

**Pump-Probe Measurement Techniques for Determining Curie Temperature
Distribution and Gilbert Damping**

Submitted in partial fulfillment of the requirements for

the degree of

Doctor of Philosophy

in

Electrical and Computer Engineering

Zhengkun Dai

B.S., Physics, Shandong University

M.S., Electrical and Computer Engineering, Carnegie Mellon University

Carnegie Mellon University

Pittsburgh, PA

December, 2019

Acknowledgements

During my Ph.D. progress, many people have offered their sincere help and support to me, either in academic or daily life. I would like to take this opportunity to thank all of them.

First of all, I would like to express my sincere appreciation to my advisor, Professor Jian-Gang (Jimmy) Zhu. He has been offering insightful guidance for my research work. He provided me many opportunities to try different ways in my research, taught me how to deal with failures, guided me to discover new things. Every discussion with him gave me new ideas as well as confidence in my research. Without his support, this thesis will not be possible. In my mind, he is an outstanding researcher with great enthusiasm and creativity, he is also an excellent teacher in academic research and life experience.

Also, I would like to thank the other committee members: Professor James A. Bain, Professor Maysam Chamanzar and Professor Vincent Sokalski. They offered constructive suggestions from different perspectives during my Ph.D. research. Their advices helped me to conduct and understand my research in novel directions.

Many other faculty and staff have offered their kind help for my research. I would like to thank Professor David Laughling and Professor Mark Kryder for being the committee members in my Ph.D. qualification exam, Professor Elias Towe for taking me as teaching assistant, Andrew Gamble for helping to set up experiment system and lab maintenance, Patricia Grieco and Chloë Mattingly for administrative work, staff of Nanotechnology Laboratory in Carnegie Mellon University for preparing samples.

I would like to thank Carnegie Mellon University, Department of Electrical and Computer Engineering, Data Storage Systems Center (DSSC) and its industrial sponsors for generous financial support throughout my Ph.D.

Friends are another important source of support during my Ph.D. time. In particular, I would like to thank Dr. Hai Li, Dr. Xiaoyu Bai and Yuwei Qin, they provided help in simulation and discussion to understand the research problems. Bing Zhou, Yang Liu and Enbo Zhang, they helped in thin film fabrication and measurement to study the magnetic properties. Dr. Jinxu Bai and Dr. Chang Yang, they helped in optical experiment design. Except for these main hands in helping me through the research, I would like to thank all the other friends who accompanied and helped me during my Ph.D. life. Dr. Matthew Moneck, Dr. David Bromberg, Dr. Vignesh Sundar, Dr. B.S.D.Ch.S. Varaprasad, Dr. Masaki Furuta, Dr. Tong Fan, Dr. Chen Wang, Dr. Baojiang Yang, Dr. Sanxi Yao, Dr. Xianglin Liu, Dr. Rulin Chen, Dr. Ermao Cai, Dr. Jun Li, Dr. Xin Wang, Dr. Menglei Sun, Dr. Jingkun Gao, Dr. Zhen Tang, Dr. Min Xu, Dr. Jinglin Xu, Jingyu Wang, Yunlu Li, Jiang He, Chenyang Wu, Dr. Yuan-Fu (Efrem) Huang, Dr. Ankita Mangal, Dr. Shivram Kashyap, Cheng-Ming Chow, Xiao Lu, Tong Mo, Sibbo Wang, Huan Cheng, Lai Jiang, Boyuan Yang. Many more names are not listed here, but your friendship is always in my mind. Thank all these friends, they provided generous help in my research work and daily life, shared my sorrow and happiness.

Most importantly, I would like to thank my family for standing behind me and supporting me, my wife Mrs. Yunfei Zang, my mother Mrs. Yuling Wang and my father Mr. Yonglu Dai. Their encouragement, understanding and love help me through the difficult times in my life. They made me a better person and where I am today.

Abstract

This doctoral thesis presents two experimental studies utilizing the pump-probe techniques with pulsed laser systems to measure (1) Curie temperature distribution in granular FePt-L1₀ magnetic thin film for heat assisted magnetic recording (HAMR) applications and (2) Gilbert damping constants, with the ability to distinguish interfacial and bulk contributions in magnetic multilayer structures.

For the first study, the granular thin film sample consists of a two-dimensional closely packed FePt metallic grains with non-magnetic carbon grain boundaries. A laser pulse, of 1064 nm wavelength and 700 ps pulse duration, is used to heat a localized area uniformly in a controlled magnetic field. The magnetization of the grains after the heating is probed utilizing Kerr effect. By varying the laser pulse energy, the heating temperature of the sample can be varied with accurate precision in controlled manner. By heating/cooling the sample across the Curie temperature at different magnetic fields, Curie temperature distribution of the grains can be characterized with precision. This method was published and widely adopted by the recording industrial. In the thesis, all the detailed experimental setups and considerations, as well as experimental measurement procedures are clearly described. The idea of utilizing magnetic oxide grain boundary to reduce Curie temperature distribution is proposed and proved in experiment. The pump-probe method is extended to measure the temperature dependence of anisotropy field around Curie temperature.

For the second study, a different pulsed laser system was built using an ultrafast laser with pulse width of 80-100fs for examining the magnetization dynamics in multilayered magnetic thin films. In this scientific investigation, the pump pulse is used to excite the magnetic moment of the sample away from equilibrium and a probe pulse with varying

time delay is used to measure the magnetization precession and damping motions that immediately follows excitation. Micromagnetic dynamic modeling is established to analyze the dynamic magnetization orientations to extract the ferromagnetic resonance frequency and the Gilbert damping constant. The developed method is capable of measuring magnetization dynamics in gigahertz to sub-terahertz range. Using this experimental setup, Co/Pt multilayered magnetic thin films with perpendicular anisotropy have been studied. It is found that in this system, there are two distinctive contributions to the overall Gilbert damping of the multilayers: One from interface and the other one from bulk. When the magnetic layers having thickness in nanometer scale, the interfacial damping dominates. Comparison between sandwiched magnetic thin films with Co as magnetic layer and Pt/Ir as nonmagnetic layers shows the nonmagnetic material and the interfacial coupling determine the overall damping together.

Table of Contents

Acknowledgements.....	ii
Abstract.....	iv
Table of Contents.....	vi
List of Figures.....	ix
List of Tables	xiv
1 Introduction	1
1.1 Background and Motivation.....	1
1.2 Heat Assisted Magnetic Recording	2
1.3 Magnetic Dynamics.....	6
1.4 Magneto Optical Kerr Effect.....	11
1.5 Thesis Outline	13
2 Pump-Probe Study of Heat Assisted Magnetic Recording Media	15
2.1 Methodology of Curie Temperature Distribution Measurement.....	15
2.1.1 Methodology and Design of Experiment.....	15
2.1.2 Micromagnetic Simulation of Methodology.....	20
2.2 Pump-Probe Experimental System	23
2.3 Curie Temperature Distribution of HAMR Media.....	28
2.3.1 Curie Temperature Distribution of HAMR Media with Different Grain Heights.....	29

2.3.2	Curie Temperature Distribution of HAMR Media with Magnetic Oxide Grain Boundary	31
2.4	Measurement of Temperature Dependence of Anisotropy Field	37
2.4.1	Methodology of $H_k(T)$ Measurement.....	37
2.4.2	Example of $H_k(T)$ Measurement.....	41
3	Simulation Study of Magnetic Dynamics Induced by Ultrafast Laser Heating	44
3.1	Modeling of Magnetic Dynamics Induced by Ultrafast Laser Heating	44
3.1.1	Two Temperature Model	44
3.1.2	Magnetic Dynamics and Kittel Model.....	47
3.1.3	Micromagnetic Simulation and Analysis.....	51
3.2	Magnetic Dynamics in Thin Films with Perpendicular Anisotropy	53
3.3	Magnetic Dynamics in Thin Films without Anisotropy.....	58
4	Time Resolved Magneto Optical Kerr Effect System	63
4.1	Ultrafast Amplified Femtosecond Ti : Sapphire Laser	64
4.2	Pump Line for the Excitation of Magnetic Dynamics.....	68
4.3	Probe Line for the Detection of Magnetic Dynamics	73
4.4	Compact Electromagnet and Sample Holder	75
5	TRMOKE Study of the Gilbert Damping in Multilayered Magnetic Thin Films	79
5.1	Study of TRMOKE Experimental Conditions	79
5.1.1	Co/Pt Fabrication and Static MOKE Measurement.....	80

5.1.2	Magnetic Dynamic Study under Different TRMOKE Measurement Conditions.....	86
5.2	Damping Constant and FMR Frequency of Co/Pt Multilayers.....	93
5.2.1	Co/Pt Fabrication and Study of Magnetic Properties	93
5.2.2	TRMOKE Study of the Gilbert Damping Constant and FMR Frequency with Different Co Thickness.....	96
5.3	Comparison of the Gilbert Damping in Sandwiched Magnetic Thin Films	100
6	Summary and Discussion of Future Directions	104
	References.....	106

List of Figures

Figure 1.1 Recording trilemma. Media pattern courtesy: Hai Li.....	3
Figure 1.2 Schematic of heat assisted magnetic recording from Reference [5].	4
Figure 1.3 Simulated HAMR media SNR degradation due to the grain-to-grain T_C and H_k variation from Reference [10].....	5
Figure 1.4 Schematic of LLG equation.....	7
Figure 1.5 MAMR switching field dependence on damping constant from Reference [13].	8
Figure 1.6 Previous studies on the damping constant vs. Co layers thickness.(a) from Reference [42] , (b) from Reference [28].	10
Figure 1.7 Magneto optical Kerr effect.....	11
Figure 1.8 Geometries of MOKE.....	13
Figure 2.1 Curie temperature distribution of recording media.	16
Figure 2.2 Interpretation of Curie temperature distribution for measurement.....	16
Figure 2.3 Testing sequence of Curie temperature distribution measurement. Media pattern courtesy: Hai Li.....	19
Figure 2.4 Micromagnetic simulation of switching curve under pulsed heating sequence.	21
Figure 2.5 Analysis of simulated Curie temperature distribution measurement. The setting values for Curie temperature distribution is 0 % for top left, 2 % for top right, 4 % for bottom left, 6 % for bottom right. The fitting values are shown in the figure.	22
Figure 2.6 Optical path of Curie temperature distribution measurement system.	23

Figure 2.7 Pulse energy control system. Top: Optical path. Bottom: Change of the polarization state. Solid red line indicates the light propagation direction. Dashed red line indicates the polarization direction.	24
Figure 2.8 Pulse energy dependence on LCVR voltage.	25
Figure 2.9 Schematic of balanced MOKE signal detection. Image of Wollaston prism is from Thorlabs.....	26
Figure 2.10 Spot sizes and overlapping of pump spot and probe spot. (a) Beam profile of probe spot. (b) Damage pattern of pump spot and overlapping with probe spot.....	27
Figure 2.11 Photo of pump-probe Curie temperature distribution measurement system.	28
Figure 2.12 Example of measured switching curves on one sample.	29
Figure 2.13 Curie temperature distribution of HAMR media with different grain heights.	30
Figure 2.14 (a) XRD patterns of C1 - C3 and T1 - T2. (b) Order parameter of C1 - C3 and T1 - T2 vs. grain size	32
Figure 2.15 (a) Perpendicular and in-plane MH loops of C3. (b) Perpendicular and in-plane MH loops of T2. (c) Dependence of perpendicular and in-plane coercivity on grain size.	33
Figure 2.16 The in-plane bright field TEM images for (a) C1, (b) C3, (d) T1, and (e) T2 with the insets being their corresponding average grain size and standard deviation. The high resolution TEM images for (c) C1 (FePt - 30 vol. % C) and (f) T1 (FePt - 40 vol. % (C + BaFe _x O _y)). The high angle annular dark field (HAADF) images (g) and the EDS mapping of (h) Pt, (i) Fe, (j) Pt + Fe, and (k) Pt + O of T1 (FePt - 40 vol. % (C + BaFe _x O _y)).	34

Figure 2.17 Curie temperature distribution as a function of average grain volume for FePt-C and FePt-BaFe _x O _y -C media.....	36
Figure 2.18 Temperature dependence of anisotropy field.	38
Figure 2.19 Switching curve simulation with different external fields.	39
Figure 2.20 Comparison of simulated $H_k(T)$ measurement results with preset media property.	40
Figure 2.21 Deviation between preset and extract temperature vs. normalized H_k	41
Figure 2.22 Normalized switching curves measured with different external field.	42
Figure 2.23 Fitting results of measured switching curves with different external field. ..	42
Figure 2.24 H_k (external field) dependence on normalized temperature.	43
Figure 3.1 Interaction of femtosecond laser with metallic magnetic film based on two temperature model.	45
Figure 3.2 Two temperature model simulation of electron temperature and phonon temperature.	46
Figure 3.3 Schematic of magnetic dynamics induced by femtosecond laser in the magnetic thin film with perpendicular anisotropy.....	47
Figure 3.4 Schematic for Kittel model derivation.	48
Figure 3.5 Evolution of normalized M_x and M_z components with time under femtosecond laser heating. The blue line is the fitting curve with Equation 3.8.	52
Figure 3.6 The evolution of M_z component with different pulse energy.....	54
Figure 3.7 The evolution of M_z component with different external field direction.	55
Figure 3.8 FMR frequency (a) and lifetime (b) vs. maximum electron temperature and external field direction.	56

Figure 3.9 Effective damping constant vs. external field direction and maximum media temperature.	57
Figure 3.10 Effective damping constant vs. magnetization direction with two external field applying methods.	58
Figure 3.11 Schematic of magnetic dynamics induced by femtosecond laser in magnetic thin film without anisotropy.	59
Figure 3.12 Evolution of M_z component with different external field direction.	60
Figure 3.13 FMR frequency (a) and lifetime (b) vs. maximum media temperature and external field direction.	61
Figure 3.14 Scaled effective damping constant vs. external field direction.	62
Figure 4.1 Full optical path of TRMOKE system.	63
Figure 4.2 Optical path and principle for pulse energy control.	65
Figure 4.3 Polarization state of light before and after half waveplate.	66
Figure 4.4 Beam spot size control system.	68
Figure 4.5 Optical path of pump line.	69
Figure 4.6 Spot size analysis with CCD camera. (a) The intensity image of laser spot; (b) 3D plot of laser intensity; (c) Intensity plot along X axis; (d) Intensity plot along Y axis. (c) (d) are the cross section at spot center.	70
Figure 4.7 Spot center drifting and adjustment.	72
Figure 4.8 Optical path of incident probe beam.	73
Figure 4.9 Optical path for MOKE detection.	75
Figure 4.10 Photo and the simulation of magnetic field for homemade electromagnet. ..	76
Figure 4.11 TRMOKE delay control.	77

Figure 4.12 TRMOKE detection.....	77
Figure 5.1 Film stack and in-plane MH loops of Co/Pt multilayered magnetic thin films.	80
Figure 5.2 Schematic of angled MH measurement.....	81
Figure 5.3 Typical angled MH measurements with and without pump pulse.	82
Figure 5.4 Magnetization direction measured under different pulse energy.	84
Figure 5.5 Effective anisotropy field dependence on Co layer thickness.....	85
Figure 5.6 TRMOKE measurement performed with different pulse energies for Co(0.8nm)/Pt(0.6nm) film.	86
Figure 5.7 TRMOKE measurement performed with different external field angle for Co(0.8nm)/Pt(0.6nm) film.	87
Figure 5.8 FMR frequency dependence on external field direction.	88
Figure 5.9 Lifetime dependence on external field direction.	89
Figure 5.10 Effective damping constant vs. pulse energy.	90
Figure 5.11 Comparison of damping constant measured with different external field conditions.....	91
Figure 5.12 (a) Film stack of Co/Pt multilayered magnetic thin film. (b) and (c) In-plane and perpendicular MH loops measured with MPMS-3, respectively.	93
Figure 5.13 M_s and H_k^{eff} dependence on single Co layer thickness. Red open circles: H_k^{eff} from angled MH measurements.....	94
Figure 5.14 Interfacial anisotropy constant calculation.	95
Figure 5.15 Examples of TRMOKE measurement. The black lines are fitting curves to Equation 3.8.	96

Figure 5.16 FMR frequency vs. single Co layer thickness.	97
Figure 5.17 Lifetime dependence on single Co layer thickness.	98
Figure 5.18 Damping constant vs. single Co layer thickness.	99
Figure 5.19 Film stacks for the comparison of sandwiched magnetic thin films with Co as magnetic layer, Pt and Ir as non-magnetic layer.	101
Figure 5.20 Perpendicular and in-plane MH loops for sandwiched magnetic thin films.	101
Figure 5.21 Damping constant vs. external field direction for sandwiched magnetic thin films with Pt and Ir as nonmagnetic layers.	102

List of Tables

Table 3.1 Values for two temperature model simulation.	46
---	----

1 Introduction

1.1 Background and Motivation

Magnetic materials have been widely used in today's recording industry and the development of future technologies. For example, granular thin film media with perpendicular magnetic anisotropy has been used as the recording media in hard disk drive (HDD) since 2005 [1],[2]. However, the explosion of data requires higher recording densities for HDD [3],[4]. Two energy assisted magnetic recording methods were proposed to be the next generation technologies in HDD, Heat Assisted Magnetic Recording (HAMR) and Microwave Assisted Magnetic Recording (MAMR) [5],[6]. Except for recording media in HDD, magnetic devices also play a key role in many applications. Magnetic tunneling junction (MTJ) is used as the reader in hard disk drive [7]. The spin torque oscillator (STO) is used to generate localized microwave field for MAMR [6]. Several companies are developing the magneto resistive random-access memory (MRAM) based on MTJ, which is an excellent candidate for non-volatile random-access memory [8],[9].

There are many challenging problems in developing and optimizing the magnetic materials in these applications. One of the challenging problems in HAMR is the measurement and control of the Curie temperature (T_C) distribution in the recording media that affects the HAMR recording performance significantly [10],[11]. In MAMR, the generation of localized microwave fields and the matching of the resonant frequency with the recording media are challenging problems [12]. The damping constant of the MAMR recording media can also affect the writability significantly [13]. In MRAM, the switching speed and the switching current density are related to the damping constant [14]–[16].

Therefore, some fundamental measurements and understandings of the magnetic properties are essential for the research in these areas. This thesis is focused on developing optical pump-probe methods to characterize and study some of the key properties of magnetic thin films, including the T_C distribution of HAMR media, the damping constant and ferromagnetic resonance (FMR) frequency of multilayered magnetic thin films.

1.2 Heat Assisted Magnetic Recording

HDD is one of the most widely used data storage products in market and the recording density grows steady in the past few decades [3]. However, due to the recording trilemma, the recording density of current perpendicular magnetic recording (PMR) technology is going to reach the limit. The recording trilemma is determined by three key factors, signal-to-noise ratio (SNR), thermal stability and writability [17],[18],[19]. Figure 1.1 shows the origin of recording trilemma. As shown in Figure 1.1, the recording media in HDD contains grains with uniaxial anisotropy in perpendicular direction w.r.t film normal. Each bit contains multiple grains with the same magnetization direction. 1s and 0s are represented by two different magnetization directions. The data is read out through the transition region between bits. The SNR is proportional to the number of grains in the bit region [17]. To increase the recording density and maintain sufficient SNR, the area of a single grain must be reduced.

However, the reduced grain area will bring in the thermal stability problem. For long term data storage, the recording grains should be able to maintain the magnetization directions against the thermal agitation that tends to randomize the distribution of magnetization directions of the grains. The switching probability P_s of a single grain is determined by Equation 1.1 [19].

$$P_s = f_0 \exp\left(\frac{-K_u V}{k_B T}\right) \quad (1.1)$$

where K_u is the magneto crystalline anisotropy constant, V is the grain volume, $K_u V$ is the magneto crystalline anisotropy energy, i.e. the energy barrier between up and down magnetizations. k_B is the Boltzmann constant, T is the environmental temperature, $k_B T$ is the thermal agitation energy. f_0 is the attempt frequency, which has the order of 10^9 to 10^{12} [18],[19]. $K_u V/k_B T$ should be larger than 55 to store data for at least five years [17]. To keep the thermal stability for smaller grains, the magneto crystalline anisotropy constant K_u must be increased accordingly. L1₀-FePt with K_u as high as 4.5×10^7 erg/cc is one of the most widely studied materials that were proposed as HAMR media [11].

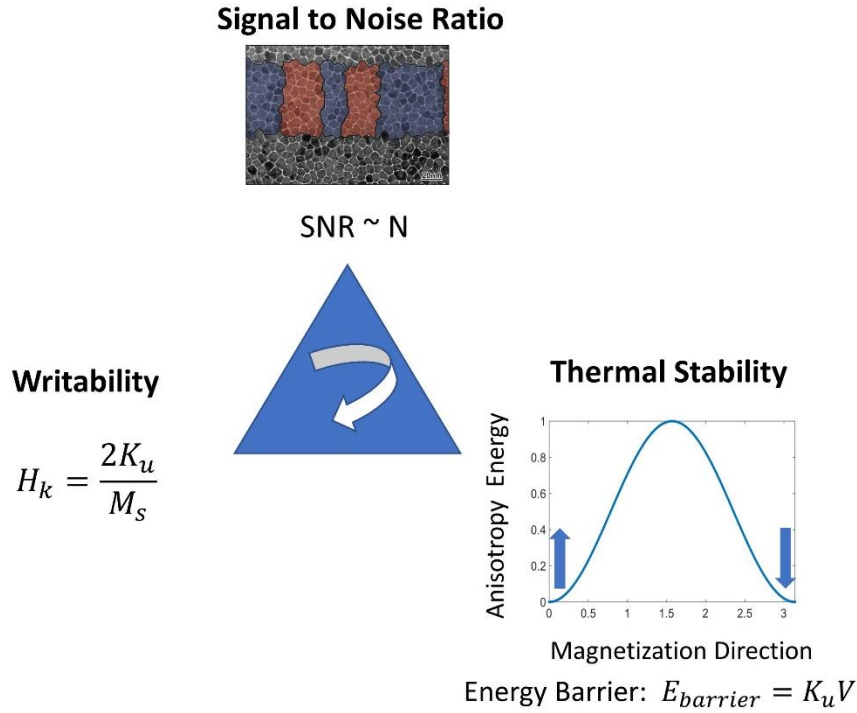


Figure 1.1 Recording trilemma. Media pattern courtesy: Hai Li

High K_u will bring the writability problem. Since the grain volume is very small, the magnetic moment of one grain can be treated as single macro spin and described by Stoner-

Wohlfarth model [20]. The field required to switch the moment of the grains can be expressed by Equation 1.2.

$$H_K = \frac{2K_u}{M_s} \quad (1.2)$$

where H_K is the anisotropy field, M_s is the saturation magnetization. Grains with higher K_u require higher switching field which can easily goes beyond the field of write head. The maximum strength of write head field is limited by the material and the geometry design which is about 1T [21],[22].

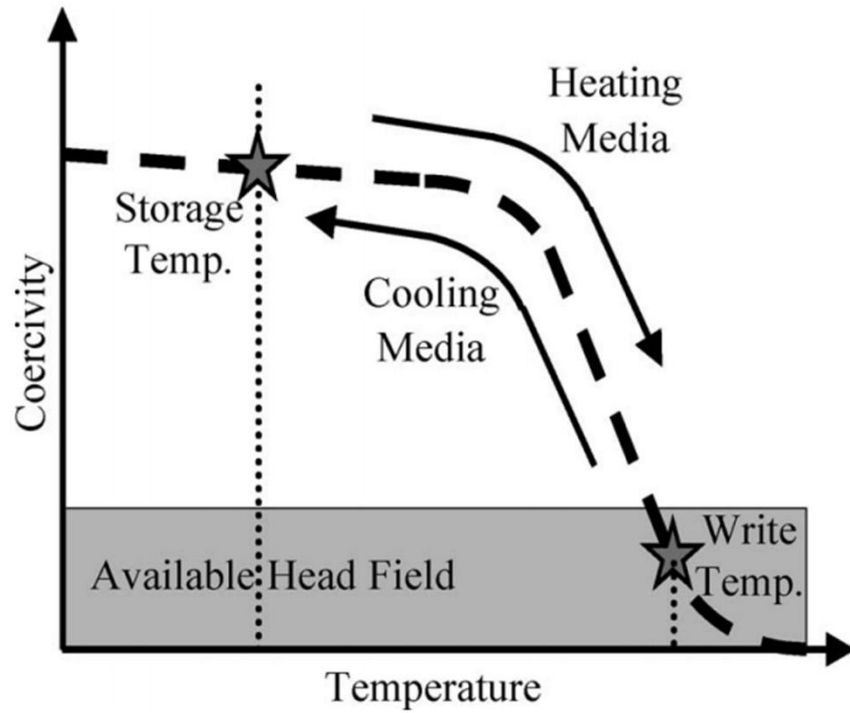


Figure 1.2 Schematic of heat assisted magnetic recording from Reference [5].

To solve the recording trilemma and achieve higher recording density, HAMR is proposed to be one of the candidates for the next generation recording technologies. The key idea of HAMR is shown in Figure 1.2. K_u is a temperature dependent property and decreases with increasing temperature. During recording, K_u is reduced by heating the media locally near or above T_C , thus the magnetic moments of the grains can be switched by the available head field. After writing, the media will cool down to room temperature and maintain thermal stability for long term data storage.

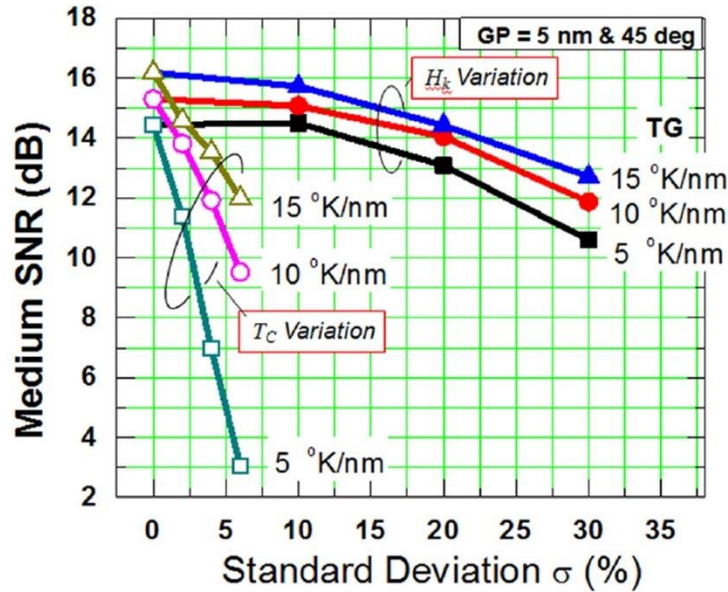


Figure 1.3 Simulated HAMR media SNR degradation due to the grain-to-grain T_C and H_k variation from Reference [10].

Since the media is heated and cooled in HAMR, the magnetic properties that depend on temperature are essential to improve HAMR performance. However, the recording media is granular film, the properties of all grains are not identical and usually form some distribution over temperature. Hai Li, et.al. studied the effect of media property distributions on the SNR of recording patterns with standard distributions of T_C and H_K added during simulation [10]. Figure 1.3 showed the σ_{T_C} is one of the key factors that

determines the recording SNR. Large σ_{T_C} can result in a significant degradation of SNR. Therefore, a method to measure T_C distribution is crucial for characterizing and optimizing the HAMR recording media. One of the successful experimental methods to measure T_C distribution was proposed by S. Pisana, et al. with the switching probability measurement through optical pump-probe method [23],[24]. In this thesis, the micromagnetic simulation was adopted to understand the methodology and improve the experimental measurement. A pump-probe experimental system was built with shorter pump pulse width to achieve more accurate measurement.

Another important property of HAMR recording media is the temperature dependence of anisotropy field $H_k(T)$ that determines the effective field gradient dH_{eff}/dx with the thermal gradient dT/dx through Equation 1.3.

$$\frac{dH_{eff}}{dx} = \frac{dH_k}{dT} \frac{dT}{dx} \quad (1.3)$$

In case of same dT/dx , larger dH_k/dT near T_C will result in larger dH_{eff}/dx that improves the sharpness of transition region and reduces the transition jitter noise. Thus, a method to measure $H_k(T)$, especially near T_C , is essential for HAMR media research. In this thesis, the pump-probe method was extended to measure the $H_k(T)$ near T_C for the first time [25].

1.3 Magnetic Dynamics

Most applications based on magnetic phenomenon involve the switching of magnetic moment which is a dynamic process. For example, in magnetic recording, the writing process is the switching of magnetic moment from one direction to the other direction. In

STO, the magnetic moment precesses rapidly to generated localized microwave field. The magnetic dynamic process can be simulated by micromagnetic modeling with Landau-Lifshitz-Gilbert (LLG) equation which has the form of Equation 1.4 [26] .

$$\frac{d\vec{M}}{dt} = -\gamma\vec{M} \times \vec{H} + \frac{\alpha}{M_s}\vec{M} \times \frac{d\vec{M}}{dt} \quad (1.4)$$

In LLG equation, t is the evolution time, \vec{H} is the total field, \vec{M} is the magnetic moment. γ is the gyromagnetic ratio, which is $1.76 \times 10^7 \text{ Oe}^{-1} \text{ S}^{-1}$ for electron. The parameter α is a phenomenal parameter introduced by Gilbert, which is called Gilbert damping constant. As shown in Figure 1.4, the first term of LLG equation determines the precession of the magnetic moment around the total field. The second term determines the damping of the magnetic moment towards the total field. With higher α , \vec{M} can damp to \vec{H} direction faster. From the perspective of energy, α determines the energy dissipation rate from high energy state to low energy state.

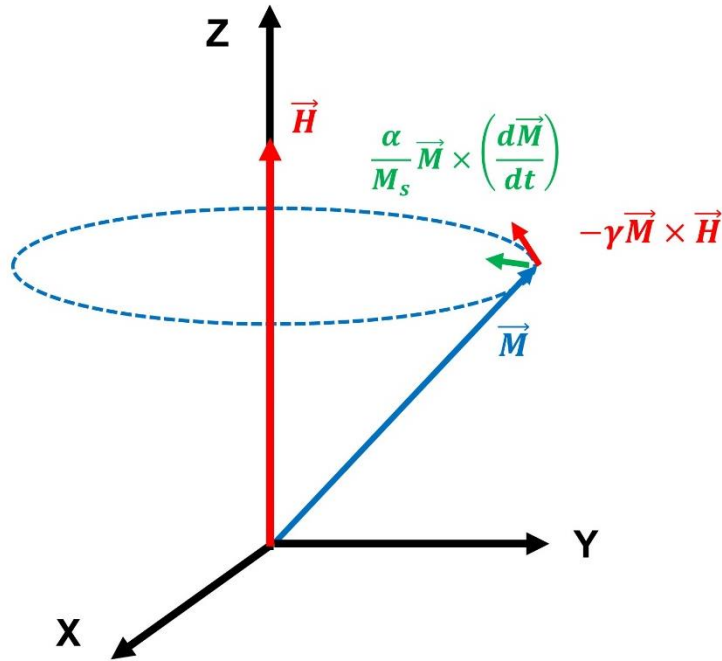


Figure 1.4 Schematic of LLG equation.

The damping constant α is an important parameter in many scenarios. The reversal time of magnetic moment has inverse dependence on the damping constant [15], thus higher damping constant can settle down the magnetic moment faster to the equilibrium state. In other scenarios, lower damping constant is preferable. J-Zhu, et.al. studied the effect of media damping constant on the switching field in MAMR [13]. As shown in Figure 1.5. lower media damping constant requires smaller switching field. In STT-MRAM, the critical switching current density J_c is proportional to the damping constant which means lower damping constant is desired to reduce the power consumption in devices [15].

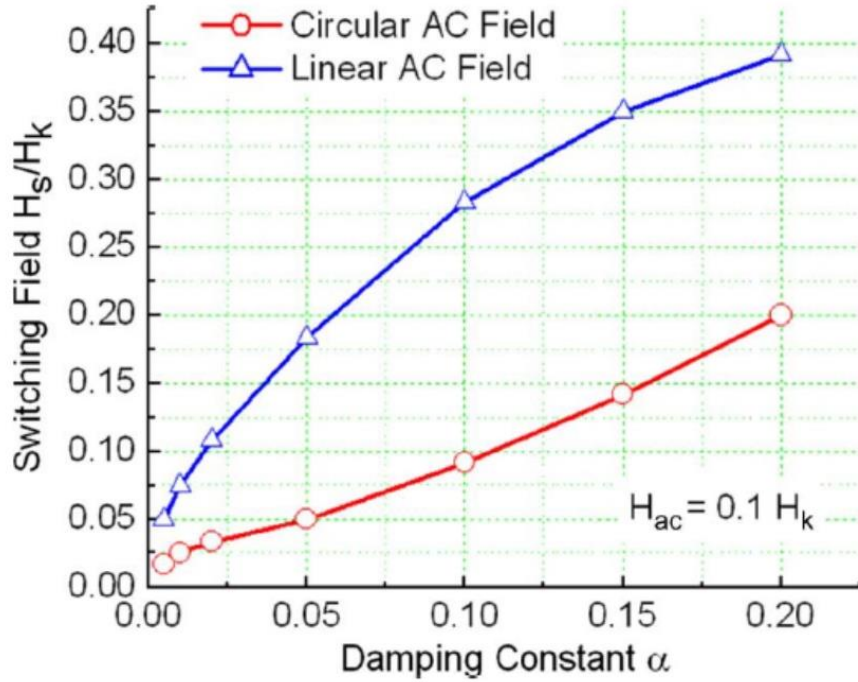


Figure 1.5 MAMR switching field dependence on damping constant from Reference [13].

The measurement and control of damping constant are critical to achieve the best performance in different applications. There are two main categories of the experimental techniques for the study the magnetic dynamics: (1) frequency domain and (2) time domain. FMR is the most widely used frequency domain method through the measurement of the microwave absorption spectrum. The damping constant is determined by the width of the

resonant absorption peak [27]. Time resolved magneto optical Kerr effect (TRMOKE) is the time domain study taking the advantage of the femtosecond laser. The magnetic dynamic process is excited by femtosecond laser pulse pump and detected through magneto optical Kerr effect (MOKE) with varying time delay after excitation. The damping constant can be extracted from the measurement of dynamic process [28]. Compared with FMR study, TRMOKE is a localized method with high SNR [29],[30] and doesn't have the radioactive contribution to the damping [31]. In this thesis, TRMOKE was chosen as the experimental technique for the study of Gilbert damping constant and FMR frequency.

Co/Pt multilayered magnetic thin film is widely used in the development of spintronic applications, such as magnetic tunneling junction [32], [33] and domain wall motion [34], [35]. The damping originates from the coupling of spin angular momentum to the orbital angular momentum [36], [37]. Since the perpendicular anisotropy (PMA) arises from the spin orbital coupling at Co/Pt interfaces [38], it has been believed that the same coupling should also contribute to the Gilbert damping through interfacial effect [39], [40].

Many different approaches have been made to measure and understand the damping constant of Co/Pt multilayers, however, the results and origins still remain controversial. Some studies measured the damping constant with FMR. A. Caprile et al. reported the damping constant almost linearly increases from 0.05 to 0.17 for $[\text{Pt}(0.2 \text{ nm})/\text{Co}]_6$ with Co thickness t_{Co} from 0.2 nm to 0.32 nm [41]. N. Fujita et al. studied $[\text{Co}/\text{Pt}(1.4 \text{ nm})]_{12}$ with t_{Co} from 0.3 nm to 8 nm [42]. As shown in Figure 1.6 (a) the damping constant first decreases from 0.037 to 0.025 with t_{Co} from 1.0 nm to 1.8 nm, then gradually increases with t_{Co} [42]. Other researchers measured the damping constant with TRMOKE. A. Barma et al. studied the magnetic dynamics of $[\text{Co}(0.4 \text{ nm})/\text{Pt}(0.8 \text{ nm})]_n$ multilayers with layer

repeat number n from 2 to 12 [43]. The reported effective damping constant α_{eff} increases from ~ 0.1 to ~ 0.13 with increasing n . However, the corresponding perpendicular anisotropy shows a decreasing trend. S. Mizukami et al. measured α_{eff} of Pt(5 nm)/Co/Pt(2 nm) layer with t_{Co} varied from 0.5 nm to 4.0 nm [28]. They reported a rapid increase of α_{eff} with decreasing t_{Co} when $t_{Co} < 1.0$ nm as shown in Figure 1.6 (b) [28]. The reported α_{eff} varies from ~ 0.05 to ~ 0.45 with decreasing Co thickness [28].

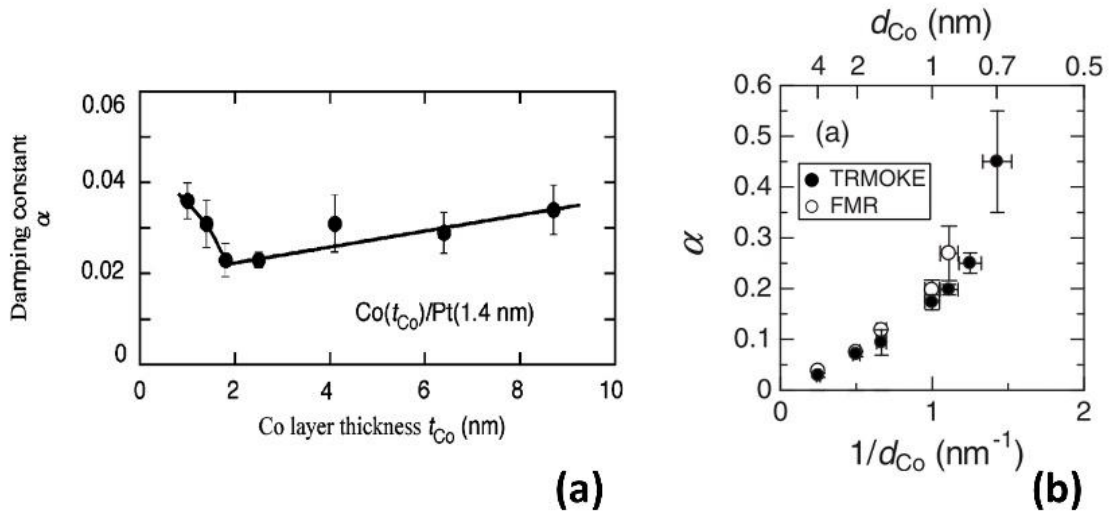


Figure 1.6 Previous studies on the damping constant vs. Co layers thickness.(a) from Reference [42] , (b) from Reference [28].

Some recent theoretical studies on Ferromagnetic(FM)/Nonmagnetic Metal(NM) multilayers propose the damping constant should be inversely proportional to the FM layer thickness plus a constant bulk contribution which can be express by Equation 1.5 [40], [44].

$$\alpha = \frac{\alpha_s}{t_m} + \alpha_b \quad (1.5)$$

where α_s is the contribution through the spin diffusion to the NM layer, which is inversely proportional to the magnetic layer thickness t_m , the second term α_b is the contribution from the bulk value of magnetic layer. In this thesis, an in-depth study of the magnetic dynamics in Co/Pt multiplayered films with different Co layer thickness will be performed.

1.4 Magneto Optical Kerr Effect

The experimental work of this thesis is based on magneto optical Kerr effect. Here we briefly introduced the principle of MOKE that will be utilized in this work, more application details will be described in the following chapters.

MOKE was discovered by Kerr in 1877 [45]. MOKE describes the effect of light interacting with the magnetic moment in materials. Macroscopic understanding can be described with the dielectric tensor, which has the form of Equation 1.6 [46] [47].

$$\epsilon = \epsilon_0 \begin{pmatrix} 1 & -iQ_z & iQ_y \\ iQ_z & 1 & -iQ_x \\ -iQ_y & iQ_x & 1 \end{pmatrix} \quad (1.6)$$

where Q_x , Q_y and Q_z determine the coupling between YZ, XZ and XY directions, respectively.

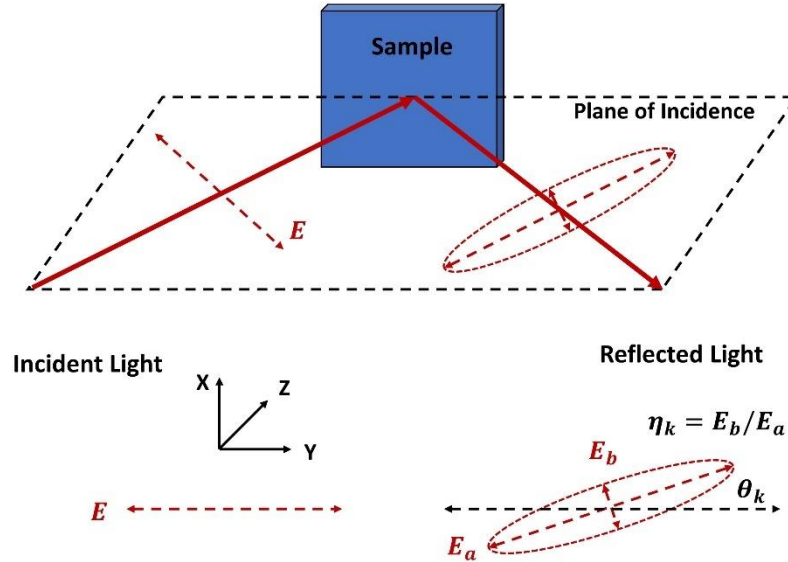


Figure 1.7 Magneto optical Kerr effect.

When linearly polarized light is reflected from the magnetic surface, the polarization state of reflected light will be changed due to the off-diagonal terms in the dielectric tensor.

In magnetic thin film, the magnitudes of the off-diagonal terms are proportional to the magnetic moment in the corresponding directions [47]. Thus, the state of reflected light indicates the magnetic state of the film. Taking P-polarized light for example as shown in Figure 1.7. When P-polarized light is reflected off a magnetic surface, the reflected light has a major P-component as ordinary reflection. A minor S-component also appears due to the coupling from the off-diagonal terms. The S-component is usually out of phase with respect to the reflected P-component. The polarization state of reflected light will be the combination of these two components and become elliptically polarized. The major axis is rotated by a small angle θ_k with respect to the polarization direction of the incident light, the ellipticity of the reflected light is describe by η_k .

Depends on the different geometries of measurement, MOKE can be classified into three categories: (1) Longitudinal MOKE, (2) Transversal MOKE, (3) Polar MOKE, as shown in Figure 1.8. In longitudinal MOKE, the magnetic moment lies in film plane and parallel to the plane of incidence. In transversal MOKE, the magnetic moment lies in film plane and perpendicular to the plane of incidence. In polar MOKE, the magnetic moment is perpendicular to the film plane and the out of plane component of magnetic moment is detected. The incident light in polar MOKE is normal or near normal to the film plane.

The signal of polar MOKE is usually larger than the other two configurations [48] and the study in this thesis is mainly focused on the magnetic thin films with perpendicular anisotropy, thus polar MOKE geometry was adopted in this thesis. Since θ_k and η_k are

very small, with small angle approximation, the intensity change in the polarization direction of incident light is proportional to the magnetic moment [47].

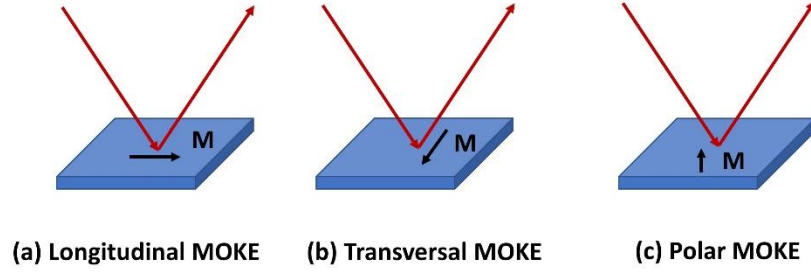


Figure 1.8 Geometries of MOKE.

1.5 Thesis Outline

In this thesis, micromagnetic simulation was adopted to understand the methodology of optical pump-probe measurement. Experimental systems based on MOKE were designed and built to study the T_C distribution of HAMR media and the Gilbert damping constant of magnetic multilayered thin film.

Chapter 1 is a brief introduction of background information and the motivation to study the T_C distribution for HAMR media and Gilbert damping constant of magnetic multilayered thin films.

In Chapter 2, the methodology to measure T_C distribution was presented. The design of experiment was studied and validated with micromagnetic simulation. The optical pump - probe system was built to measure T_C distribution. A novel HAMR recording media with magnetic oxide as grain boundary was proposed and fabricated to reduce T_C distribution. The pump-probe method was extended to measure the temperature dependence of anisotropy field $H_k(T)$ around T_C .

In Chapter 3, the simulation model of TRMOKE triggered by femtosecond laser heating was presented. The magnetic dynamic process was studied through micromagnetic

modeling with different media properties to understand and guide the experiment. The phenomenal model to analyze TRMOKE measurement was validated with the micromagnetic simulation data.

In Chapter 4, the design and construction of TRMOKE measurement system were presented and discussed in detail.

In Chapter 5, the best experimental conditions to perform reliable TRMOKE measurement were studied with Co/Pt multilayers. The Gilbert damping constants and FMR frequencies of Co/Pt layers with difference Co layer thickness were accurately measured. The Gilbert damping constant of Co/Pt multilayers was found to contain a part inversely proportional to the magnetic layer thickness in addition to the bulk contribution of magnetic layer, which provided an effective way to tune the damping constant of magnetic multilayers. Comparison of Co/Pt and Co/Ir multilayered thin films shows the nonmagnetic material and the interfacial coupling determine the overall damping together.

Chapter 6 is the summary of the whole thesis and discussion of future interesting areas.

2 Pump-Probe Study of Heat Assisted Magnetic Recording Media

This chapter is focused on the measurement of T_C distribution and $H_k(T)$ of HAMR recording media. The theoretical analysis and design of experiment will be presented first. The feasibility of the experimental design will be validated by micromagnetic simulation. The layout and capability of pump-probe experimental system will be presented in detail. The T_C distribution of HAMR media from industrial sponsors and HAMR media with magnetic oxide grain boundary will be measured. Results show the magnetic oxide grain boundary can effectively reduce T_C distribution for HAMR media with small grain size. A novel way to measure $H_k(T)$ will be presented at the end of this chapter.

2.1 Methodology of Curie Temperature Distribution Measurement

2.1.1 Methodology and Design of Experiment

HAMR recording media contains magnetically decoupled grains with perpendicular anisotropy. Due to the ordering, grains size and many other factors, the T_C of all grains are not identical [49]–[52]. As shown in Figure 2.1, taking the T_C of all grains into statistics, they will form a probability distribution over temperature. The T_C distribution can be assumed to follow a Gaussian distribution that can be described by Equation 2.1 [23], [24].

$$f(T) = \frac{1}{\sigma_{T_C} \sqrt{2\pi}} e^{-\frac{(T-\bar{T}_C)^2}{2\sigma_{T_C}^2}} \quad (2.1)$$

where $f(T)$ is the probability distribution over temperature, \bar{T}_c is the average Curie temperature of all grains.

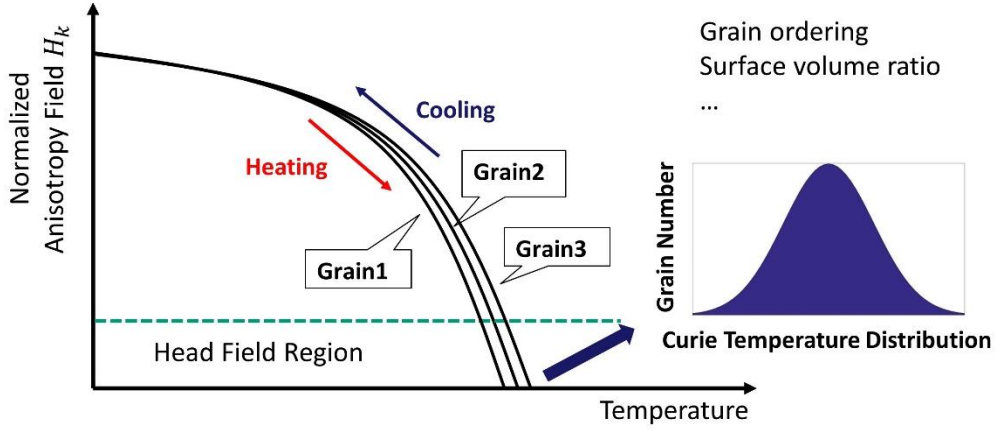


Figure 2.1 Curie temperature distribution of recording media.

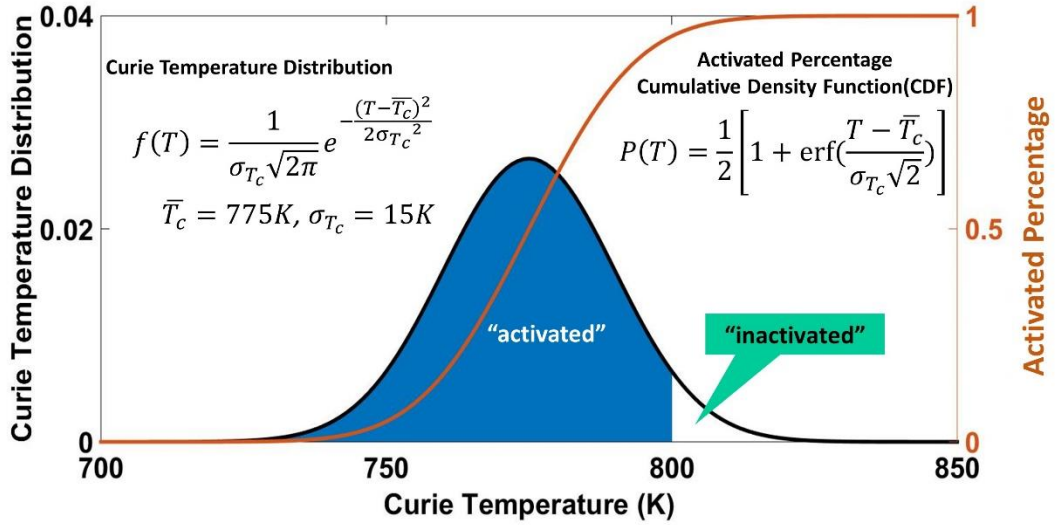


Figure 2.2 Interpretation of Curie temperature distribution for measurement.

To measure σ_{T_c} , we need a method to identify the ratio of grains corresponding to a specific temperature. In experiment, it is impossible to measure the T_c for all grains to perform statistic analysis. However, in macroscopic view, we can heat the media to a specific temperature T and measure the ratio of grains that have T_c equal to or lower than T , which can be achieved through magnetic remanence measurement [23],[51]. As shown

in Figure 2.2, the black curve stands for the T_C distribution with 775K \bar{T}_C and 15K σ_{T_C} . In HAMR recording media, the magnetic moments of the grain have two stable directions, positive and negative along film normal direction. The media is assumed to be saturated in negative direction before measurement. If the media is heated to 800K, the grains with T_C equal to or lower than 800K will have zero magneto crystal anisotropy, which are shown as activated grains in the blue region in Figure 2.2. During cooling process, these activated grains will have randomly distributed magnetization directions without external field $H_{external}$ or switched to the direction of a positive $H_{external}$, even $H_{external}$ is very small. The grains with T_C higher than T will maintain the negative direction since they still have some anisotropy. If $H_{external}$ is applied $H_{external}$ should be small enough to have negligible effect on inactivated grains. The percentage of grains $P(T)$ with T_C equal to or lower than the media temperature T can be calculated from the change of magnetic moment. $P(T)$ is the cumulative density function (CDF) of T_C distribution $f(T)$.

$$P(T) = \frac{1}{2} \left[1 + \operatorname{erf} \left(\frac{T - \bar{T}_C}{\sigma_{T_C} \sqrt{2}} \right) \right] \quad (2.2)$$

where erf is the error function. $P(T)$ measured with and without external fields can be calculated from Equation 2.3.

$$P(T) = \begin{cases} \frac{2(M(T) - M_{neg})}{M_{pos} - M_{neg}} & \text{with } H_{external} \\ \frac{M(T) - M_{neg}}{M_{pos} - M_{neg}} & \text{without } H_{external} \end{cases} \quad (2.3)$$

where M_{pos} and M_{neg} are the positive and negative saturation magnetic moment which correspond to all grains saturated in positive and negative directions, respectively. $M(T)$ is the magnetic moment measured with or without external field after heating the media to

temperature T and cooling down. The scale factor 2 without $H_{external}$ comes from the random distribution of magnetization directions of activated grains during cooling. $P(T)$ defines the percentage of grains that can be switched from negative direction to the positive direction by heating the media to temperature T , which is called switching curve in this thesis.

In the previous analysis, the thermal agitation was assumed to have no effect on the magnetization directions of the grains and only the external field determines the state of the media during the heating and cooling process. In reality, thermal agitation does affect the stability of the grains. From Equation 1.1, it can be concluded high temperature and long dwell time can significantly increase the switching probability of the moment. Even the media temperature T is lower than T_C , the media will result in a demagnetized state if the heating and cooling is not fast enough. Thus, an instant heating method is critical to minimize the thermal agitation effect to distinguish the switching behavior of grains with different T_C .

Traditional heating methods, such as hot plate or oven, will bring in significant thermal agitation effect due to the second scale heating and cooling speed. What's more, the synchronized and instant measurements of temperature and magnetization are quite difficult in these methods. Any time delay in the temperature measurement will lead to inaccurate relationship of $P(T)$. To solve these problems, nanosecond pulse laser was chosen to heat the media. The temperature raise is proportional to the pulse energy, which can provide accurate control of media temperature [23]. The region of laser heating is sub-mm that ensures fast heat dissipation through substrate. The dwell time of media at high temperature is in nanosecond time scale, which means the grains with T_C above the heating

temperature T will not be affected by the thermal agitation significantly. For localized detection, continuous He-Ne laser was used to measure the magnetic moment in heated region through MOKE.

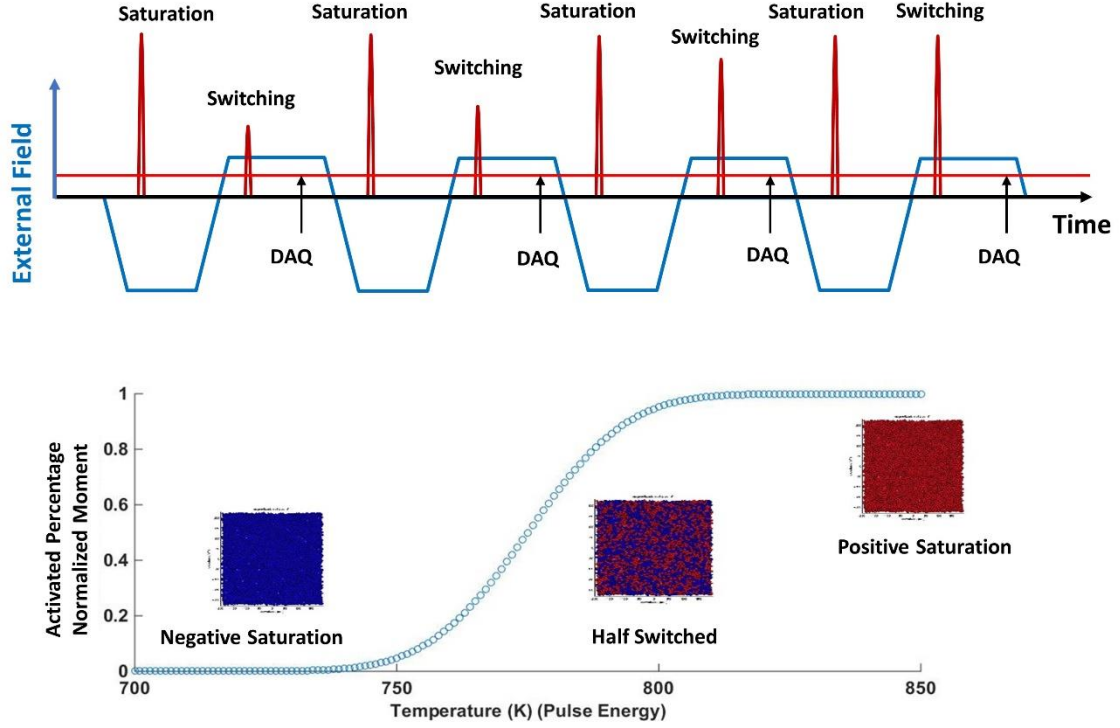


Figure 2.3 Testing sequence of Curie temperature distribution measurement. Media pattern courtesy: Hai Li

Figure 2.3 shows the design of testing sequence to measure $P(T)$. The horizontal axis stands for the time and the vertical axis stands for the $H_{external}$. First, $H_{external}$ was set to maximum value in negative direction. However, the maximum magnetic field from a traditional electromagnet is lower than 2 T, which is not high enough to saturate the HAMR media alone. Then a laser pulse with high pulse energy E_p is applied to heat all the grains above their T_C to saturate the media in negative direction during cooling. This process is labeled as saturation in Figure 2.3.

After negative saturation, $H_{external}$ is set to a small positive value for switching the activated grains or zero to demagnetize the activated grains. A switching laser pulse with small E_p is used to heat the media to a temperature T . After the media cools down to room temperature, the activated grains will be switched or demagnetized, then the magnetic moment is measured through MOKE. This process is labeled as switching in Figure 2.3. The saturation and switching process are repeated with gradually increasing switching pulse energy E_p until the media is saturated in positive direction or fully demagnetized. Through this measurement sequence, the $M(T)$ relationship can be acquired as shown in Figure 2.3 with T scaled by E_p . $P(T)$ is normalized $M(T)$ and σ_{T_c} be extracted through fitting $P(T)$ to Equation 2.2. In this testing sequence, the media is negatively saturated before each heat assisted switching with high pulse energy and negative magnetic field. Another simpler sequence is only saturate the media in negative direction once since the inactivated grains still maintains negative direction after heat assisted switching.

2.1.2 Micromagnetic Simulation of Methodology

There are several assumptions in the design of experiment in Section 2.1.2, micromagnetic simulation was performed to study the feasibility of the methodology in this section. An excellent micromagnetic simulation model developed by Hai Li was used to simulate the experimental procedure. The details of simulation model can be found in Reference [53]. Here we focus on the analysis and discussion of simulation results.

In micromagnetic simulation, the \bar{T}_c was assumed to be 775K. A Gaussian distribution variation was added to the T_c of grains randomly to simulate the T_c distribution. The initial directions of the all grains were set to negative direction. We assumed the media was heated under a sequence of Gaussian temperature profiles in time domain. There was no spatial

distribution of the media temperature, i.e. the media was heated uniformly in space. The full width of half maximum (FWHM) of the heating time profiles was set to 12.5 ns. The peak temperatures of the heating profiles were gradually increased until well above the highest T_C of grains. After each heating, the media was cooled down to room temperature. The magnetic moments of grains were summarized and normalized to get $P(T)$. The experimental process without external field was simulated, which corresponds to the demagnetization final state.

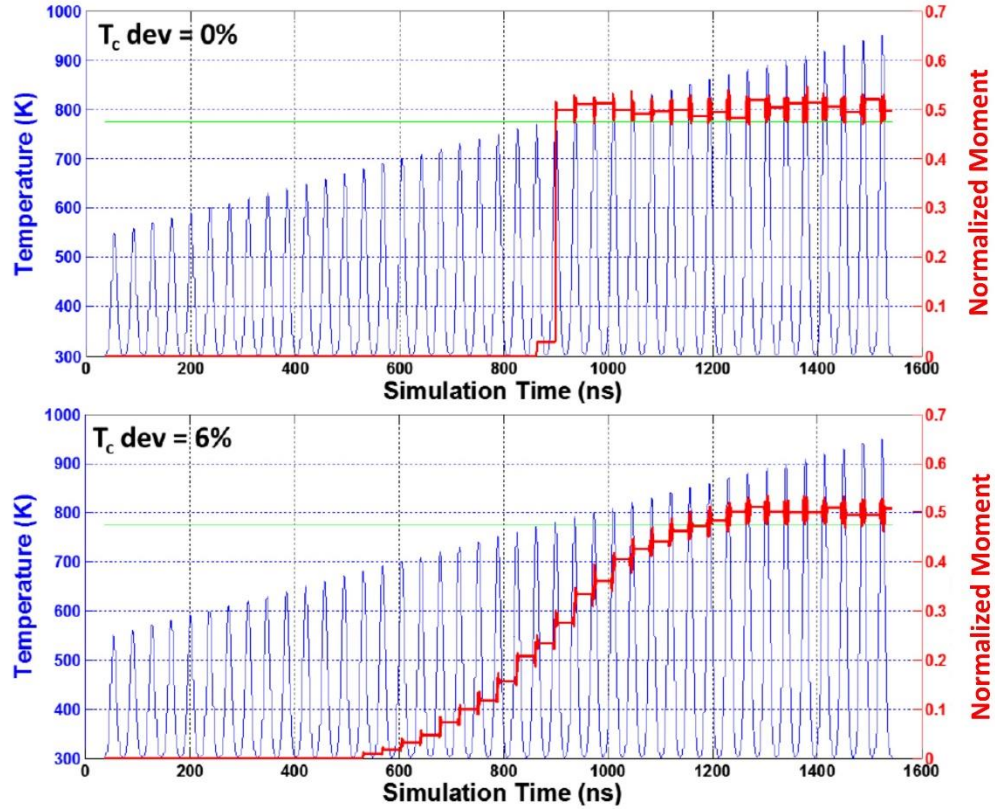


Figure 2.4 Micromagnetic simulation of switching curve under pulsed heating sequence.

Figure 2.4 shows the simulation results with 0% and 6% σ_{T_C} . The horizontal axis is the simulation time. The left vertical axis is the media temperature and the green line indicates 775K. The right vertical axis is normalized moment, which is calculated from the total magnetic moment of the grains. The negative and positive saturation moment were defined

as 0 and 1 for normalization, respectively. As shown in Figure 2.4(a), the switching curve with 0% σ_{T_c} exists a sharp transition when the media was heated to 775K. Figure 2.4(b) shows the switching curve with 6% σ_{T_c} , the switching starts as low as 600K and finishes till 1200K. The micromagnetic simulation shows a clear broad transition region for the media with high T_c distribution.

To calculate σ_{T_c} , the switching curves from simulation was differentiated to convert the cumulative density function into Gaussian distribution function. Figure 2.5 shows the histogram of Gaussian distributions calculated from switching curve simulation. Red curves are fitting curves to Equation 2.1. The fitting \bar{T}_c and σ_{T_c} values match well with the simulation settings which validates the methodology to measure σ_{T_c} .

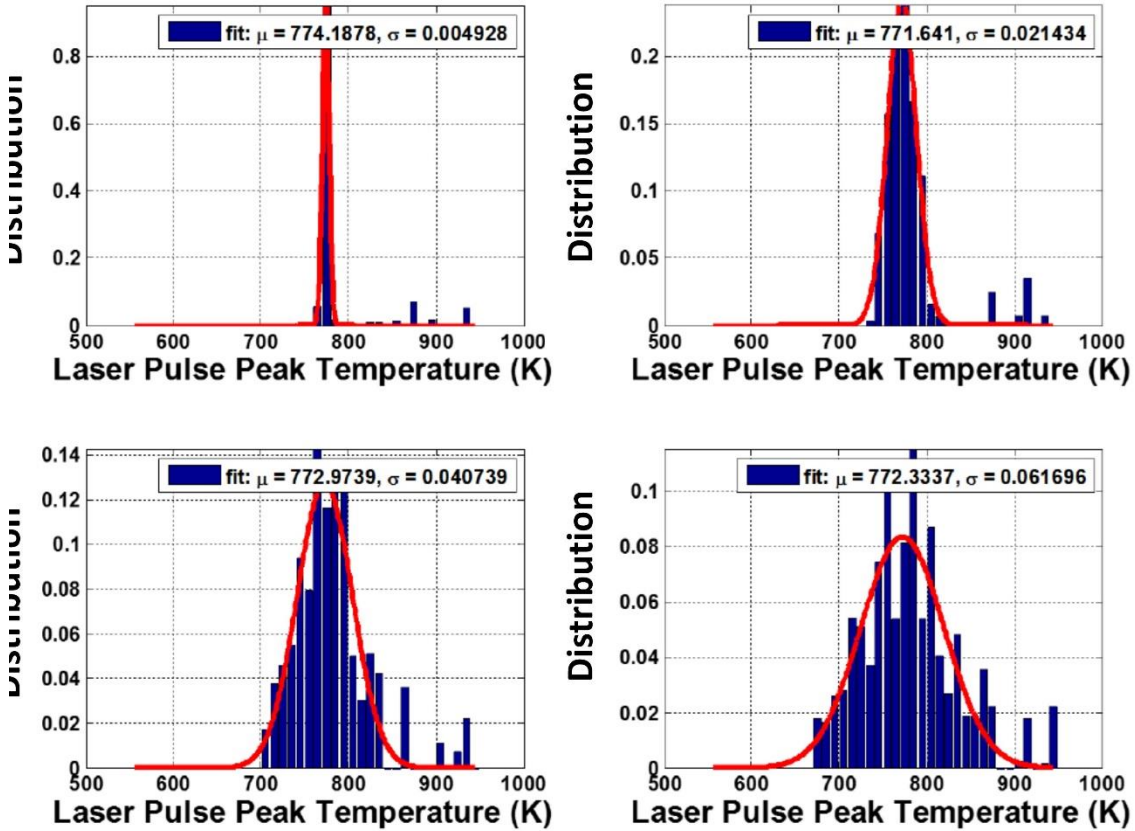


Figure 2.5 Analysis of simulated Curie temperature distribution measurement. The setting values for Curie temperature distribution is 0 % for top left, 2 % for top right, 4 % for bottom left, 6 % for bottom right. The fitting values are shown in the figure.

2.2 Pump-Probe Experimental System

Following the design of experiment in Section 2.1, a pump-probe MOKE system was designed to measure the T_C distribution. There were several updates of the system [25][54], the most advanced design will be presented here. The system contains two major parts, the pump laser line to heat the sample and the probe laser line to measure the magnetic moment through MOKE. Figure 2.6 shows the optical path of the system.

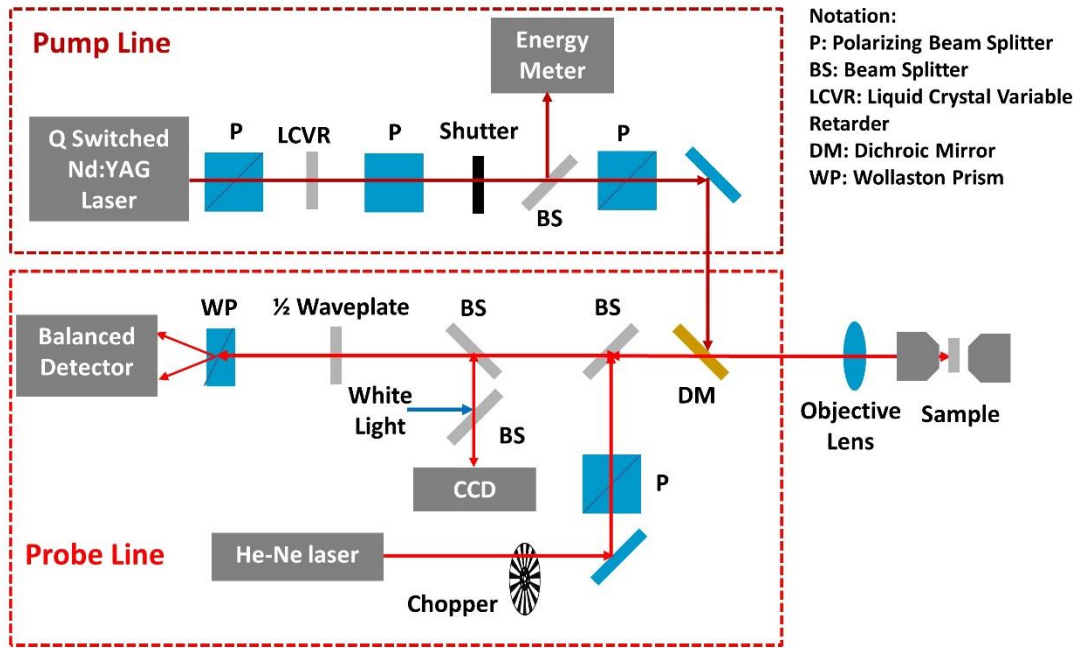


Figure 2.6 Optical path of Curie temperature distribution measurement system.

The pump laser was a Q-switched Nd:YAG laser from Standa Ltd. with 1064nm wavelength. The output pulse energy was 300 μJ /pulse with 10 Hz repetition rate, ~ 700 ps pulse width. Single pulse selection and accurate pulse energy control is essential to control the precise heating of sample. The pulse energy control system contained a liquid crystal variable retarder (LCVR, LC1221 from Thorlabs) between two polarizing beam splitters (PBS25-532-HP from Thorlabs). Figure 2.7 shows the optical path and principle of pulse energy control. The first polarizer ensures the input beam into LCVR was linearly polarized

in horizontal direction. The fast axis of the LCVR was fixed at 45° w.r.t. the horizontal direction, i.e. input light was separated into two equal components that polarized along fast axis and slow axis. The retardance of the LCVR was controlled by applied voltage to change the linearly polarized input light into elliptically polarized output light. The second polarizing beam splitter after the LCVR was set to pass the vertically polarized component of the elliptically polarized light. Since planes of incidence are different for two polarizing beam splitters, the polarization directions are referred with vertical and horizontal directions.

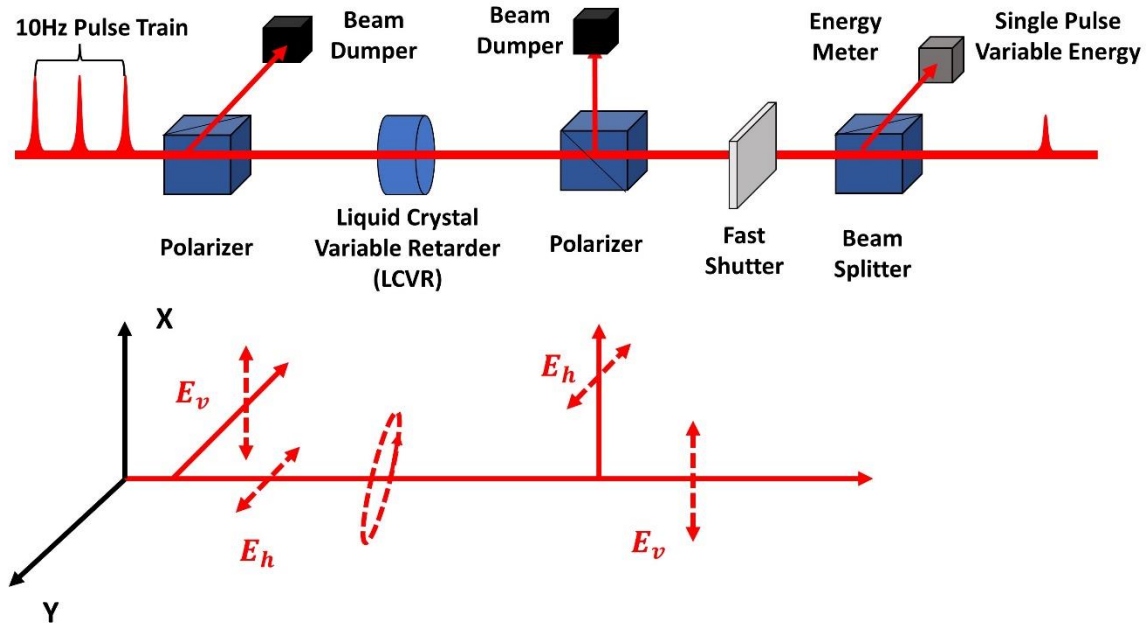


Figure 2.7 Pulse energy control system. Top: Optical path. Bottom: Change of the polarization state. Solid red line indicates the light propagation direction. Dashed red line indicates the polarization direction.

Figure 2.8 shows the pulse energy vs. LCVR voltage. The LCVR acts as a half waveplate around 1.5 V that rotates the horizontally polarized light into vertically polarized light, thus the output pulse energy reaches the maximum value. As the voltage goes higher, the retardance goes smaller and reduces the vertical components that will pass through the second beam splitter. The inner plot is the expansion of the curve from 1.5 V and 1.6 V, which shows the accurate control of pulse energy.

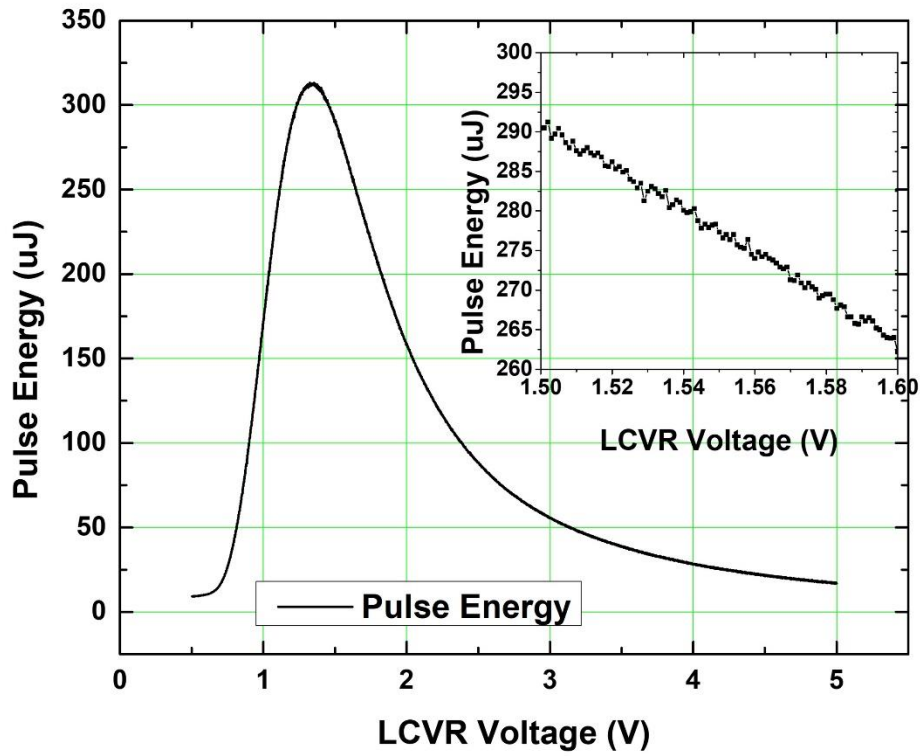


Figure 2.8 Pulse energy dependence on LCVR voltage.

After the pulse energy control part, single pulse was pick out by a fast-mechanical shutter synchronized with the laser output trigger. The open window of the fast shutter was 100 ms. The delay between the laser trigger and the shutter trigger was adjusted to allow single pulse through when the shutter was open. Half of the selected pulse was sampled by a non-polarizing beam splitter into an energy sensor to measure the pulse energy. Another

polarizing beam splitter was mounted on rotation mount to achieve proper pulse energy on the sample. The actual pulse energy on the sample was scaled by a ratio without affecting the measurement data, since the pulse energy is only a relative measurement of the media temperature.

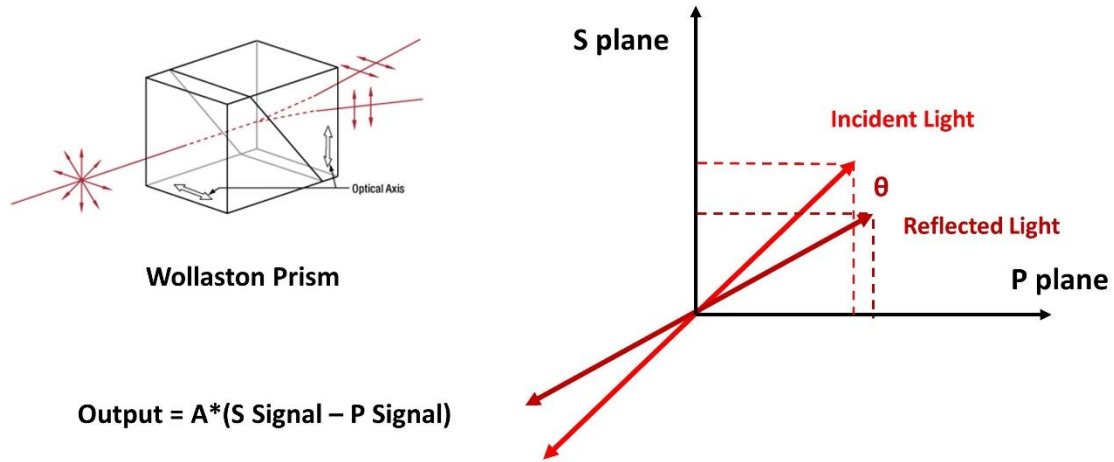


Figure 2.9 Schematic of balanced MOKE signal detection. Image of Wollaston prim is from Thorlabs.

The probe laser was a continuous He-Ne laser from JDSU. Incident probe beam was linearly polarized and chopped at 5 kHz for lock-in detection. The reflected probe beam was focused and passed through a Wollaston prism. The Wollaston prism will separate S-polarized light and P-polarized light in space for optical bridge detection. A balanced photodetector was used to detect and amplify the difference of S-polarized light and P-polarized light. As shown in Figure 2.9, before measurement, the polarization direction of incident beam was controlled by rotating the polarizer to balance the S component and P component. Once the polarization of reflected beam was changed due to the change of magnetic moment in probe region, the intensity of one component will decrease while the other component will increase. This balanced detection scheme can suppress the background noise and the common mode noise of the laser intensity to achieve high SNR

[55]. The amplitude of output signal was detected by a lock-in amplifier (SR830) that locked to the chopper frequency. A CCD camera was integrated into the probe line to inspect the sample surface and the overlapping of pump spot and probe spot.

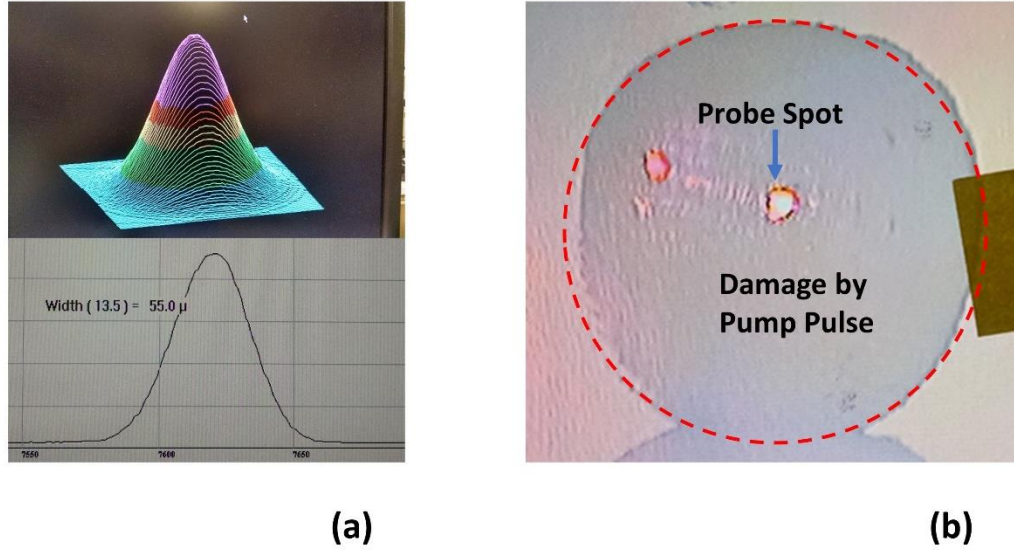


Figure 2.10 Spot sizes and overlapping of pump spot and probe spot. (a) Beam profile of probe spot. (b) Damage pattern of pump spot and overlapping with probe spot.

The pump beam and probe beam were combined by a short pass dichroic mirror (DMSP 1000 from Thorlabs), which passes 632 nm probe beam and reflects 1064nm pump beam. The combined beam was focused on the sample with a 10X objective lens. The spot size ratio of the pump beam and probe beam was controlled to be larger than 10:1, which ensures the probed region is uniformly heated by the pump laser. Figure 2.10 (a) shows the beam profile of probe laser with 55 μm spot size ($1/e^2$). Figure 2.10 (b) is the view of sample under camera. The red dot is the probe beam. The spot size of pump beam is inspected with the damage pattern created by the highest pump pulse energy. This damage pattern was also used to inspect the overlapping of pump spot and probe spot. After overlapping, the sample was translated to an undamaged location for measurement.

Figure 2.11 is the photo of the experimental system. The sample was mounted on a vertical sample holder with tilting adjustment capability. The sample holder was mounted on motorized stages for XYZ adjustment. An access hole for the objective was opened in one pole of the magnet. The maximum magnetic field with air cooling was 11.4 kOe.

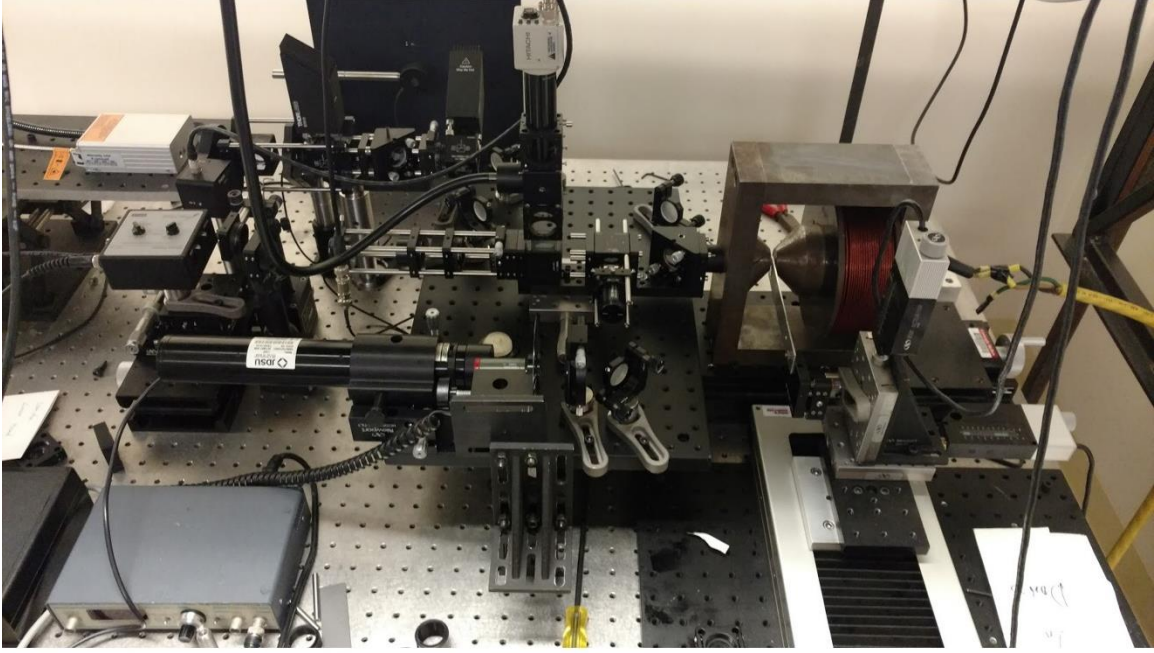


Figure 2.11 Photo of pump-probe Curie temperature distribution measurement system.

2.3 Curie Temperature Distribution of HAMR Media

One important factor of T_c distribution arises from the surface effect. For $L1_0$ FePt grains, ferromagnetic exchange fields on surface spins are smaller than that of the spins in the core due to the break of symmetry. T_c is the temperature when thermal agitation can balance the exchange interaction. As the grain size goes smaller, the variation of surface-to-volume ratio is more significant and results in larger σ_{T_c} . In this section, the T_c distribution study will be performed on two types of HAMR media. One is the HAMR

media from industrial sponsors with different grain heights, the other one is HAMR media with magnetic oxide grain boundary which was proposed to reduce T_c distribution [54].

2.3.1 Curie Temperature Distribution of HAMR Media with Different Grain Heights

HAMR recording media with different grain heights were provided by our industrial sponsors [51]. The grains size and average T_c increases with increasing grain height and the T_c distribution is supposed to increase with increasing surface volume ratio [51].

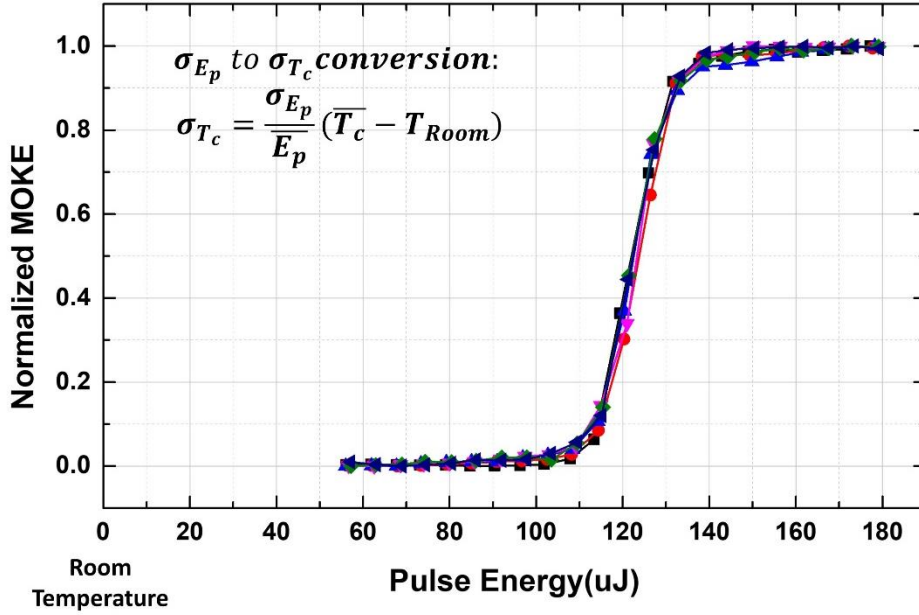


Figure 2.12 Example of measured switching curves on one sample.

Figure 2.12 shows an example of measured switching curves on one of the samples. The horizontal axis is the pulse energy and the vertical axis is normalized MOKE signal. Different curves are repeated measurements to reduce the measurement error through averaging. The measurements show excellent SNR and repeatability. The switching curve shows the distribution of T_c is very similar to Gaussian distribution as assumed in Section 2.1. However, the media temperature can't be directly measured, but the temperature raise starts from room temperature is proportional to the pulse energy. The direct fitting of the

experimental data gives the switching pulse energy distribution σ_{E_p} and the average switching pulse energy $\overline{E_p}$. σ_{T_C} can be calculated with Equation 2.4.

$$\sigma_{T_C} = \frac{\sigma_{E_p}}{\overline{E_p}} (\overline{T_C} - T_{room}) \quad (2.4)$$

where T_{room} is the room temperature. The average Curie temperature $\overline{T_C}$ that can be measured with commercial magnetometers, such as MPMS-3. In Equation 2.4, σ_{T_C} is evaluated in unit of Kelvin.

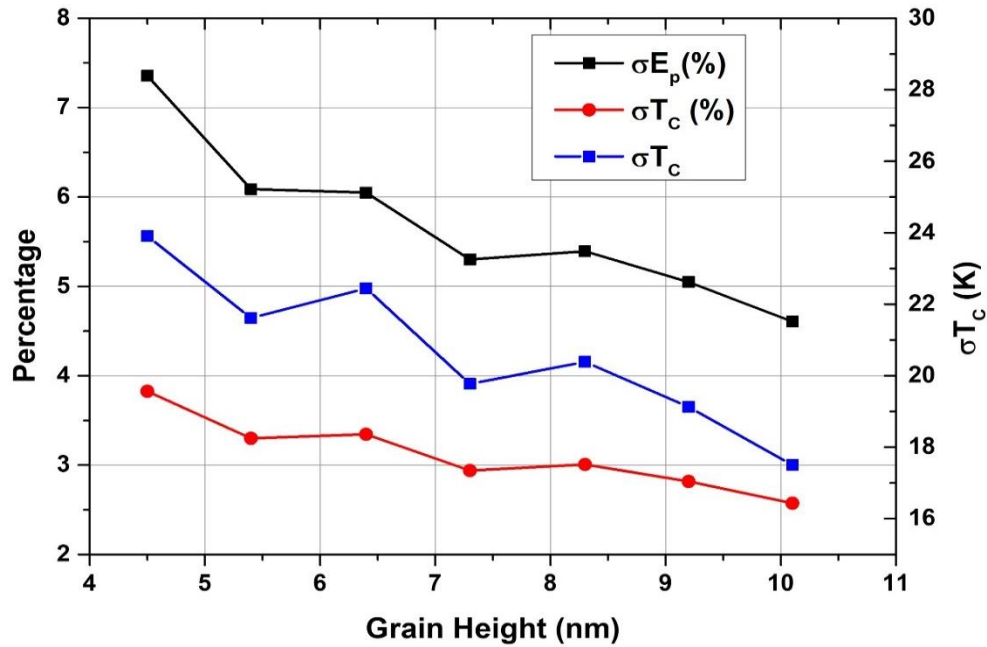


Figure 2.13 Curie temperature distribution of HAMR media with different grain heights.

Same measurements were performed on all HAMR samples with different grain heights. σ_{E_p} and $\overline{E_p}$ of every single measurement were evaluated from fitting to Equation 2.2 then converted to σ_{T_C} with Equation 2.4. Figure 2.13 summaries the results of T_C distribution measurements. The black curve shows the σ_{E_p} evaluated in percentage vs. grain heights. The blue line is σ_{T_C} evaluated in Kelvin. The red line is the relative value of σ_{T_C} (w.r.t $\overline{T_C}$) in percentage. As show in the figure, both the absolute value and relative value of the σ_{T_C}

increases with decreasing grain heights, which agrees with the increasing trend of surface to volume ratio as the grain size also decrease with decreasing grain height [51].

2.3.2 Curie Temperature Distribution of HAMR Media with Magnetic Oxide Grain Boundary

The straightforward way to control the grain-to-grain T_C variation is controlling the grain size distribution. However, controlling grain size distribution becomes more challenging when the mean grain size gets smaller. Here, an alternative way to reduce the T_C dependence on grain size was proposed. The idea is coupling the surface spins with magnetic grain boundary materials that have higher T_C than of that of FePt. $\text{BaFe}_{12}\text{O}_{19}$ is a ferrimagnetic material with high T_C (> 800 K) [56] and relatively low thermal conductivity 4 W/m/K [57]. The T_C distribution of HAMR media with mixed BaFe_xO_y and C as the new grain boundary material is studied. The films were fabricated by Bing Zhou. XRD, magnetic properties and TEM analysis were performed by Bing Zhou and B. S. D. Ch. S. Varaprasad [54].

All films were sputtered on thermally grown SiO_2 substrates with AJA system. The base pressure was less than 2×10^{-9} Torr. Two series of samples C1, C2, C3 and T1, T2 with film stack SiO_2/Ta (5 nm)/Cr (100 nm)/MgO (9 nm)/magnetic media (M) (7.5 nm) were prepared. All samples have the same structure except for the magnetic media. In the first series of samples, the media layer M is FePt-X vol.% C, where $X = 30, 32$ and 35 for C1, C2 and C3, respectively. In the second series, the media layer M is FePt-X vol. % (C+ $\text{BaFe}_{12}\text{O}_{19}$) where $X = 40$ and 42 , for T1 and T2, respectively. The Ta and Cr layers were DC sputtered at 5 mTorr at room temperature and 200°C , respectively. They were subsequently annealed in vacuum at 650°C for 40 min. The Cr buffer layer is used to

obtain large MgO grains with a strong (002) texture and to serve as the heat sink. The MgO layer was RF sputtered at 10 mTorr at room temperature. The sample was then preheated at 650 °C for 30 min to stabilize the deposition temperature of media layer M. The FePt alloy target and the C target were subsequently DC sputtered with the RF-sputtered BaFe₁₂O₁₉ target onto the pre-deposited MgO at 5 mTorr at 650 °C.

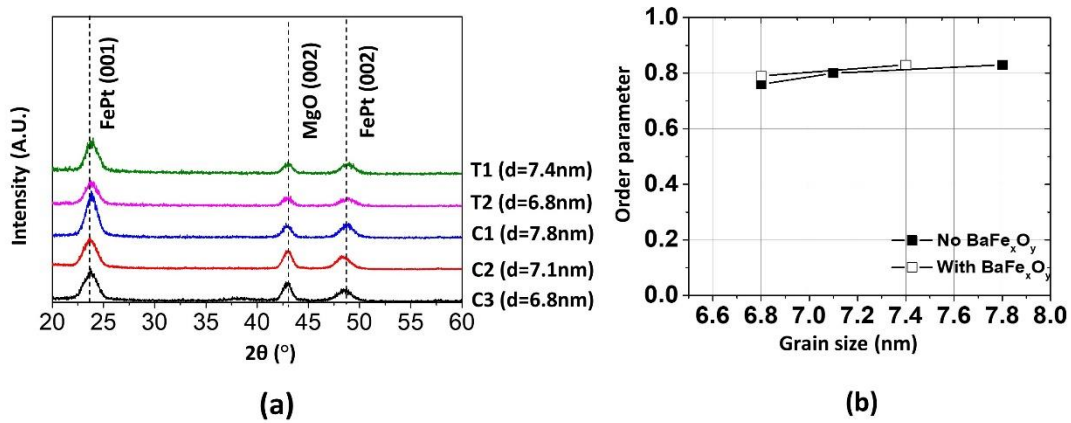


Figure 2.14 (a) XRD patterns of C1 - C3 and T1 - T2. (b) Order parameter of C1 - C3 and T1 - T2 vs. grain size

Figure 2.14 (a) shows the XRD patterns of C1-C3 and T1-T2, with the MgO and FePt peaks indexed. All samples show only FePt (001) and FePt (002) peaks indicating a well-textured FePt growth on the MgO with and without BaFe_xO_y. The large integrated intensity ratio between the super lattice peak FePt (001) to the fundamental peak FePt (002) in all samples demonstrate good chemical ordering in L1₀ FePt. The order parameter (S) was plotted vs. grains size in Figure 2.14 (b). S was calculated from the ratio of I_{001}/I_{002} with the absorption factor and Lorentz factor taken into account, where I_{001} and I_{002} are integrated intensity of FePt (001) and (002) peaks, respectively [58]. The mean grain size was obtained from the in-plane bright field TEM images. As shown in the figure, the S of C series shows a slight decreasing trend with decreasing grains size, when the carbon volume percentage increases from 30 to 35. This is due to the increasing surface to volume

ratio caused by grain size reduction as the carbon volume percentage increases. S of the T series of samples follows the same trend as C series. The chemical ordering of FePt remains constant with BaFe_xO_y added to the media layer, suggesting that FePt is chemically inert to BaFe_xO_y .

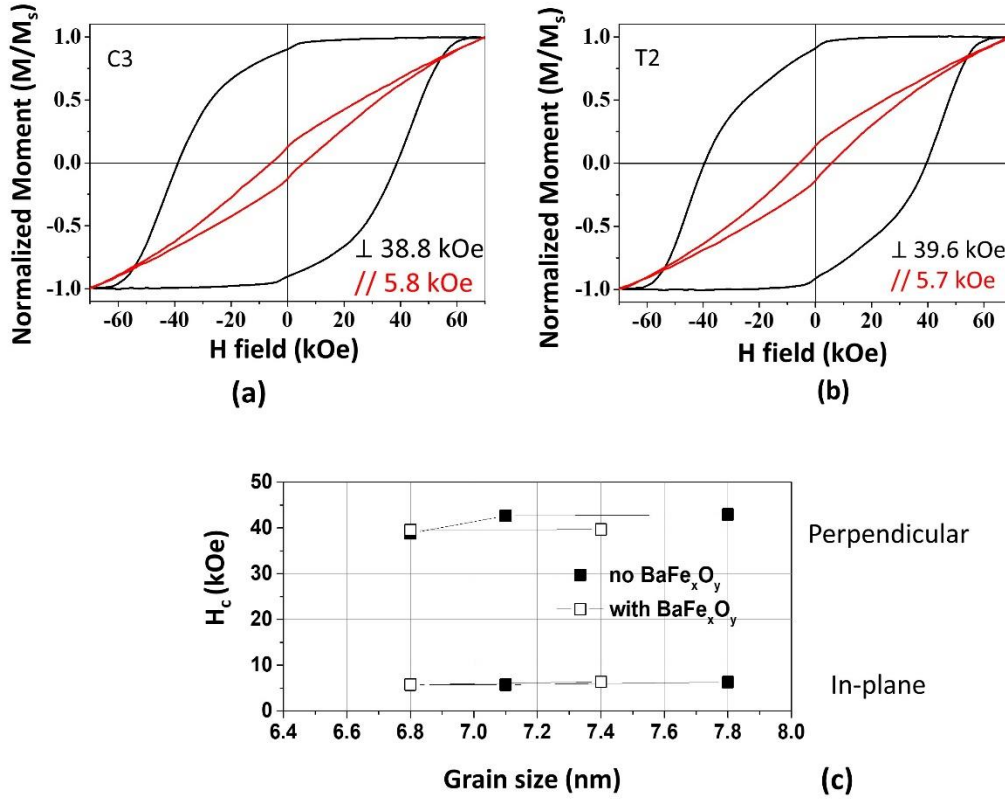


Figure 2.15 (a) Perpendicular and in-plane MH loops of C3. (b) Perpendicular and in-plane MH loops of T2. (c) Dependence of perpendicular and in-plane coercivity on grain size.

Figure 2.15 (a) and (b) show the typical perpendicular and in-plane MH loops for samples with (T2) and without BaFe_xO_y (C3) at room temperature. T2 and C3 have a similar average grain size of 6.8 nm. Figure 2.15 (c) shows the dependence of the perpendicular and in-plane coercivity on grain size of the samples with and without BaFe_xO_y . All samples show high perpendicular coercivity ranging from 38 kOe to 42 kOe,

suggesting good L1₀ ordering of FePt films with and without BaFe_xO_y. The in-plane MH loops of all samples show a small opening with coercivity < 7 kOe and normalized remanence magnetization < 0.14 which indicates the c-axis of FePt grains are predominantly perpendicular to the film plane. The coercivity and squareness of the perpendicular MH loop of sample C3 and T2 are similar, which concludes the BaFe_xO_y does not strongly exchange couple the adjacent FePt grains. Both the XRD and MH measurements proves the microstructure of the media was well maintained with BaFe_xO_y added as grain boundary material.

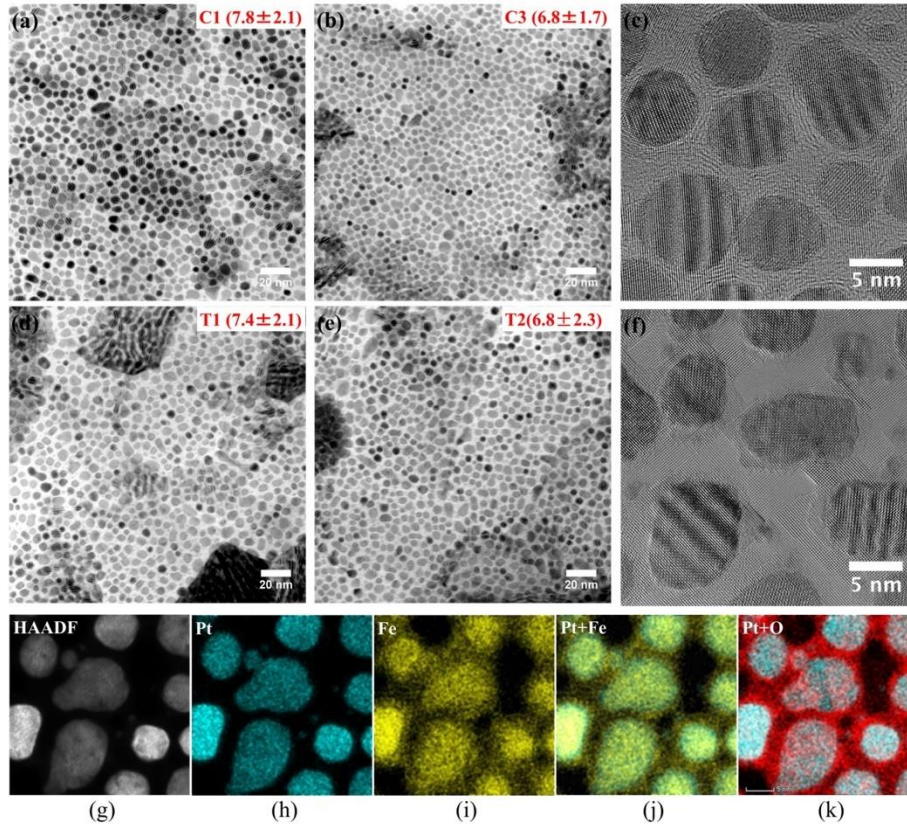


Figure 2.16 The in-plane bright field TEM images for (a) C1, (b) C3, (d) T1, and (e) T2 with the insets being their corresponding average grain size and standard deviation. The high resolution TEM images for (c) C1 (FePt - 30 vol. % C) and (f) T1 (FePt - 40 vol. % (C + BaFe_xO_y)). The high angle annular dark field (HAADF) images (g) and the EDS mapping of (h) Pt, (i) Fe, (j) Pt + Fe, and (k) Pt + O of T1 (FePt - 40 vol. % (C + BaFe_xO_y)).

Figures 2.16 (a), 2.16 (b), 2.16 (d) and 2.16 (e) show the in-plane bright field TEM images of C1, C3, T1 and T2, respectively. The in-plane bright field TEM image of C2 is not shown here. All samples show a well-separated granular microstructure. The grain size analysis was performed on multiple regions from each sample to ensure the accuracy. The mean grain size of FePt decreases gradually from 7.8 nm to 6.8 nm as the volume fraction of the grain boundary material (C) increases from 30 vol.% to 35 vol.% in samples C1 to C3. For T1 and T2, the grain size of FePt decreases from 7.4 nm to 6.8 nm as the volume fraction of grain boundary materials (C and BaFe_xO_y) increases from 40 vol.% to 42 vol.% . The in-plane microstructure of 7.5 nm FePt-30 vol.% BaFe_xO_y was also examined (result not shown), and it shows an interconnected microstructure similar to other oxides such as SiO₂ and TiO₂ shown in Reference [59]. Therefore, the C content is crucial to control the microstructure. Figures 2.16 (c) and 2.16 (f) show the HR-TEM images for C1 and T1, respectively. As shown in the images, the FePt grains are enclosed with graphitic regions followed by amorphous carbon, whereas for FePt-BaFe_xO_y-C media, connecting crystalline shells are found around the FePt grains. To find where BaFe_xO_y resides in the media layer, elemental mapping of Fe, Pt and O was performed on the sample with BaFe_xO_y. The elemental mapping of Ba is not used in this study, since the overall atomic percentage of Ba is too low to be detected. Figures 2.16 (g) - 2.16 (k) show the HAADF-STEM and corresponding EDS mappings of Fe and Pt of the FePt- BaFe_xO_y -C media. The chemical mapping of Pt shows the well-defined grains as FePt grains, which suggests that the Pt lies only in the FePt grains. The chemical mapping of Fe shows that Fe exists not only in FePt grains but also in the grain boundary. Figures 2.16 (j) and 2.16 (k) show the overlapped EDS mappings of Fe-Pt and Pt-O which clearly shows a crystalline shell

surrounding FePt grains with a significant amount of Fe and O. Therefore, it can be concluded that BaFe_xO_y the media layer forms a crystalline shell surrounding FePt grains and the shells are connected with each other.

Through the analysis of the XRD patterns, the room temperature magnetic properties, and the microstructure, it can be concluded that FePt with BaFe_xO_y -C added in the media layer forms a crystalline shell surrounding FePt grains and it does not chemically interact with FePt nor strongly exchange couple the adjacent FePt grains.

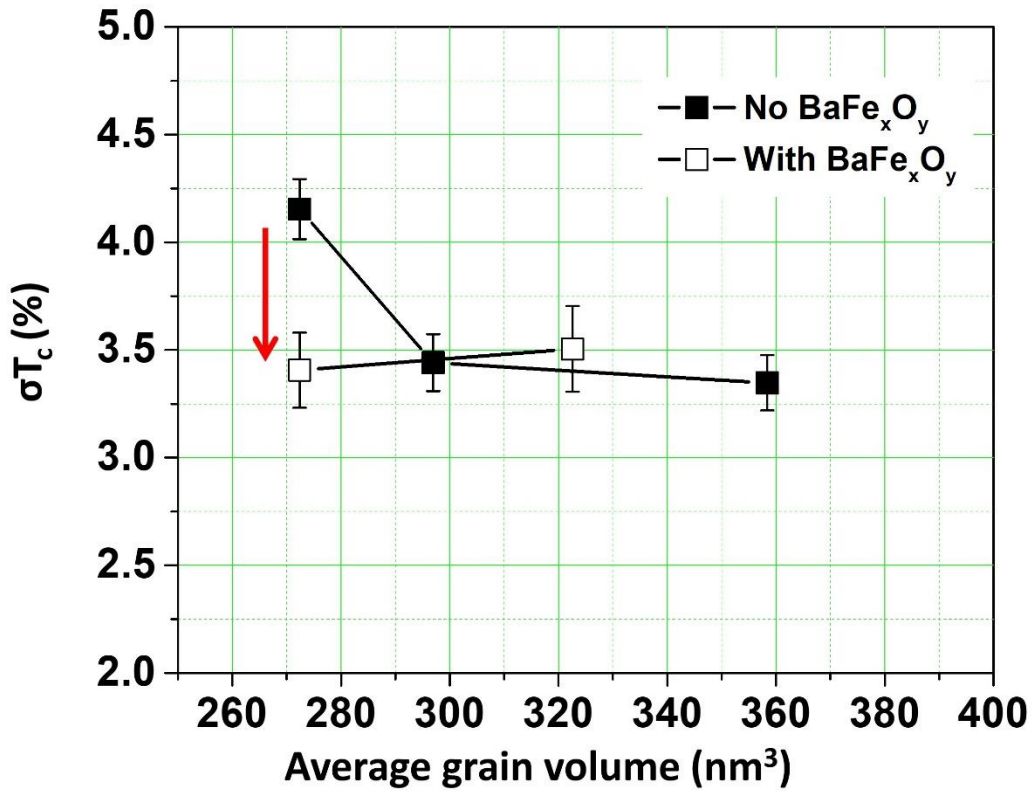


Figure 2.17 Curie temperature distribution as a function of average grain volume for FePt-C and FePt- BaFe_xO_y -C media.

The switching curves were measured with the pump-probe system on at least five different locations for each sample. The negative saturation field was 6 kOe and the switching curves were measured without $H_{external}$. Figure 2.17 shows the dependence of T_c distribution as a function of grain volume. The solid squares represent C1, C2 and C3

and open squares represents T1 and T2. The measured σ_{T_C} for FePt-C media C1-C3 increases significantly as the grain volume reduces. In comparison, σ_{T_C} of FePt-BaFe_xO_y-C media shows a 0.7% reduction in σ_{T_C} at smaller grain volume. It can be inferred that the addition of BaFe_xO_y in the media layer could have even larger effect at smaller grain size because of the hyperbolic increase in surface to volume ratio as the grain diameter reduces.

2.4 Measurement of Temperature Dependence of Anisotropy

Field

The temperature dependence of anisotropy field ($H_k(T)$) around T_C is another important property of HAMR media, since it determines the effective field gradient in HAMR. Based on the T_C distribution measurement, a novel way to measure $H_k(T)$ around T_C will be proposed and demonstrated.

2.4.1 Methodology of $H_k(T)$ Measurement

The $H_k(T)$ can be described by Equation 2.5 [60][61].

$$\frac{H_k(T)}{H_k(0)} = \left(\frac{M_s(T)}{M_s(0)} \right)^{n-1} \quad (2.5)$$

where $M_s(T)$ and $M_s(0)$ are the saturation magnetization at temperature T and 0 K, respectively. $H_k(T)$ and $H_k(0)$ are the anisotropy field at temperature T and 0 K, respectively. n is the parameter that determines the trends of $H_k(T)$. In T_C distribution measurement, the switching curve was measured either without external field or with very small $H_{external}$, the switching happens when the grain temperature is heated to T_C . However, when the $H_{external}$ is high enough to counter balance a significant part of the H_k , the switching will start at lower temperature when the strength of H_k is reduced to the

strength of $H_{external}$. As shown in Figure 2.18, the black line shows the normalized $H_k(T)$ and the dashed lines indicate the strength of $H_{external}$, both of them are normalized with room temperature H_k . When H_k is reduced to the magnitude of $H_{external}$ through heating the media to T, the total field will be zero. T will be the temperature at which the switching starts. T_C distribution measurement can give the average switching energy which can be scaled to get average switching temperature $T_{switching}$, thus $H_{external}(T_{switching})$ represents the relationship of $H_k(T)$. In other words, $H_{external}$ is assumed to be equal to H_k at switching point, the temperature is identified by the media temperature scaled by pulse energy.

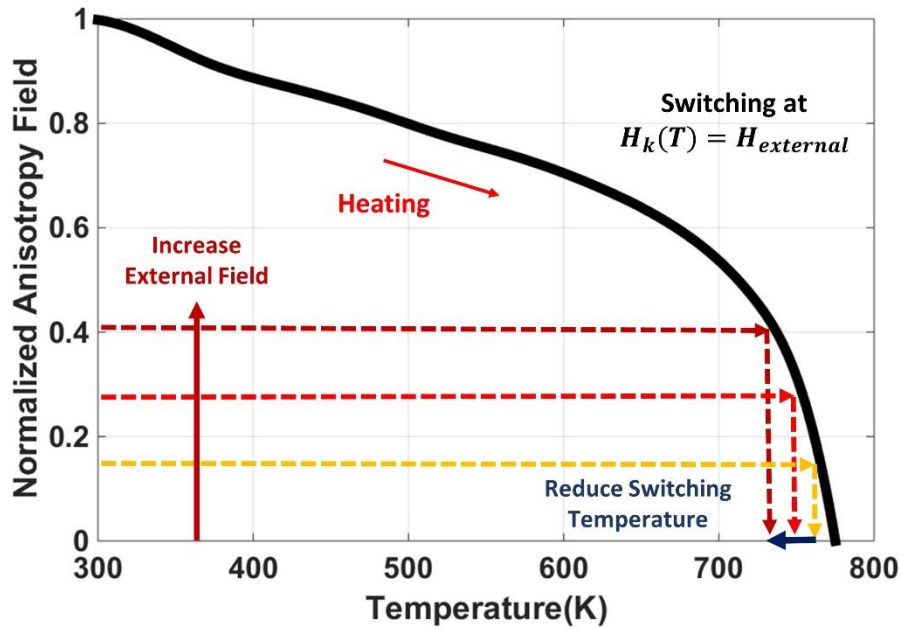


Figure 2.18 Temperature dependence of anisotropy field.

The feasibility of the methodology was studied with micromagnetic simulation. The simulation was performed with 775K \bar{T}_C with no T_C distribution. Figure 2.19 shows two typical simulated switching curves with zero and 70 kOe external fields. As shown in the figure, a sharp transition happens when the media was heated to 775 K with zero external field. With 70 kOe external field, the switching starts from significantly lower temperature

as expected. What's more, the transition region spans over a wide temperature range. This phenomenon comes from the thermal agitation effect since large $H_{external}$ reduced the energy barrier significantly, a slight increase of the thermal agitation will trigger the flipping of moment. Note, the final media state with $H_{external}$ is positively saturated.

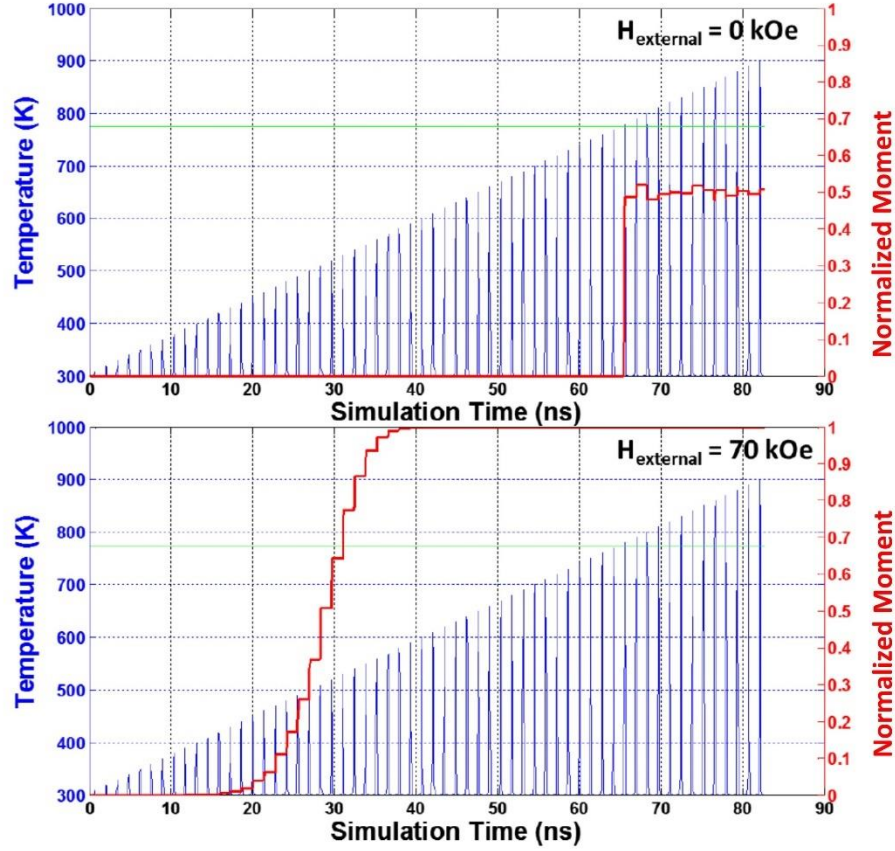


Figure 2.19 Switching curve simulation with different external fields.

The switching curves were simulated with different external fields and different n of the media. The average switching temperatures were extracted to get $H_{external}(T_{switching})$ that stands for $H_k(T)$. Figure 2.20 shows the comparison of the simulation results and preset $H_k(T)$. The red and black lines are the preset $H_k(T)$ for $n=2$ and $n=3$. The blue and purple lines with symbols are the fitting values from simulated switching curves. The fitting values show a good matching with the preset values around T_C . However, the

deviation becomes larger as the external field $H_{external}$ goes higher where the thermal agitation starts to play a more significant role and reduce the switching temperature.

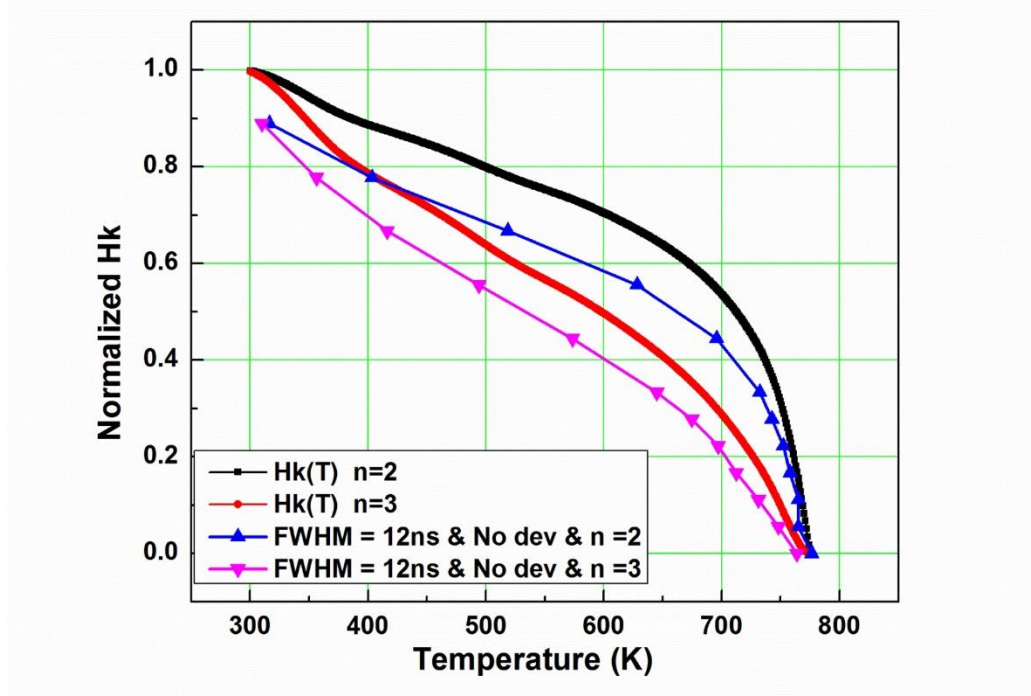


Figure 2.20 Comparison of simulated $H_k(T)$ measurement results with preset media property.

The thermal agitation effect was further studied with different heating pulse widths. The pulse widths were set to be 0.12 ns, 1.2 ns and 12 ns for simulation. Figure 2.21 shows the deviation between preset and extracted temperature at same normalized H_k ($H_{external}$ in simulation) with different pulse widths. The horizontal axis is the normalized H_k , which is also the $H_{external}$ during simulation. The vertical axis is the deviation between preset T and extracted $T_{switching}$. For all results with different pulse widths, the deviation increases with increasing $H_{external}$. Shorter heating pulse width can reduce the deviation significantly. They all have good agreements when $H_{external}$ is less than 30% of H_k . The pump-probe method was proved to be feasible to measure the temperature dependence of anisotropy field especially around T_C .

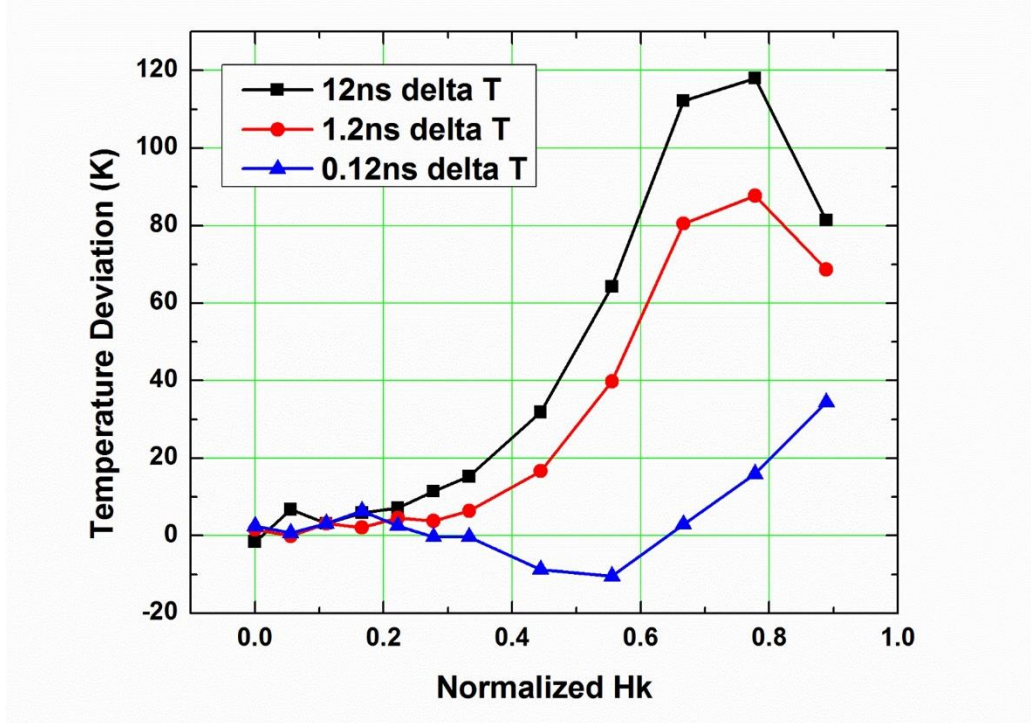


Figure 2.21 Deviation between preset and extract temperature vs. normalized H_k .

2.4.2 Example of $H_k(T)$ Measurement

Two prototype measurements were performed with HAMR recording media. Figure 2.22 shows the switching curves measured with different external fields. All measurements were performed at same location without adjustment to the optical path and sample. The measurements were performed with the first-generation experimental system [25] which had larger noise than the most advanced system shown in Section 2.2. As shown in the figure, the switching curve shifts towards low pulse energy direction with increasing $H_{external}$, which indicates the switching happens at lower temperature with the shifting rate determined by $H_k(T)$.

Figure 2.23 shows the fitting of experimental data to the CDF function, the black cross is the point with 50% switched moment, the corresponding pulse energy was used to represent the average switching temperature.

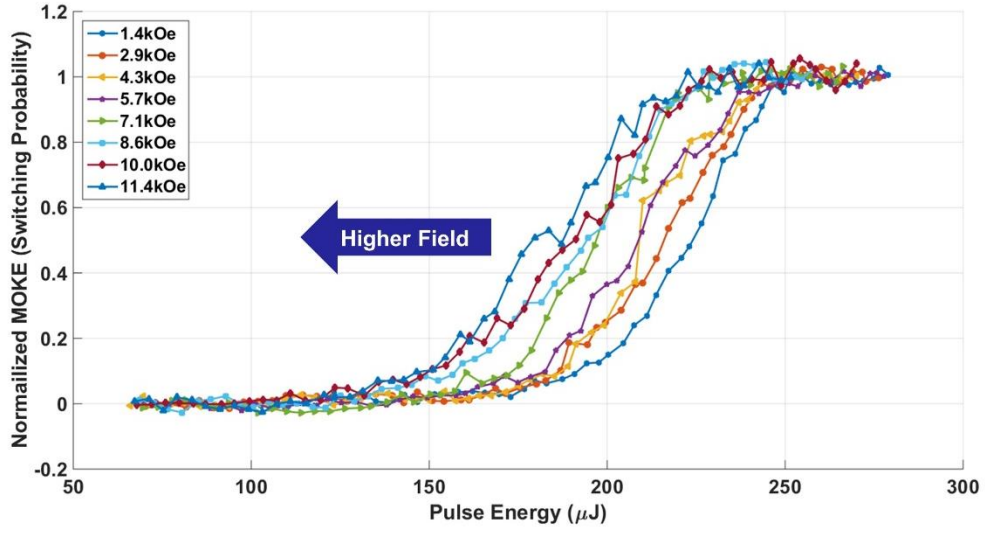


Figure 2.22 Normalized switching curves measured with different external field.

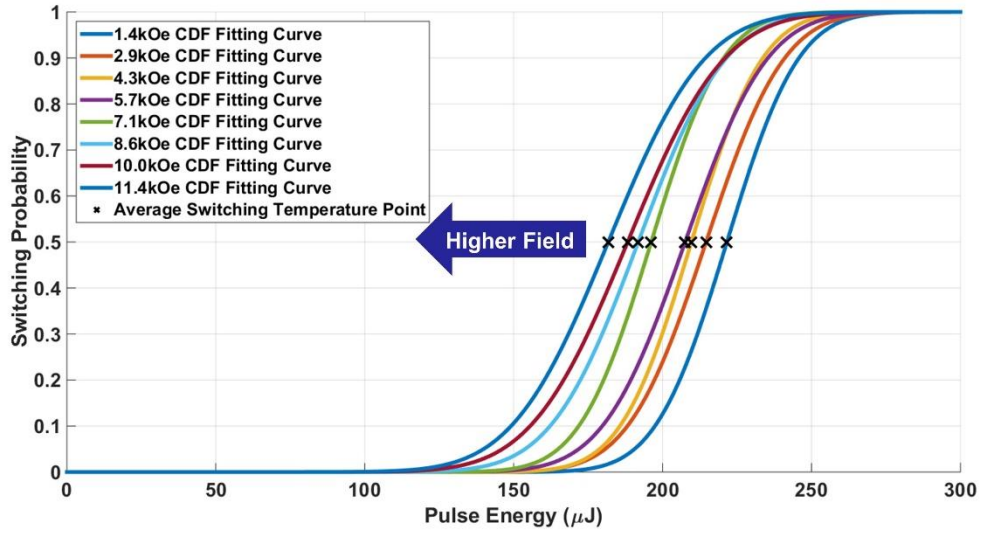


Figure 2.23 Fitting results of measured switching curves with different external field.

Figure 2.24 shows the external field vs. normalized temperature. The inner plot shows the measured result with normalized temperature starts from room temperature. As shown in the figure, sample 1 has sharper $H_k(T)$ dependence around normalized Curie temperature than sample 2.

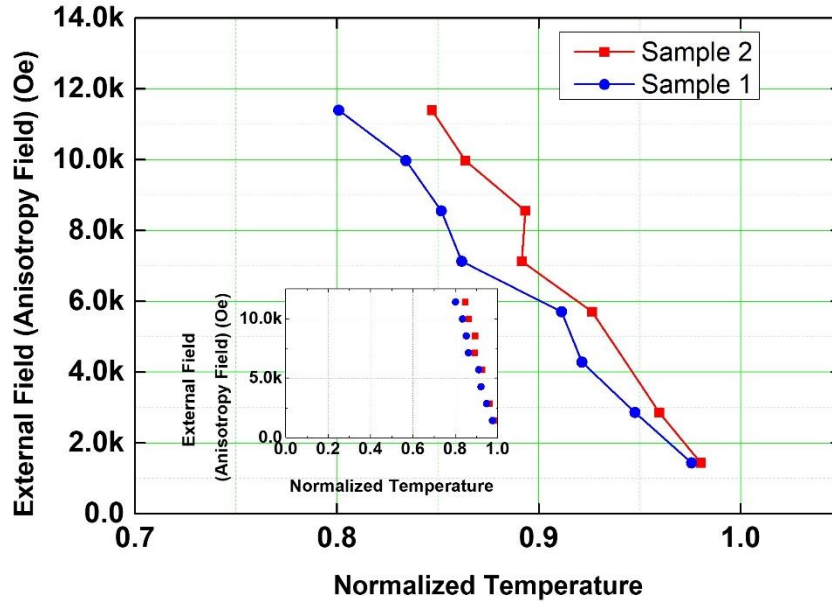


Figure 2.24 H_k (external field) dependence on normalized temperature.

In this chapter, the methodology for T_C distribution measurement was analyzed and validated with micromagnetic modeling. The pump-probe experimental system was successfully built to measure the T_C distribution and temperature dependence of anisotropy field around T_C . $L1_0$ -FePt HAMR media with $BaFe_xO_y+C$ magnetic oxide grain boundary was proposed and fabricated to suppress T_C distribution. Thorough study shows the T_C distribution was well reduced without affecting the magnetic properties and microstructure of the $L1_0$ FePt with $BaFe_xO_y+C$ grain boundary. The pump-probe system was extended to measure $H_k(T)$ relationship near T_C for the first time.

3 Simulation Study of Magnetic Dynamics Induced by Ultrafast Laser Heating

This chapter will study the magnetic dynamics induced by ultrafast laser heating through micromagnetic simulation. Two temperature models will be used to simulate the thermal effect induced by femtosecond laser heating. The simulation will be performed with two types of films, (1) films with perpendicular anisotropy, (2) films with no anisotropy, to understand and guide the experimental work. The phenomenal model to analyze the experimental data is validated with the simulation results.

3.1 Modeling of Magnetic Dynamics Induced by Ultrafast Laser Heating

3.1.1 Two Temperature Model

TRMOKE based on ultrafast laser is a useful tool to excite and detect the magnetic dynamics. The basic excitation of magnetic dynamics in metallic magnetic film comes from the heating effect. Two temperature model is commonly used to describe the thermal dynamics [42], [43]. In two temperature model, the film is separated into two systems, the electron system and the photon system. Since the spin and the charge are both intrinsic properties of electron, the temperature that affects the magnetic properties is treated same as electron temperature [63], [64].

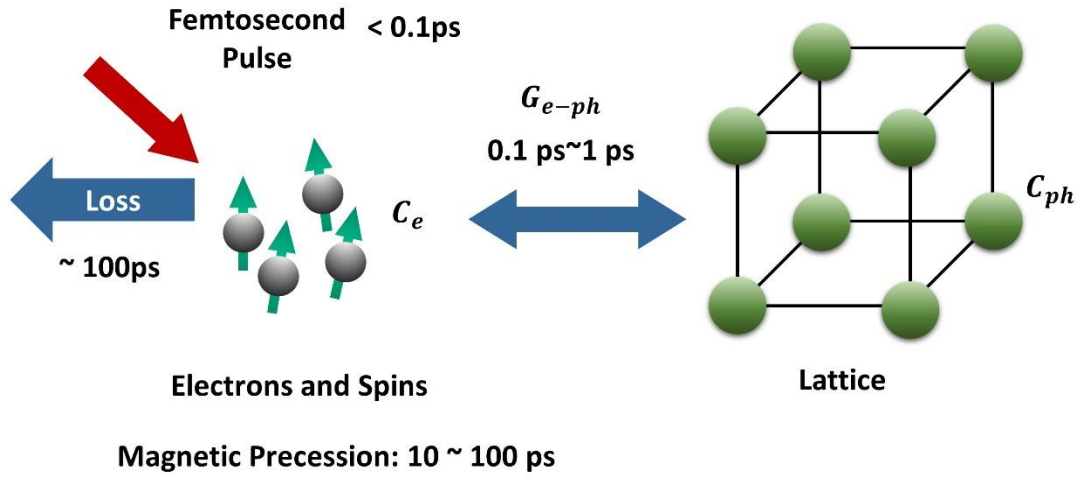


Figure 3.1 Interaction of femtosecond laser with metallic magnetic film based on two temperature model.

Figure 3.1 shows the interaction of femtosecond laser with metallic magnetic film. The pulse width of femtosecond laser is about 0.1 ps. Due to the nature of electromagnetic wave, femtosecond pulse first interacts with the free electrons in the film and heats up the electrons. Then the electrons start to transfer the energy to the phonons through electron-photon interaction. G_{e-ph} is the coupling constant that determines the energy exchange rate between the electron and phonon systems. The time scale of electron-phonon interaction is in several ps. Then the electron temperature T_e and phonon temperature T_{ph} will reach equilibrium and cool down through the heat dissipation to the environment. The time scale of heat dissipation is usually in several hundred of ps. Equation 3.1 is the quantitative description of two temperature model.

$$\begin{aligned}
 C_e \frac{dT_e}{dt} &= -G_{e-ph}(T_e - T_{ph}) + P(t) - C_e \frac{T_e - T_{room}}{\tau_{ph}} \\
 C_{ph} \frac{dT_{ph}}{dt} &= G_{e-ph}(T_e - T_{ph})
 \end{aligned} \tag{3.1}$$

where t is the evolution time, C_e and C_{ph} are the specific heat of electron and phonon, respectively, $P(t)$ is the energy input rate from the femtosecond laser heating. τ_{ph} is the

heat dissipation rate to the environment. The C_e is assumed to be linearly proportional to T_e which is $\gamma_e T_e$ [64]. C_{ph} is assumed to be constant [63]. Typical values were chosen from References [63], [64] for simulation as listed in Table 3.1. $P(t)$ is assumed to follow a Gaussian profile in time domain with 0.1 ps pulse width (FWHM) [65], the peak power was adjusted to mimic different E_p . Unit volume was assumed for simulation.

Table 3.1 Values for two temperature model simulation.

Parameter	Value
γ_e	$2 \times 10^3 \text{ Jm}^{-3}\text{K}^{-2}$
C_{ph}	$7.5 \times 10^5 \text{ Jm}^{-3}\text{K}^{-1}$
G_{e-ph}	$1.5 \times 10^{17} \text{ Wm}^{-3}\text{K}^{-1}$
τ_{ph}	100 ps
T_{room}	300 K

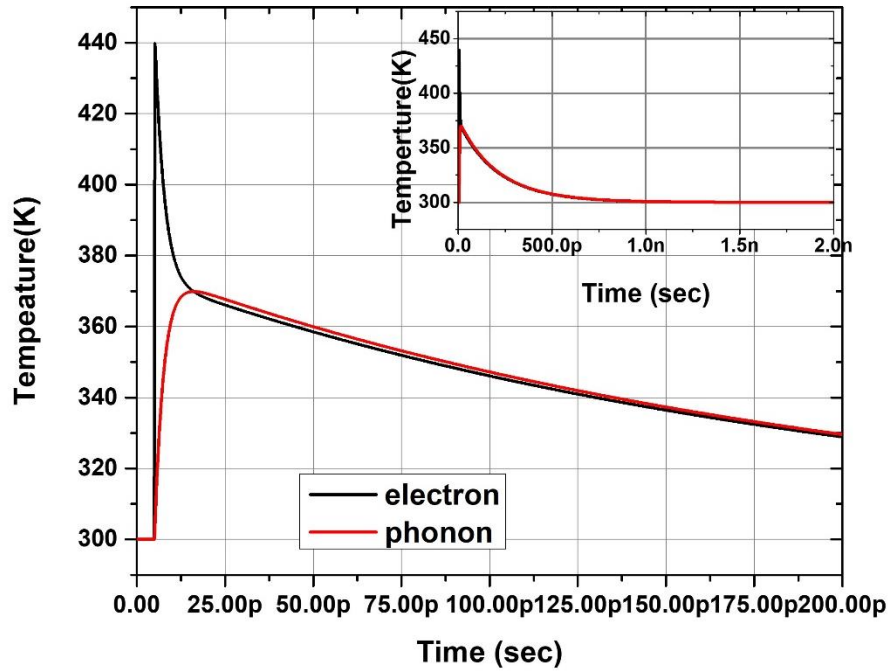


Figure 3.2 Two temperature model simulation of electron temperature and phonon temperature.

Figure 3.2 shows the temperature profiles of electron temperature and phonon temperature in time domain with femtosecond laser heating. The electron is heated up instantly in < 1 ps through the direct interaction with femtosecond laser pulse. In a few ps, T_e starts to decrease while T_{ph} starts to increase through the coupling between electron and phonon. T_e can reach higher value than T_{ph} due to the smaller specific heat of electron than that of phonon. T_e and T_{ph} reach equilibrium in about 10 ps then decrease simultaneously. The system will reach room temperature in about 1 ns as shown by the inner plot in Figure 3.2.

3.1.2 Magnetic Dynamics and Kittel Model

In TRMOKE, femtosecond laser is employed to excite the magnetic dynamics through heating and the magnetic moment was detect through MOKE. The pump-probe scenario of magnetic dynamics can be illustrated by Figure 3.3.

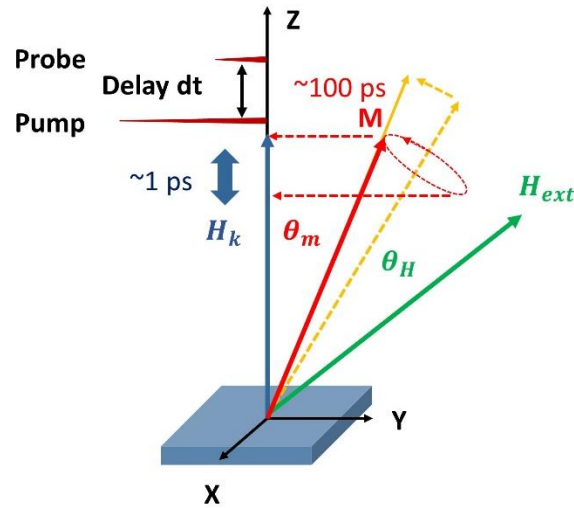


Figure 3.3 Schematic of magnetic dynamics induced by femtosecond laser in the magnetic thin film with perpendicular anisotropy.

The magnetic film is assumed to have perpendicular anisotropy and saturated in perpendicular direction. When an external field $H_{external}$ is applied at an angle θ_H w.r.t. the film normal. The magnetic moment M will be tilted away from perpendicular direction to the equilibrium direction θ_m w.r.t. Z direction, which is also the direction of total field H . When the media is heated with femtosecond laser, the media temperature is raised up in several ps. The magnetic properties that depend on temperature, such as $M_s(T)$ and $H_k(T)$, are also changed instantly, which leads to a new equilibrium direction as shown by the dashed yellow line in Figure 3.3. However, the time scale of magnetic dynamics is several tens of ps, the magnetic moment will follow the LLG equation and starts to precess around the new equilibrium direction. As the media cools down, H will gradually goes back to the initial state with the magnetic moment precessing around and damping towards it. After the excitation, a probe beam split from the same pulse with pump pulse arrives at the sample with a time delay dt to detect the M_z component with MOKE. The magnetic dynamic process $M(t)$ can be recorded by scanning dt .

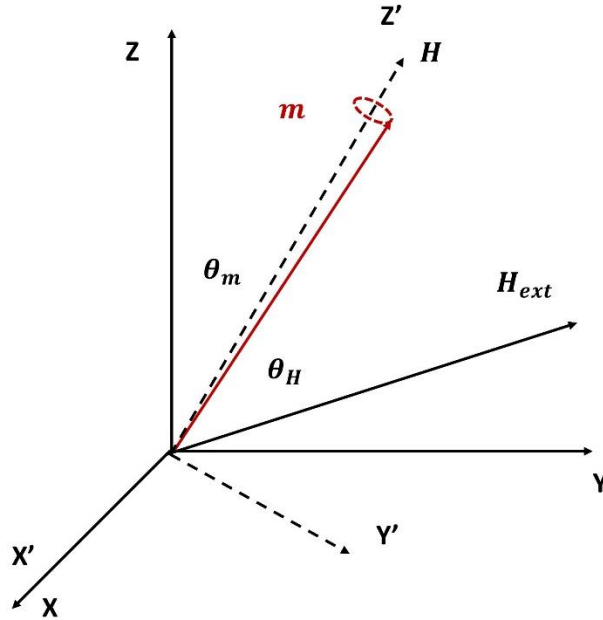


Figure 3.4 Schematic for Kittel model derivation.

In TRMOKE, the deviation of the magnetic moment and the effective field is about 1 degree, thus small angle approximation can be used to analyze the magnetic dynamic behavior. Figure 3.4 shows the equilibrium state and small angle approximation for dynamic analysis. $H_{external}$ is assumed to lie in YZ plane at θ_H w.r.t Z direction. Then M also lies in YZ plane at θ_m w.r.t Z axis. The total energy E_{total} of the system can be described by Equation 3.2.

$$E_{total} = -K_{eff}V \cos^2 \theta_m - H_{external}M_sV \cos(\theta_m - \theta_H) \quad (3.2)$$

where K_{eff} is the effective anisotropy energy which includes shape anisotropy, magneto crystal anisotropy and interfacial anisotropy. V is the grain volume. The first term is the anisotropy energy, the second term is the Zeeman energy from $H_{external}$. H can be expressed by Equation 3.3

$$H = \begin{cases} 0 \\ H_{external} \sin \theta_H \\ H_{external} \cos \theta_H + H_k^{eff} \cos \theta_m \end{cases} \quad (3.3)$$

where H_k^{eff} is the effective anisotropy field which equals to $\frac{2K_u}{M_s} - 4\pi M_s$. The first term come from the uniaxial perpendicular anisotropy from spin-orbital coupling (crystal or interfacial), the second term comes from shape anisotropy, i.e. demagnetization field in Z axis. The effective anisotropy constant K_{eff} can be express by Equation 3.4.

$$K_{eff} = \frac{H_k^{eff} M_s}{2} \quad (3.4)$$

Taking the derivative of total energy (Equation 3.2) can solve for θ_m in equilibrium state where $\frac{dE_{total}}{d\theta_m} = 0$.

When M precesses around H with a small amplitude, the dynamic process can be solved in the coordinate of $X'Y'Z'$ with small angle approximation. The Z' axis is in line with H

and the M'_z is constant that doesn't change with time. $M'_x(t)$ and $M'_y(t)$ can be expressed by Equation 3.5 which are wave equations with damped amplitude.

$$\begin{aligned} M'_x(t) &= M'_x(0)e^{-\frac{t}{\tau}}e^{-i\omega t} \\ M'_y(t) &= M'_y(0)e^{-\frac{t}{\tau}}e^{-i\omega t} \end{aligned} \quad (3.5)$$

where $M'_x(0)$ and $M'_y(0)$ is the amplitude of the precession in X' and Y' directions at zero time, respectively. τ is the lifetime constant of the damping. ω is the angular frequency of the FMR.

The LLG equation can be decomposed into component form in $X'Y'Z'$ coordinate and $M'_x(t)$ and $M'_y(t)$ is substitute with Equation 3.5. With some mathematical transformations, τ and ω can be expressed by Equation 3.6. Equation 3.6 is called Kittel formula and is commonly used to study the ferromagnetic resonance [66][41].

$$\begin{aligned} \omega &= \gamma\sqrt{H_1H_2} \\ \frac{1}{\tau} &= \frac{1}{2}\alpha\gamma(H_1 + H_2) \end{aligned} \quad (3.6)$$

where

$$\begin{aligned} H_1 &= H_{external} \cos(\theta_H - \theta_m) + H_k^{eff} \cos^2 \theta_m \\ H_2 &= H_{external} \cos(\theta_H - \theta_m) + H_k^{eff} \cos 2\theta_m \end{aligned}$$

From the Equation 3.6 we can see the damping constant can be derived from the FMR frequency and the lifetime of the oscillation with Equation 3.7.

$$\alpha = \frac{1}{2\pi f\tau} \frac{2\sqrt{H_1H_2}}{(H_1 + H_2)} \quad (3.7)$$

In experiment, TRMOKE detects the Z component of the magnetic dynamics where f and τ can be derived. A phenomenal equation (Equation 3.8) is used to fit the TRMOKE signal[28], [67]–[71].

$$M(t) = A + Be^{-\mu t} + Ce^{-\frac{t}{\tau}} \sin(2\pi f t + \varphi) \quad (3.8)$$

where A is the offset constant, $Be^{-\mu t}$ is the exponential decay background, C is the amplitude of precession, φ is the starting phase constant. f and τ can be extracted through LSE fitting from the measured TRMOKE data. The effective damping constant can be calculated from Equation 3.9.

$$\alpha_{eff} = \frac{1}{2\pi f \tau} \quad (3.9)$$

Compared with Equation 3.8, α_{eff} should be scaled to get the Gilbert damping α . The value of the scale factor depends on the media properties and measurement conditions that will be discussed in the following sections.

3.1.3 Micromagnetic Simulation and Analysis

In this section, the micromagnetic simulation model will be presented and adopted to simulate the magnetic dynamics induced by ultrafast laser heating.

The LLG equation (Equation 1.4) should be transformed into explicit form (Equation 3.10) for simulation with numerical method [72]. Single spin was assumed in all simulation.

$$\frac{d\vec{M}}{dt} = -\frac{\gamma}{1+\alpha^2} \vec{M} \times \vec{H} - \frac{\alpha}{(1+\alpha^2)M_s} \vec{M} \times (\vec{M} \times \vec{H}) \quad (3.10)$$

Since femtosecond laser heating only disturbs the equilibrium state slightly through heating, we only include temperature dependence of two magnetic properties, $M_s(T)$ and $H_k(T)$, without considering the thermal agitation effect. T_e from two temperature model was used as the temperature to retrieve the media properties. Relationship of $M_s(T)$ and $H_k(T)$ were represented by Equation 3.11 [73].

$$\begin{aligned}
M_s(T) &= M_s(0) \left(1 - \frac{T}{T_c}\right)^\alpha \\
H_k(T) &= H_k(0) \left(\frac{M_s(T)}{M_s(0)}\right)^\beta
\end{aligned}
\tag{3.11}$$

where $M_s(0)$ and $H_k(0)$ are the saturation magnetization and anisotropy field at 0K, respectively. $\alpha = 0.33$ and $\beta = 1.1$ were used in simulation. $M_s(T)$ with $T > T_c$ was set to be zero. The room temperature (300K) saturation magnetization and anisotropy field were set to be 1500emu/cc and 30 kOe, which were close to or in between of the values measured from Co/Pt multilayers in Chapter 5. The T_c of bulk Co (1400K, [74]) was used in simulation.

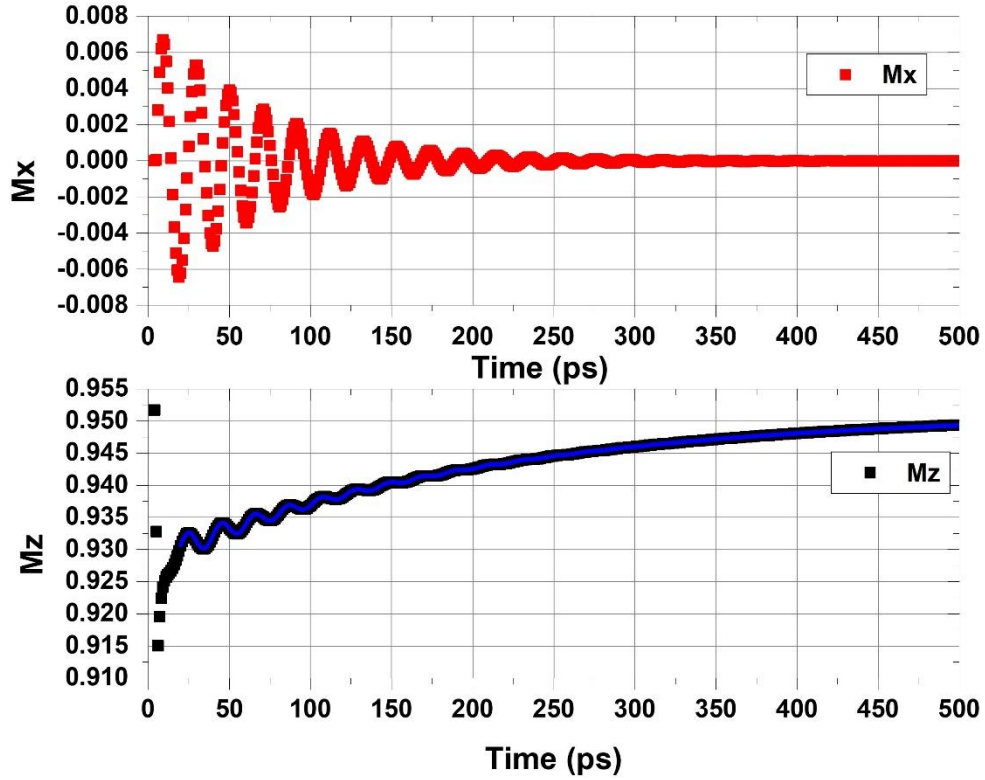


Figure 3.5 Evolution of normalized M_x and M_z components with time under femtosecond laser heating. The blue line is the fitting curve with Equation 3.8.

Figure 3.5 shows the evolution of normalized M_x and M_z components with time under femtosecond laser heating. The $H_{external}$ was set to 8.65 kOe and θ_H was set to 40° . The thermal profile in Figure 3.2 was adopted as the thermal dynamics. The damping constant α was set to 0.05 for simulation. The simulation was performed with 1×10^{-14} s step size and the result was down sampled to 1 ps step size as the output signal. As shown in the Figure 3.5, the M_x component follows a damped oscillation function as Equation 3.5. There is a fast reduction of M_z in the first few picoseconds which comes from the ultrafast heating of electrons. After the demagnetization, M_z shows a damped oscillation behavior with an exponential decay background. The blue line is the fitting curve with Equation 3.8. The 20 ps point was taken as the zero-time point to get rid of the demagnetization part for fitting.

The fitting results shows $f = 48.55$ GHz and $\tau = 66.86$ ps, which gives $\alpha_{eff} = 0.048$. The scale factor is 0.99 and can be ignored. α_{eff} is a little bit smaller than the preset α . f calculated from Kittel model (Equation 3.6) is 49.24 GHz which is 0.7 GHz larger than the fitting value from the magnetic dynamics in Z direction.

3.2 Magnetic Dynamics in Thin Films with Perpendicular Anisotropy

As shown in Section 3.1, the LLG model with thermal dynamics can simulate the magnetic dynamics induced by ultrafast laser heating. In this section, the behavior of magnetic dynamics under different experimental conditions for magnetic films with perpendicular anisotropy will be studied. The effects of pulse energy and external field will be analyzed though micromagnetic modeling.

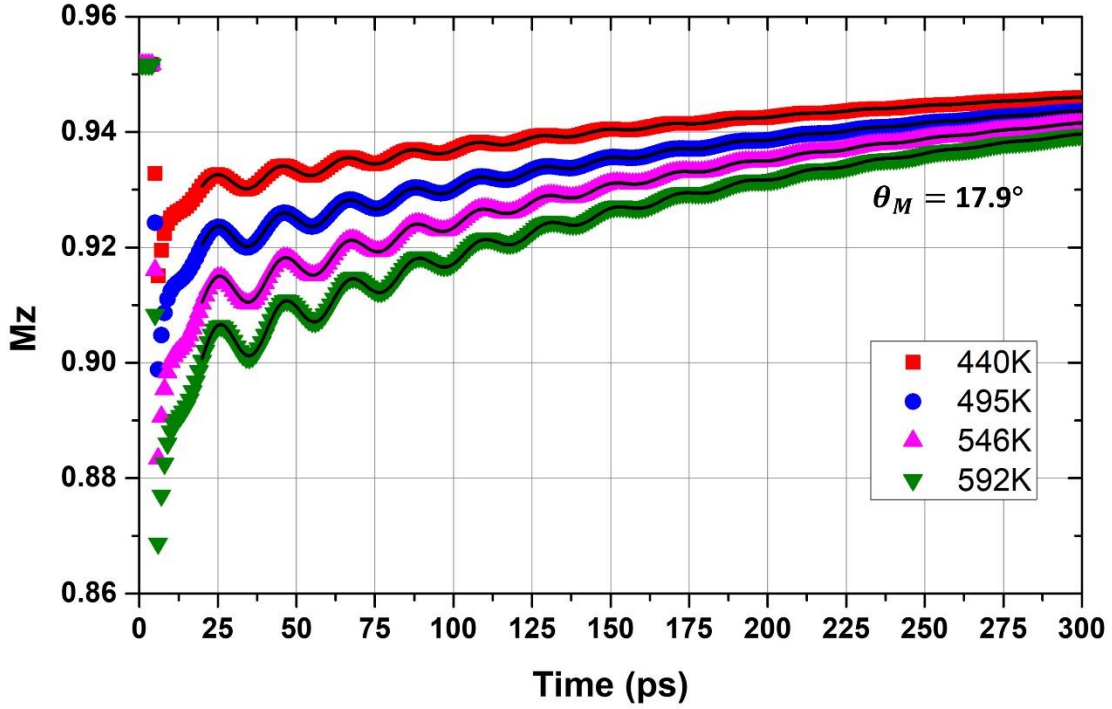


Figure 3.6 The evolution of M_z component with different pulse energy.

Figure 3.6 shows the evolution of M_z component with different pulse energy E_p . The magnitude of E_p is represented by the maximum T_e during heating. $H_{external}$ was 8.65 kOe, θ_H was 40° and H_k was 30 kOe. The black lines are the fitting curves with Equation 3.8. As shown in the figure, the demagnetization ratio and amplitude of oscillation signal are proportional to the maximum electron temperature. The fitting curves fit well with the simulation data. The magnetization direction is 17.9° w.r.t Z direction.

Figure 3.7 shows the evolution of M_z component with different θ_H . For all the simulation, $H_{external}$ is 8.65 kOe and H_k is 30 kOe. The maximum T_e is 440K. θ_H was varied from 40° to 80° in 10° step size. Again, the black lines are the fitting curves with Equation 3.8. As shown in the figure, as the $H_{external}$ moves more in-plane, the magnetic moment is tilted further away from Z direction. In the simulation data, θ_m was increased

from 17.9° to 40.5° . Since M_z equals to $M \cos \theta_m$, the amplitude of the oscillation signal also gets larger with increasing θ_m which will be easier for MOKE detection in experiment.

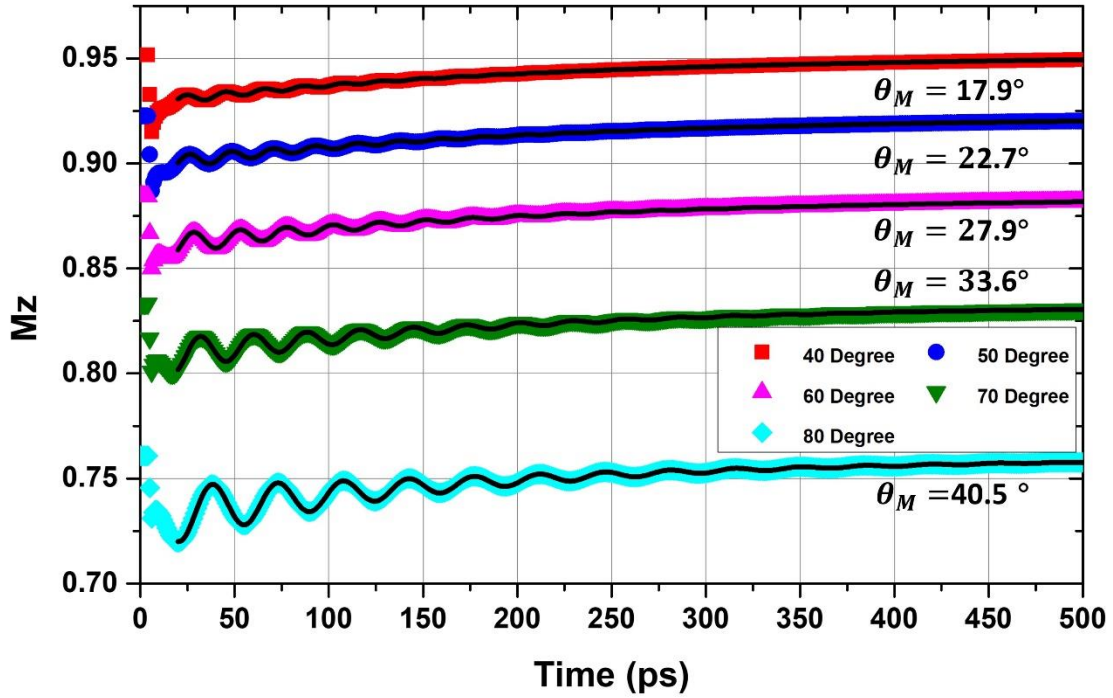


Figure 3.7 The evolution of M_z component with different external field direction.

Figure 3.8 (a) shows the fitting results of FMR frequencies with different E_p and θ_H combinations. The black line is the FMR frequencies calculated from Kittel model (Equation 3.6). As shown in the figure, the FMR frequencies from fitting are all lower than the calculated values from Kittel Model. Higher E_p will results in large deviation in f . This is a systematic difference between Kittel model and TRMOKE model. During magnetic dynamic process, θ_m is always larger than the θ_m in equilibrium state and larger θ_m corresponds to lower FMR frequency, M doesn't precess around the initial equilibrium direction as assumed in Kittel model. Thus, the frequency calculated from Kittel model will be slightly larger than the FMR frequency measured from TRMOKE. The largest

absolute deviation happens at $40^\circ \theta_H$ and 592K maximum T_e , which is 1.43 GHz, which is also the largest relative deviation 4.5%. Overall the FMR frequency is almost the same within error range.

Figure 3.8(b) shows the fitting results of precession lifetimes with different E_p and θ_H combinations. The lifetime increases with increasing θ_H which agrees with the decreasing trend in the FMR frequency. The divergence of lifetime under different E_p is smaller when θ_H is larger.

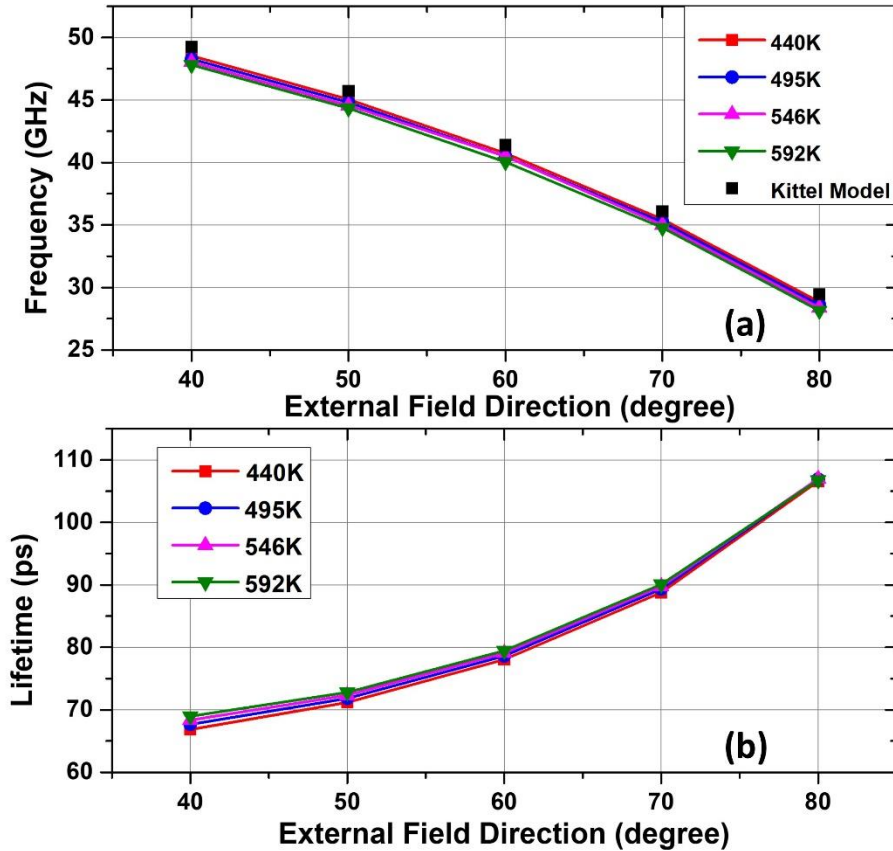


Figure 3.8 FMR frequency (a) and lifetime (b) vs. maximum electron temperature and external field direction.

Figure 3.9 shows the effective damping constant calculated from fitting f and τ with different E_p and θ_H combinations. The black line is the scale factor calculated with Equation 3.7. As shown in the figure, the scale factors almost equal to 1 with a slightly

decreasing trend as θ_H increases. Thus, for this case, the scale factor can be ignored. The relative difference between α_{eff} and α is less than 5%.

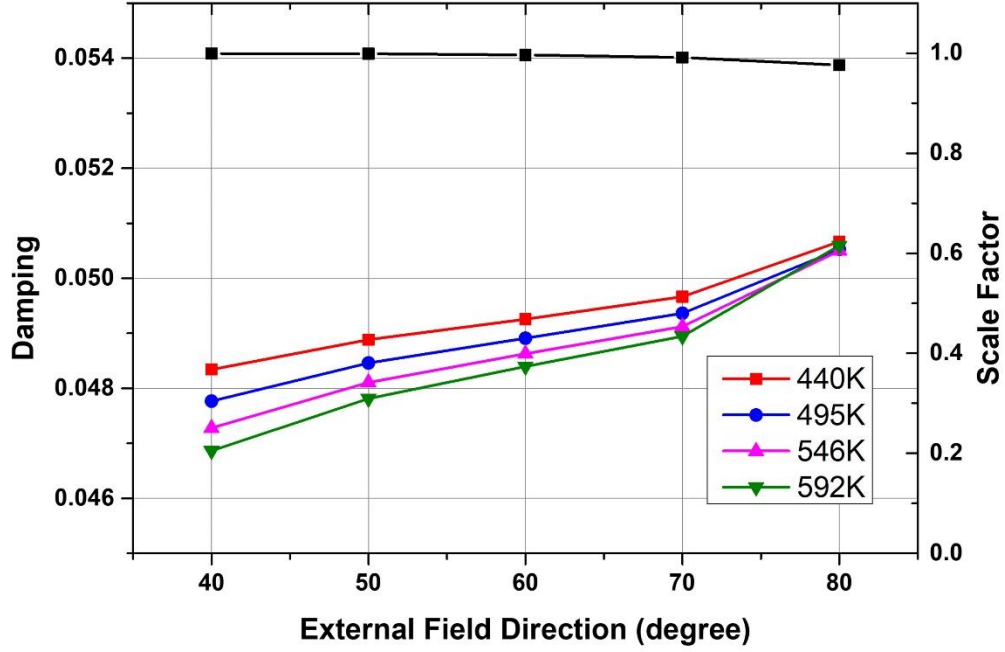


Figure 3.9 Effective damping constant vs. external field direction and maximum media temperature.

Another way to tilt the magnetic moment is fixing θ_H and changing the strength of $H_{external}$ which is also widely used in TRMOKE experiments [43], [75]. Micromagnetic simulations was also performed with θ_H fixed at 80° with different field strength and 440K maximum electron temperature.

Figure 3.10 shows the α_{eff} vs. θ_m from the two methods. In changing field strength method, the first 5 points from left to right corresponds to external field varied from 3 kOe to 7 kOe in 1 kOe step size, the last point is from the previous simulation with 8.65 kOe $H_{external}$. As shown in the figure, there are negligible difference between α_{eff} from two methods when the magnetic moment points in same direction in macroscopic perspective.

The deviations of α_{eff} from these two methods with the preset damping constant are within 5%.

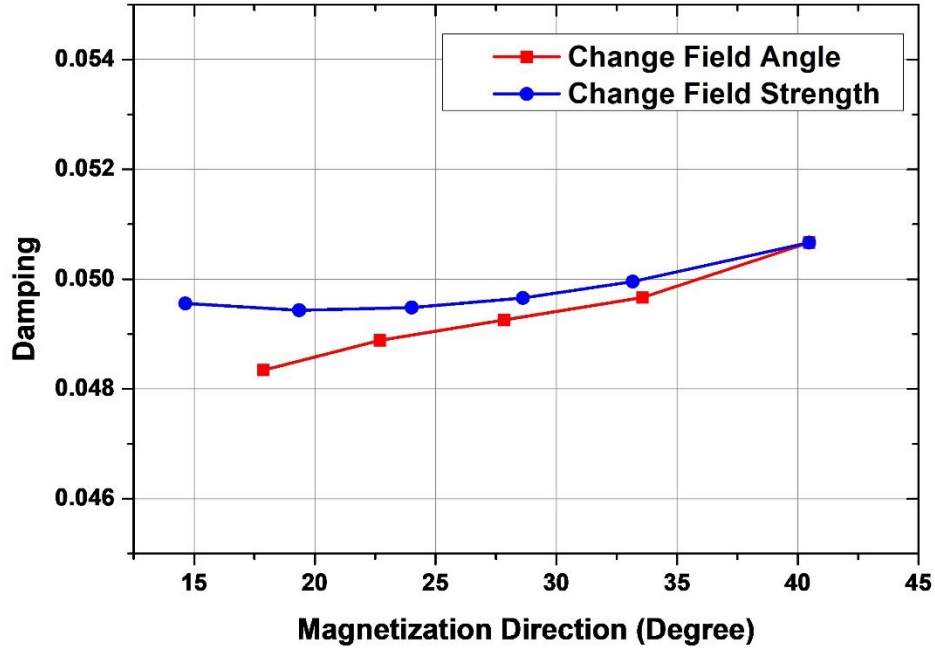


Figure 3.10 Effective damping constant vs. magnetization direction with two external field applying methods.

3.3 Magnetic Dynamics in Thin Films without Anisotropy

Magnetic films without anisotropy is also used in many applications. In this section, we will understand and simulate the magnetic dynamics in this kind of film.

The geometry of the magnetic dynamics in films without anisotropy is different from that of the films with perpendicular anisotropy. As shown in Figure 3.11, the magnetic moment lies in plane without $H_{external}$ due to the demagnetization field. When $H_{external}$ is applied at angle θ_H , the magnetic moment will be pulled out of plane to θ_m . If the film is heated by femtosecond laser, M_s will be changed instantly and cause a sudden reduction of the demagnetization field. The equilibrium direction is also changed instantly and trigger the precession of magnetic moment like the scenario in Figure 3.2, however the new

equilibrium angle will be smaller than the initial state, as shown by the yellow dashed line in Figure 3.11. The equations in Section 3.1 are also valid to analyze the magnetic dynamics with H_k set to zero.

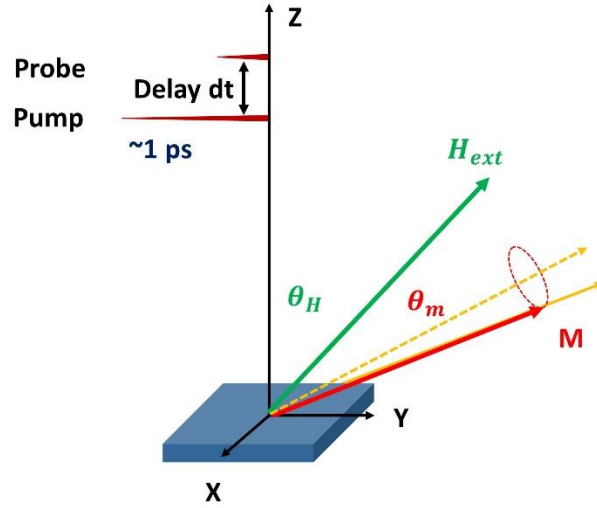


Figure 3.11 Schematic of magnetic dynamics induced by femtosecond laser in magnetic thin film without anisotropy.

Micromagnetic simulation were performed with same parameters in Section 3.2 except H_k is zero. Figure 3.12 shows the simulated magnetic dynamics in Z direction with different θ_H . The black curves are fitting result with Equation 3.8. As the shown in the figure, as $H_{external}$ becomes more perpendicular, the magnetic moment is pulled closer to perpendicular direction. The amplitude of the oscillation signal is more obvious as θ_m gets smaller, which is different from the trend in the simulation with anisotropy field (Figure 3.7). This is due to the different mechanism in the varying part in H . In the films with perpendicular anisotropy, the dominant varying part in H is H_k , the change of H_k is about the same at different θ_m with same heating temperature. Thus, the precession angle is almost the same for different θ_m . The oscillation amplitude in Z direction is determined by projecting the oscillation part with $\cos \theta_m$ to Z direction. In the film without

perpendicular anisotropy, the dominant varying part in H is the demagnetization field, which is $M_s \cos \theta_m$. Thus, the change of demagnetization field is larger with smaller θ_m . Larger demagnetization field change results in more significant oscillation signal in Z direction.

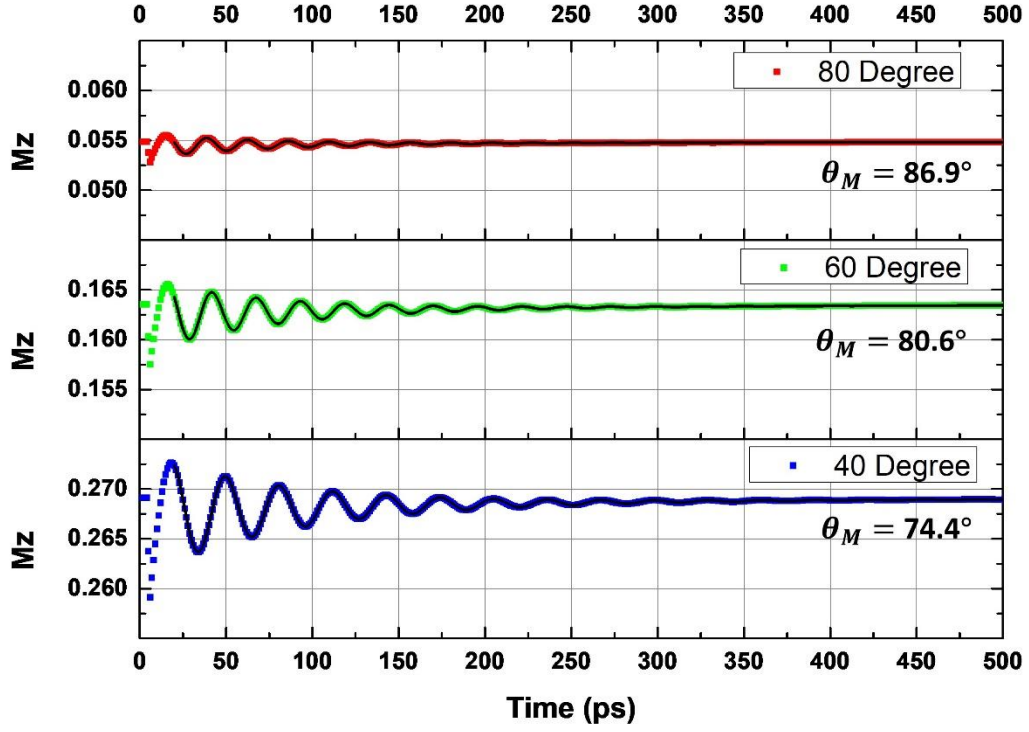


Figure 3.12 Evolution of M_z component with different external field direction.

Figure 3.13 shows the fitting FMR frequencies and lifetimes from the simulation of magnetic dynamics with different θ_H and E_p for the films without anisotropy. Figure 3.13 (a) shows the FMR frequencies from fitting are also smaller than the frequency calculated from Kittel model, but the deviation is smaller than that in the film with perpendicular anisotropy. This agrees with the observation from Figure 3.12 where the θ_m during precession can be smaller than θ_m in equilibrium state. Figure 3.13 (b) shows the lifetime decreases with increasing θ_m . High E_p slightly increases lifetime compared with low E_p .

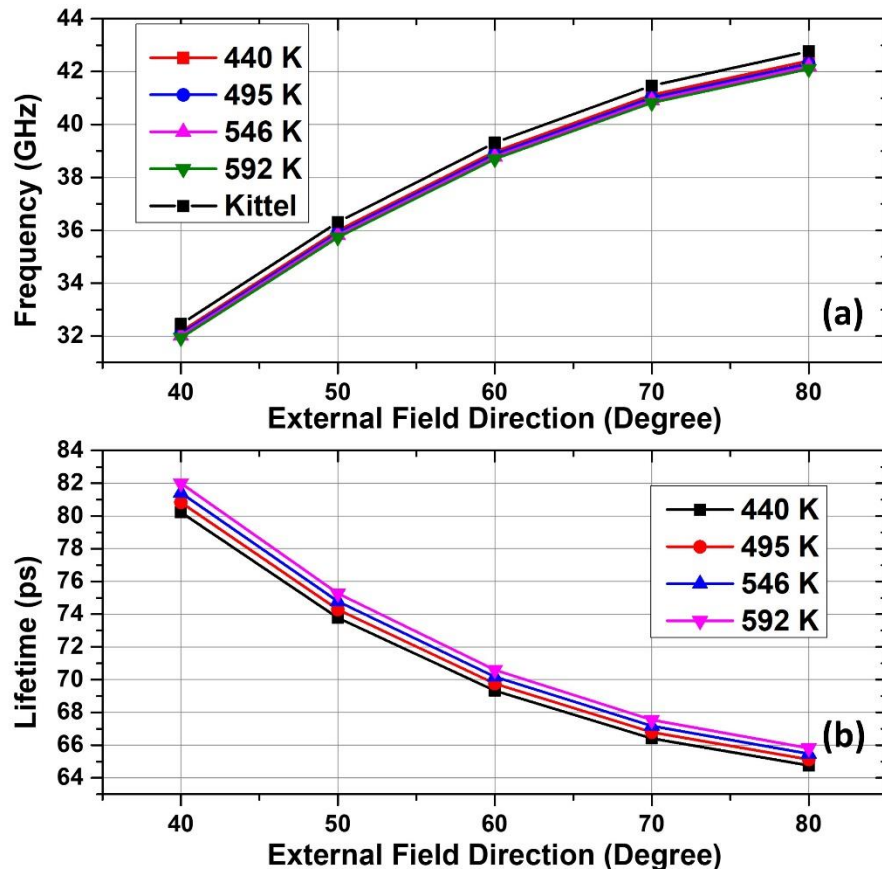


Figure 3.13 FMR frequency (a) and lifetime (b) vs. maximum media temperature and external field direction.

Figure 3.14 is the summary of scaled α_{eff} vs. θ_H . As shown in the figure, the scale factor is about 0.78 and quite different from that of the film with perpendicular anisotropy. The damping constant without scaling is larger than the preset value 0.05. The deviation can be as large as 10%. Scaled α_{eff} is slightly smaller than 0.05 with $< 5\%$ deviation. Therefore, the scale factor should be taken into consideration for the films without perpendicular anisotropy.

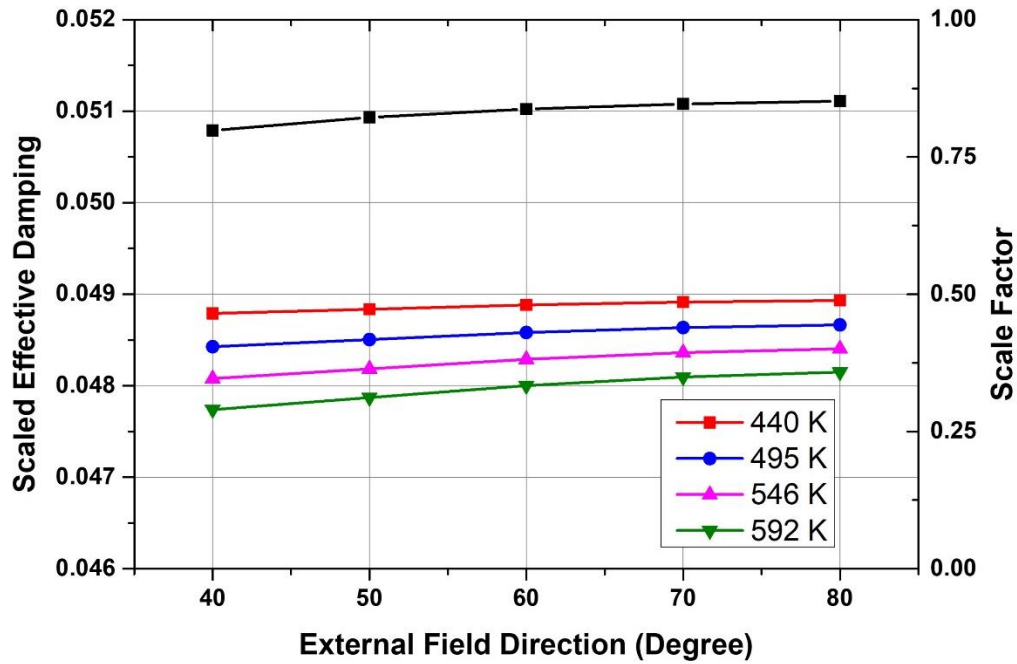


Figure 3.14 Scaled effective damping constant vs. external field direction.

In this Chapter, two temperature model was incorporated into micromagnetic simulation to study the magnetic dynamics triggered by femtosecond laser heating. The magnetic dynamic behavior is quite different for the films with and without perpendicular anisotropy. The phenomenon model fits excellent in analyzing the magnetic dynamic data. The scale factor is found to be negligible in retrieving the Gilbert damping constant for the films with perpendicular anisotropy but must be taken into consideration for the films without perpendicular anisotropy.

4 Time Resolved Magneto Optical Kerr Effect System

In this chapter, the time resolved magneto optical Kerr effect (TRMOKE) system will be designed and constructed with pump-probe technique to measure the magnetic dynamics in time domain. The details of TRMOKE system will be presented and discussed in this chapter.

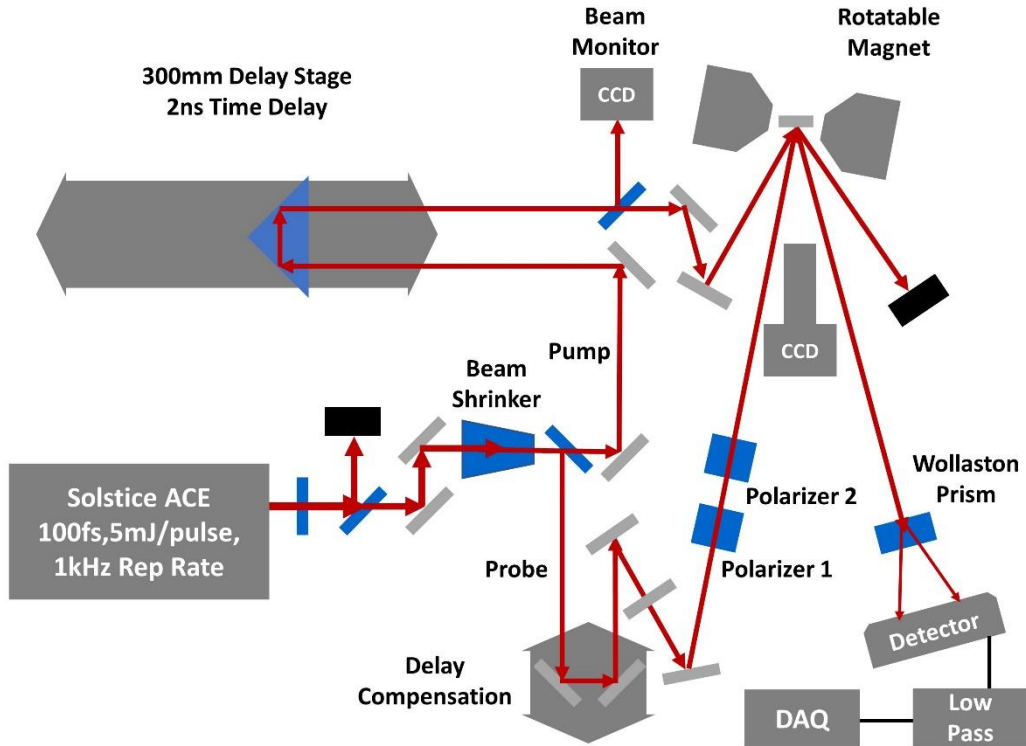


Figure 4.1 Full optical path of TRMOKE system.

Figure 4.1 shows the overview of the optical path design. A pump-probe scheme was adopted in the TRMOKE system. The laser source was ultrafast amplified Ti: sapphire laser. The output beam from the laser was attenuated and the spot size was reduced to fit the measurement requirements. Then the beam was split into two parts, one as pump beam with time delay capability, the other one as probe beam for MOKE measurement. The

whole system was controlled by LabVIEW programs. The details of the system design and capability will be discussed in the following sections.

4.1 Ultrafast Amplified Femtosecond Ti : Sapphire Laser

The laser source was Solstice ACE laser from Spectra Physics. It was an amplified Ti:sapphire laser with 1 kHz repetition rate, < 100 fs pulse width, ~ 800 nm center wavelength. The output pulse energy was 5mJ/pulse. The diameter of the laser spot was about 10 mm ($1/e^2$) with TEM00 spatial mode. The polarization direction of the output beam was in horizontal direction. The laser was able to maintain 0.5% power stability over 24 hours with the advanced design from Spectra Physics. The low 1 kHz repetition rate can ensure the sample was able to cool down to room temperature after the excitation. However, the pulse energy was more than enough to pump and probe the magnetic dynamics, the pulse energy was first reduced with a pulse energy control subsystem. The spot size was also too large to fit into many optical components. A spot size control system was introduced after the pulse energy control system.

The pulse energy control was achieved by manipulating the polarization of the laser. Figure 4.2 shows the optical path and the principle to control the pulse energy. The system contained a zero-order air-spaced half waveplate mounted on a continuous rotation mount and a thin film polarizer. Both were from EKSMO Optics and specially designed for 800 nm high power ultrashort laser pulses. The half waveplate was made from single crystal quartz, which has different indices of refraction for lights polarized in different orientations. In waveplate products, fast axis is often labeled to indicate the polarization direction along which the light has a lower index of refraction. The light polarized in fast axis direction travels faster through waveplate than the light polarized along the slow axis, which is

perpendicular to the fast axis. Half waveplate were commonly used to rotate the polarization direction of linearly polarized light. As shown in Figure 4.2, the fast axis of the waveplate lies in XY plane and was rotated by an angle θ w.r.t. the YZ plane. The P-polarized light from the laser can be decomposed into two components in the X'Y'Z' coordinate of the waveplate as shown in Figure 4.3.

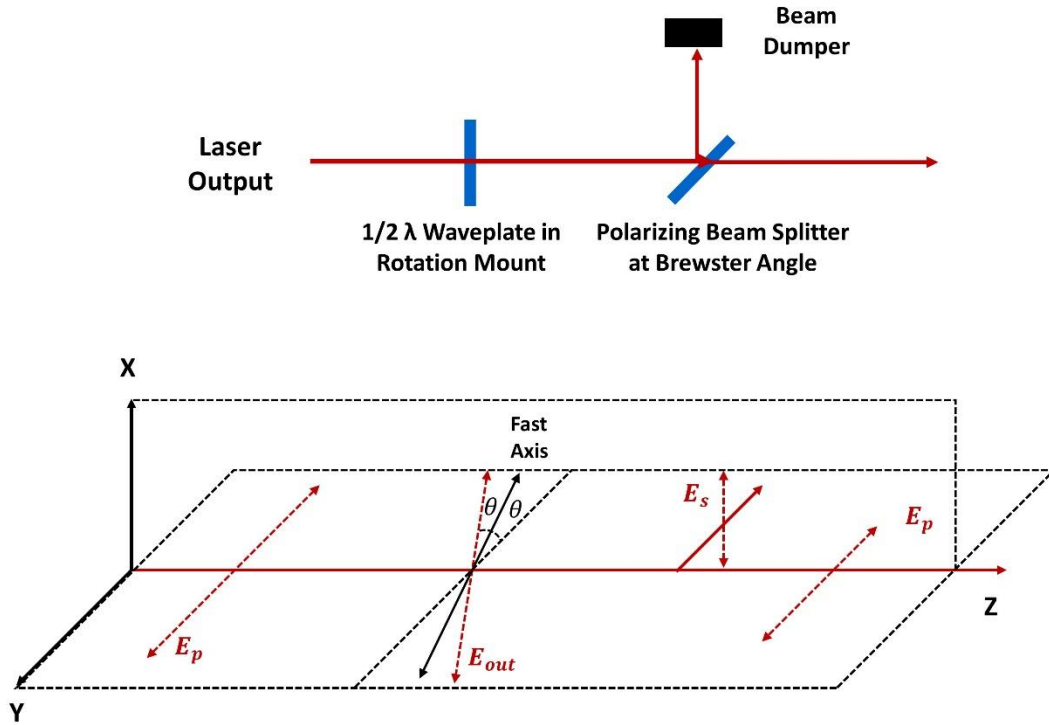


Figure 4.2 Optical path and principle for pulse energy control.

$$\vec{E} = E \sin \theta \sin(kz + \omega t) \hat{X}' - E \cos \theta \sin(kz + \omega t) \hat{Y}' \quad (4.1)$$

where \vec{E} is the vector of electric field of the input light. E is the amplitude of the electrical field. \hat{X}' and \hat{Y}' are the unit vectors in X' and Y' directions, respectively. k is the wave vector of the light. Since the light polarized in the slow axis direction travels slower, the transmitted light will encounter a φ phase delay after passing through the half waveplate, which changes the polarization of output light into the form of Equation 4.2

$$\vec{E} = E \sin \theta \sin(kz + \omega t) \hat{X}' - E \cos \theta \sin(kz + \omega t + \varphi) \hat{Y}' \quad (4.2)$$

For half wave plate φ equals $\frac{\pi}{2}$, the polarization of output light will be Equation 4.3

$$\vec{E} = E \sin \theta \sin(kz + \omega t) \hat{X}' + E \cos \theta \sin(kz + \omega t) \hat{Y}' \quad (4.3)$$

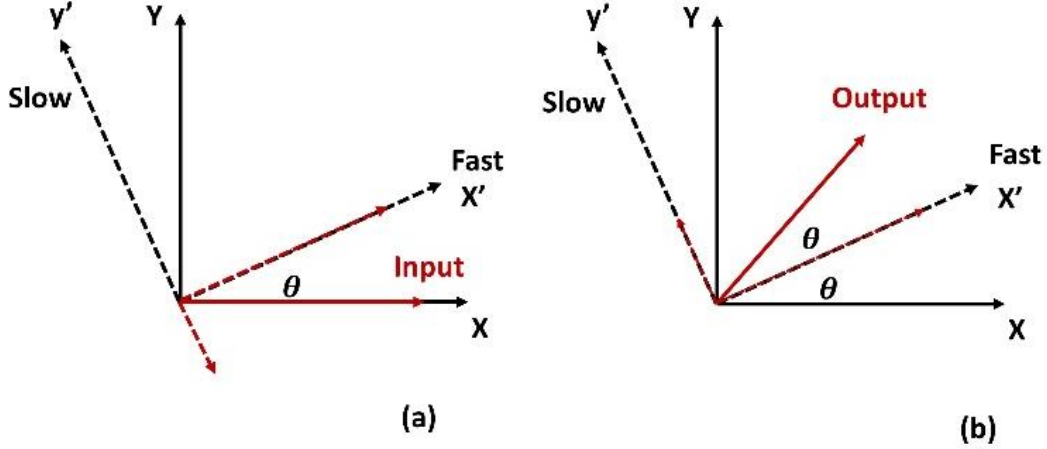


Figure 4.3 Polarization state of light before and after half waveplate.

The polarization directions before and after the waveplate viewed in Z direction are shown in Figure 4.3. The polarization of input light will be rotated by 2θ w.r.t. the YZ plane after passing through half waveplate, thus the ratio of S-polarized light and P-polarized light was changed. A thin film polarizer was used to reflect S-polarized light into the beam dumper and transmitted P-polarized light. The output pulse energy can be controlled by changing θ according to Equation 4.4. For TRMOKE application, the pulse energy was reduced to $300 \mu\text{J/pulse}$.

$$P = P \cos^2 2\theta \quad (4.4)$$

The spot size control subsystem was designed with a commercial beam expander to reduce the spot size. The GBE03-B beam expander from Thorlabs was used in reverse direction as a beam shrinker. As shown in Figure 4.4, the beam expander contains a convex lens and a concave lens working in Galilean configuration. The convex lens focuses the input beam

to reduce the beam diameter, then the concave lens collimates the output beam. This beam shrinker can reduce the output spot size to $1/3$ of the input spot size. The beam shrinker was mounted in optical cage system and sandwiched between two irises (I1 and I2) for easy alignment. The laser beam was first aligned without beam expander mounted in the cage system. Mirror 1 (M1) and mirror 2 (M2) were mounted on adjustable mirror mounts to direct the beam passing through the center of the cage system with the help of the irises and an energy meter. The energy meter was placed at the exit port of the cage system. The adjustment contained two operations:

(1) M1 was adjusted to maximize the energy reading with I1 opened about half of the spot size and I2 fully opened, which ensured the beam enters through the center of I1 .

(2) Then M2 was adjusted to maximize the power reading with I1 fully opened and I2 half opened, which ensures the beam exits through the center of iris 2.

These two operations were repeated several times until no adjustment was necessary, i.e. the beam was aligned coaxial with the cage system. The various form of this two-mirror technology was also used in other parts to ensure the beam propagating along a specific direction.

After alignment, the beam expander was mounted into the case system. The output beam was roughly collimated by monitoring the spot size with a white card moving back and forth. Fine adjustment was later made with a beam monitoring CCD camera integrated with pump line. The output beam must be well collimated to make sure the spot size doesn't change when the length of optical path is changed.

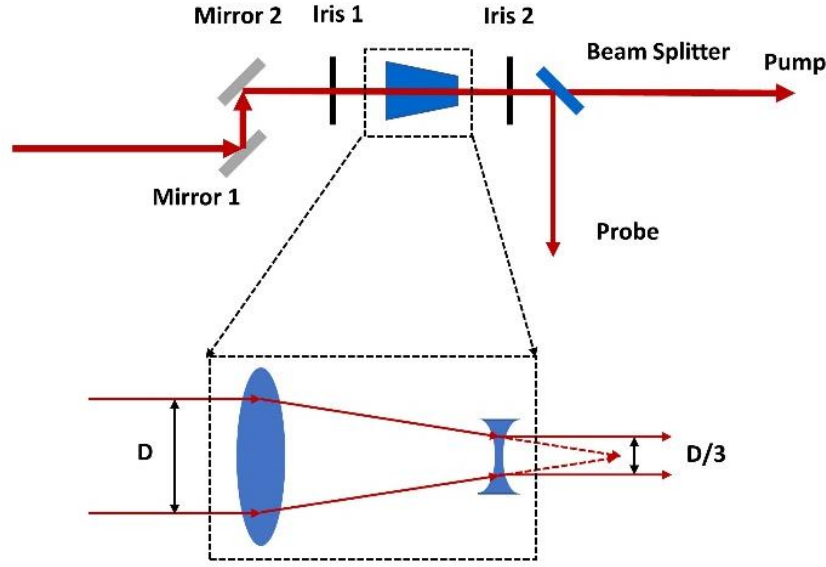


Figure 4.4 Beam spot size control system.

The output beam from the beam shrinker was split into two parts by a 50:50 non-polarizing plate beam splitter. The transmitted light was directed to the automatic translation stage as pump beam. The reflected light was used as probe beam.

4.2 Pump Line for the Excitation of Magnetic Dynamics

The pump line was designed to change the time delay between pump pulse and probe pulse with a motorized translation stage. The pump light is retroreflected back by the retroreflector mounted on the translation stage. Thus, the time delay can be achieved by changing the travel distance of the pump pulse with the motorized translation stage moving back and forth. Since the wobbling of laser spot was inevitable during the movement of the translation stage, integrating the translation stage in pump line ensured no moving part in probe line for accurate MOKE measurement. 150 μm spatial step size corresponds to 1 ps delay in time domain.

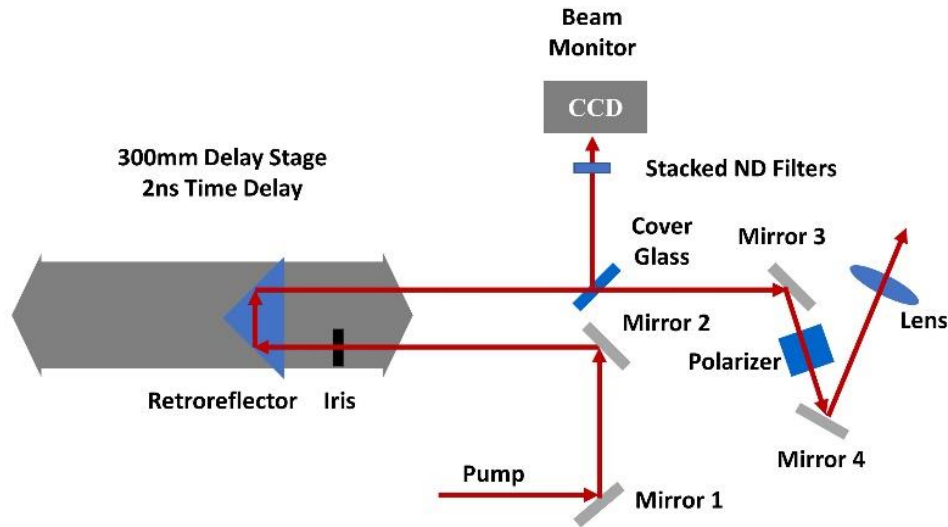


Figure 4.5 Optical path of pump line.

Figure 4.5 shows the details of the pump line. To achieve accurate time delay and minimize pump spot drifting, the beam must be accurately aligned to the travel direction of the translation stage and retro-reflected back. Two-mirror configuration was used for the alignment. The laser beam was turned with two mirrors, M1 and M2. An iris was mounted on the translation stage to indicate the travel direction of the translation stage. The open diameter of the iris is about half of the spot size. The energy meter was placed behind the iris to monitor the pulse energy passing through the iris. The iterative adjustment of alignment contains two operations:

- (1) The iris was brought close to M2, the energy reading was maximized by adjusting M1.
- (2) The iris was moved away from M2, the energy reading was maximized by adjusting M2.

This procedure was repeated several times until no adjustment was necessary. The retro-reflection of the beam was achieved with the hollow retroreflector from Newport. The

retroreflector was constructed of three front-surface mirrors assembled into a corner cube with 1 arc second return beam parallelism. If the beam travels 1 m after the retroreflector, the spot center drifting due to the fabrication error of retroreflector is only about 5 μm . The retroreflector was mounted behind the iris on a vertical translation stage that can be used to adjust the height of reflected light to be the same as the height of input beam. The total travel range of the stage is 300 mm, which corresponds to 2 ns delay in time domain.

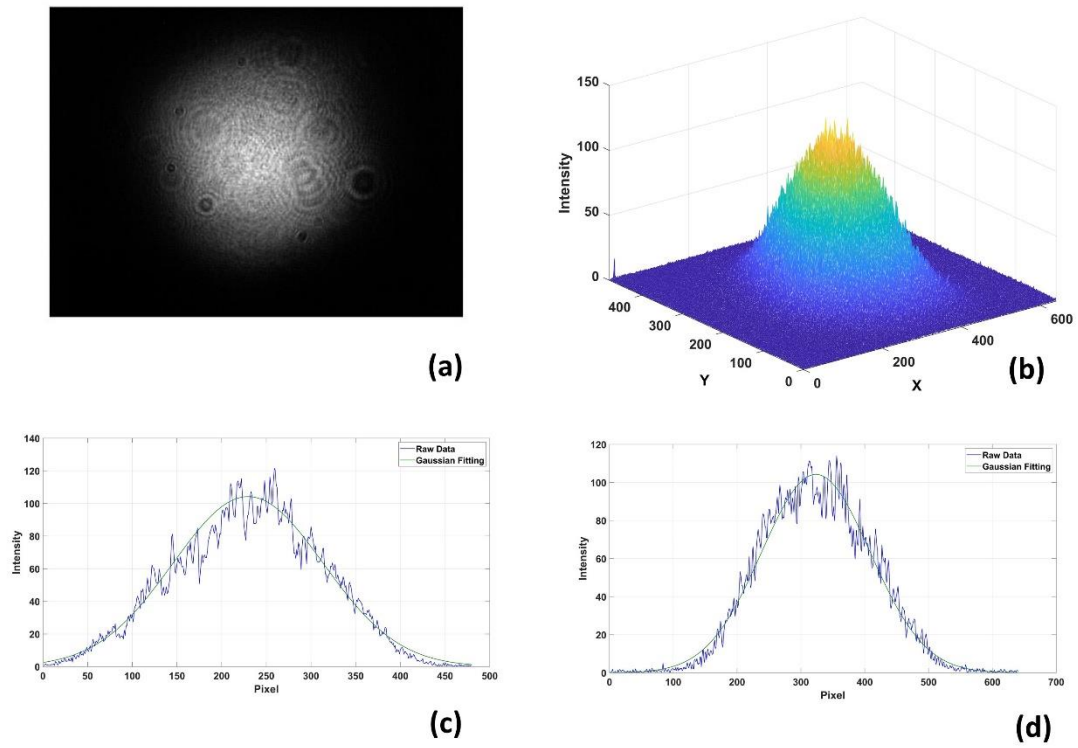


Figure 4.6 Spot size analysis with CCD camera. (a) The intensity image of laser spot; (b) 3D plot of laser intensity; (c) Intensity plot along X axis; (d) Intensity plot along Y axis. (c) (d) are the cross section at spot center.

To inspect the quality of beam collimation and alignment, a CCD camera was used to capture the spot image to perform analysis. Part of the retro-reflected beam was sampled with a cover glass and directed into the camera. A stack of neutral density filters was mounted before the camera to avoid the saturation of the CCD sensor. The intensity images of the CCD camera were captured by a video card for analysis. The spot size was extracted by fitting the intensity data with 2D Gaussian function. For spot drifting monitor, the spot center was calculated from the weighted average of the coordinate with the intensity as weight.

Figure 4.6 (a) shows an example of captured intensity image. (b) is the 3D plot of image intensity, which shows a near Gaussian distribution. (c) is the intensity plotted along the X direction with Y centered at the fitting center. (d) is the intensity plotted along the Y direction with X centered at the fitting center. The blue lines are the raw data and the green lines are fitting curves to Gaussian function. The position unit is in pixel.

The beam collimation should be adjusted first since the adjustment of beam shrinker might change the direction of output beam. The collimation was fine adjusted according to the spot size with the retroreflector moved back and forth. The spot size with retroreflector at far end was adjusted to match the spot size at close end by rotating the lens in the beam shrinker. After several repetitions, the final spot size at far end was 711 μm (x axis) and 815 μm (y axis), the spot size at close end was 716 μm (x axis) and 825 μm (y axis). The absolute values were calculated from number of pixels multiplied by the distance between pixels. The deviation of spot size during the movement of retroreflector is about 1%.

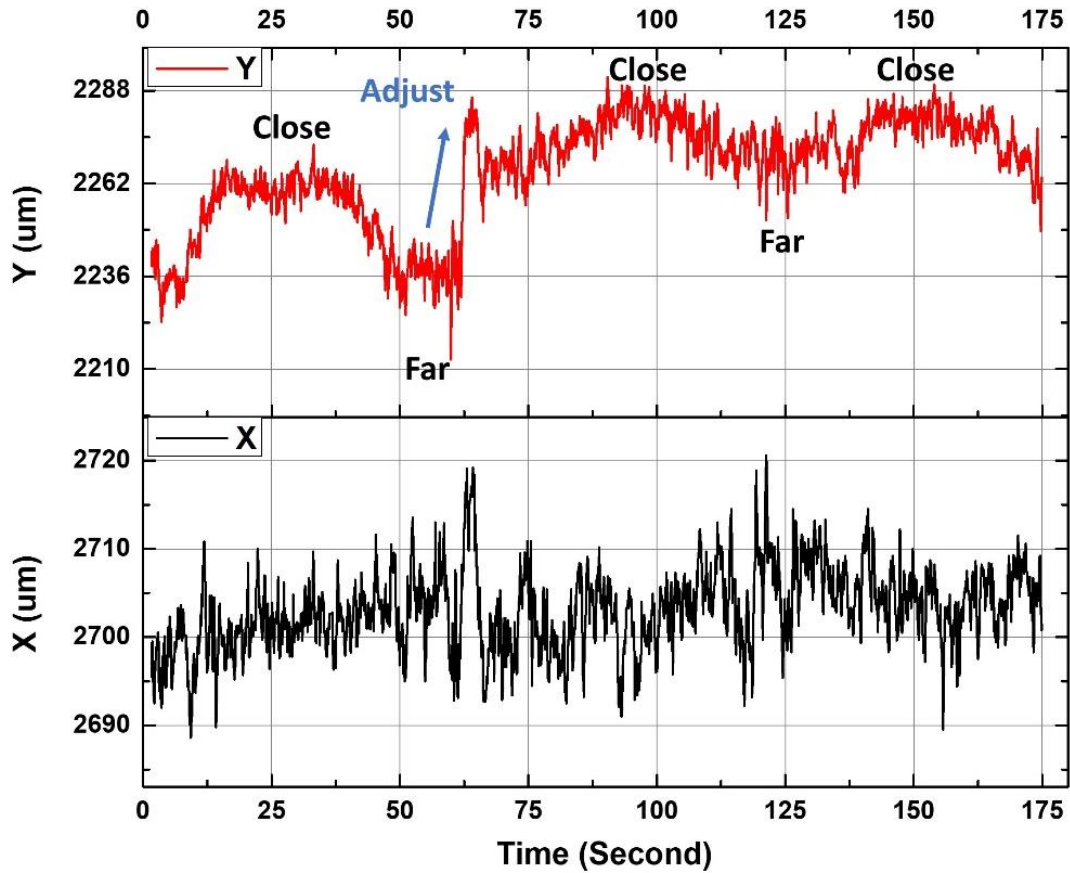


Figure 4.7 Spot center drifting and adjustment.

After collimation adjustment, the input beam into the retroreflector was fine adjusted by tuning M2, the spot center with retroreflector at far end was brought closer to the spot center with retroreflector at close end. Figure 4.7 shows the drifting of the spot center in X and Y directions during the movement of translation stage. The translation stage was first moved from close end to the far end, the Y drifting was about $30\text{ }\mu\text{m}$ in negative direction and the X drifting was negligible. M2 was adjusted to move the spot in Y direction. Then the stage was moved back and forth to check the spot center drifting which was about $20\text{ }\mu\text{m}$ after adjustment. The principle of collimation and alignment adjustments is using the state at close end as reference point that changes less significantly than that at far end.

After fine adjustment of collimation and beam pointing, the pump beam was directed through another polarizer mounted in a continuous rotation mount to control the final pulse energy for different excitation requirements. The lowest pump energy was 1 $\mu\text{J}/\text{pulse}$. The pump beam was focused on the sample holder by a convex lens and the spot diameter was about 2 mm. The incident angle of pump beam was about 15° .

4.3 Probe Line for the Detection of Magnetic Dynamics

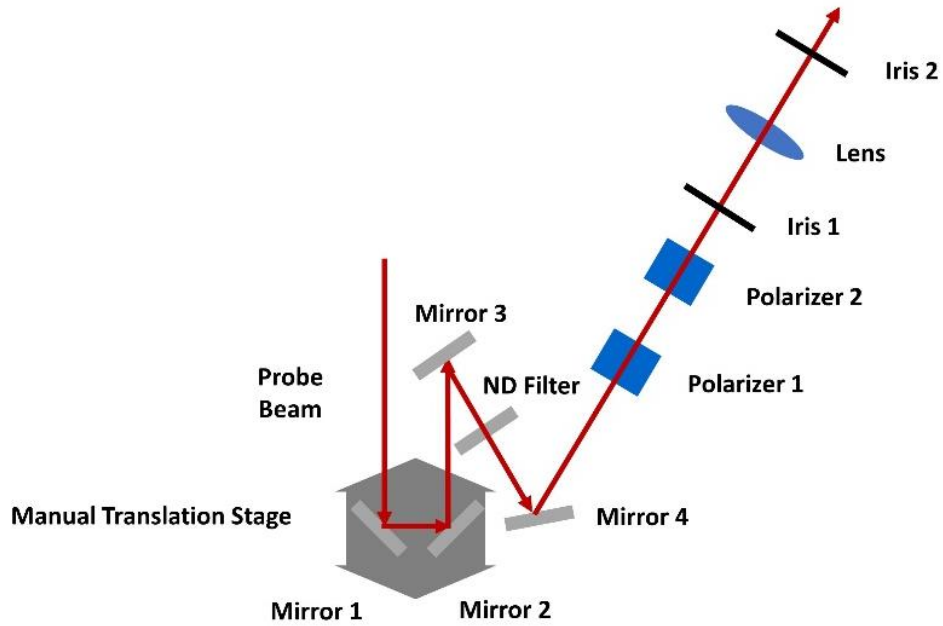


Figure 4.8 Optical path of incident probe beam.

The reflected light from the non-polarizing beam splitter in Section 4.1 was used as probe beam. Figure 4.8 shows the optical path for the incident probe beam of MOKE. The pump-probe scheme requires a zero-time delay point between the pump pulse and probe pulse during the travel of the motorized delay stage. A manual translation stage was added to compensate the travel distance of probe pulse. The probe beam was retroreflected by two mirrors mounted on a manual translation stage. The alignment was only done roughly with an alignment target. Then the pump beam was folded by another two-mirror turning

system (M3 and M4) on the sample holder as the incident light for MOKE measurement. The incident angle was about 8° . After overlapping the pump beam and probe beam, a 1GHz fast photodetector (818-BB-21 from Newport) was placed at the overlapping position to further adjust the compensation stage. The output of the photodetector was monitored on an oscilloscope. The compensation stage was adjusted so that during the motion of motorized delay stage, the pump pulse can move from negative time delay position (pump pulse arrives later than probe pulse) to positive time delay position (pump pulse arrives earlier than probe pulse).

After delay adjustment, two Glan-Laser polarizers (GL-10 from Newport) mounted on continuous rotation mounts were added to adjust the polarization direction and the intensity of probe beam. P2 was used to control the polarizing direction of incident light. The incident light contained half S-polarizing and half P-polarizing components. P1 was used to control the intensity of incident light. A long focal length convex lens was added to focus the probe beam on the sample. A telescope with CCD camera was used to inspect the overlapping of pump spot and probe spot. If necessary, the last turning mirror of pump beam was adjusted to overlap the pump spot with probe spot. The ratio of pump spot size and probe spot size was about 4, which ensures the probed region was excited uniformly.

The reflected probe light was focused by a convex lens and passed through a Wollaston prism to separate the S and P components into two directions as shown in Figure 4.9. The two beams were detected separately by two photo detectors of a balanced photoreceiver (Newport 2307). The balanced photoreceiver amplified the intensity difference of S and P light. The output from the photoreceiver were passed through a low pass filter with 2kHz cutoff frequency to remove the high frequency components. Then the filtered signal was

sent into a SR830 lock-in amplifier that locked to the trigger signal of the laser which was 1 kHz. The amplitude of the 1 kHz signal was taken as the MOKE signal. During testing, the photoreceiver was well shielded from the environmental light and diffracted laser light to reduce the noise. The time constant of SR830 was set to 300 ms and long-term monitoring shows the standard deviation of MOKE signal is smaller than 0.1%.

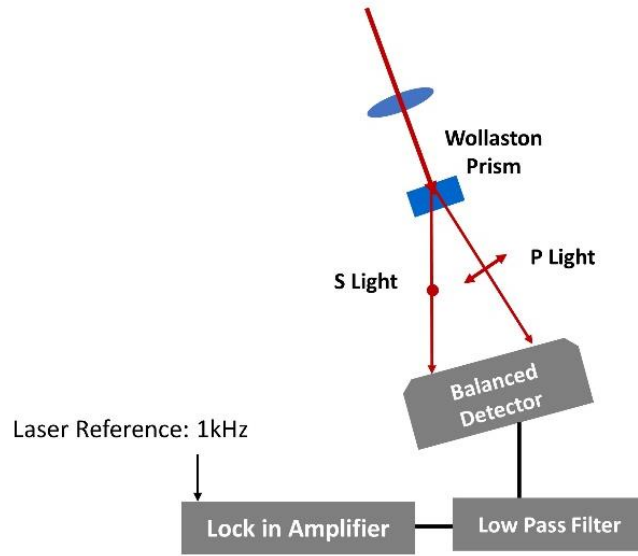


Figure 4.9 Optical path for MOKE detection.

4.4 Compact Electromagnet and Sample Holder

As stated in Chapter 3, to measure the change of MOKE signal in Z direction, an external field must be applied to deviate the magnetic moment away from Z direction at some angle w.r.t to film normal.

A water-cooled compact electromagnet was designed and constructed to satisfy the requirements. The core of the electromagnet was made of soft iron. The poles were 1 inch high cone with 1 inch top diameter and 3 inches bottom diameter. The distance between poles were 0.375 inches. A 0.4 inch high slot was opened on one pole for the access of

pump beam and probe beam. The coil was home wound with magnet wire, 3 copper tubes were embedded into the coil to flow cooling water for high current operation. The whole electromagnet was mounted on a XY translation stage and a rotation stage for adjustment of position and the external field direction. The direction of magnetic field can be varied from 0° to 90° with respect to the film normal.

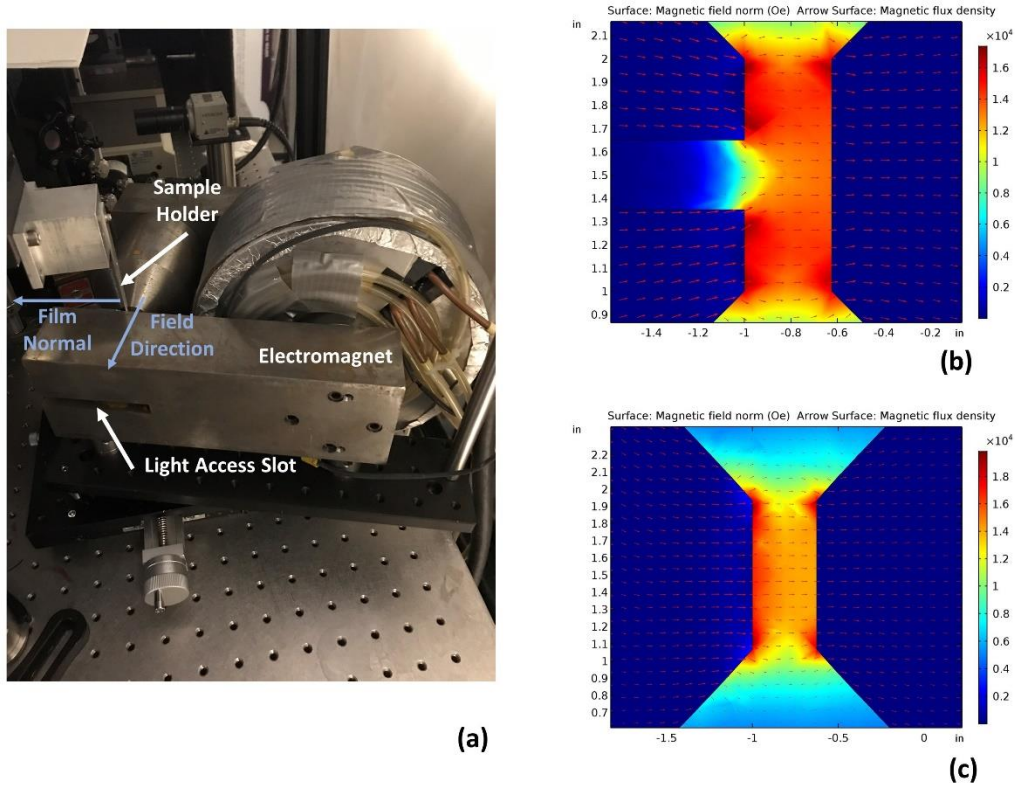


Figure 4.10 Photo and the simulation of magnetic field for homemade electromagnet.

Figure 4.10 (a) shows the photo of the electromagnet. The magnetic field distribution was simulated with COMSOL Multiphysics. Figure 4.10 (b) and (c) shows the simulated magnetic field on XZ and XY planes cut at the center between poles, respectively. The nonuniformity of the magnetic fields in sample region was $< 1\%$. The magnetic field was calibrated by placing the Hall sensor of the Gauss meter at the position of the laser spots. The maximum continuous field was 8.65 kOe at 25 A current with water cooling. The

resistance change is about 15% which is comparable to commercial electromagnet. The magnetic thin films were cut into 1/4 inch by 1/2 inch chip and mounted on the sample holder with double side tape. The sample holder was mounted on a XYZ translation stage for adjustments.

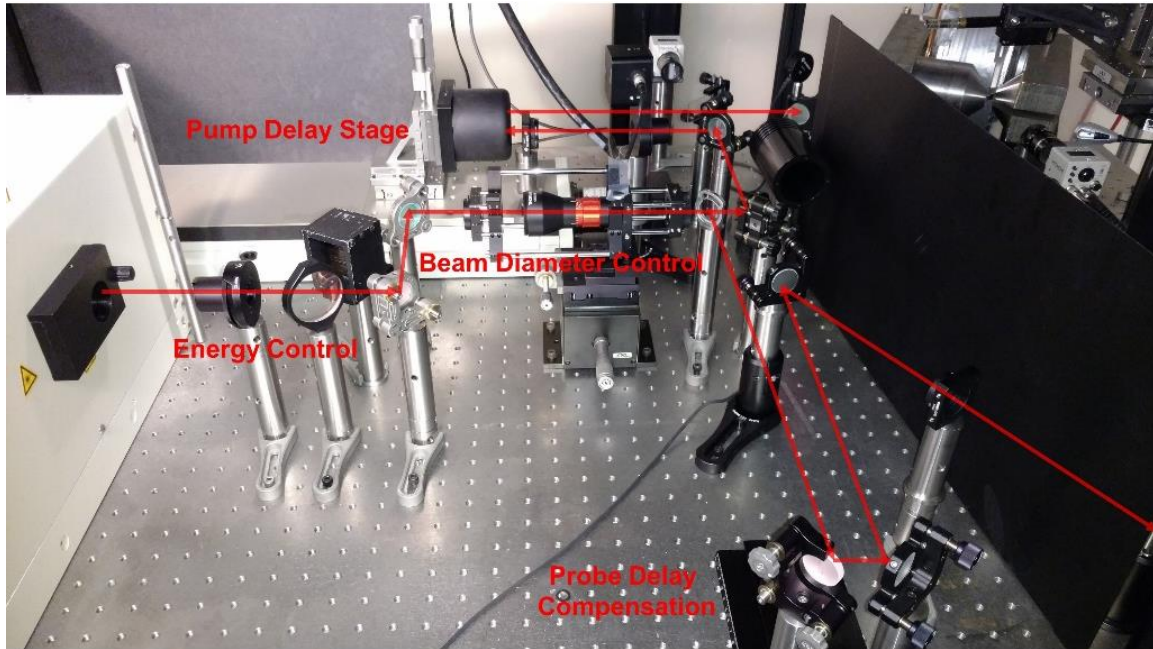


Figure 4.11 TRMOKE delay control.

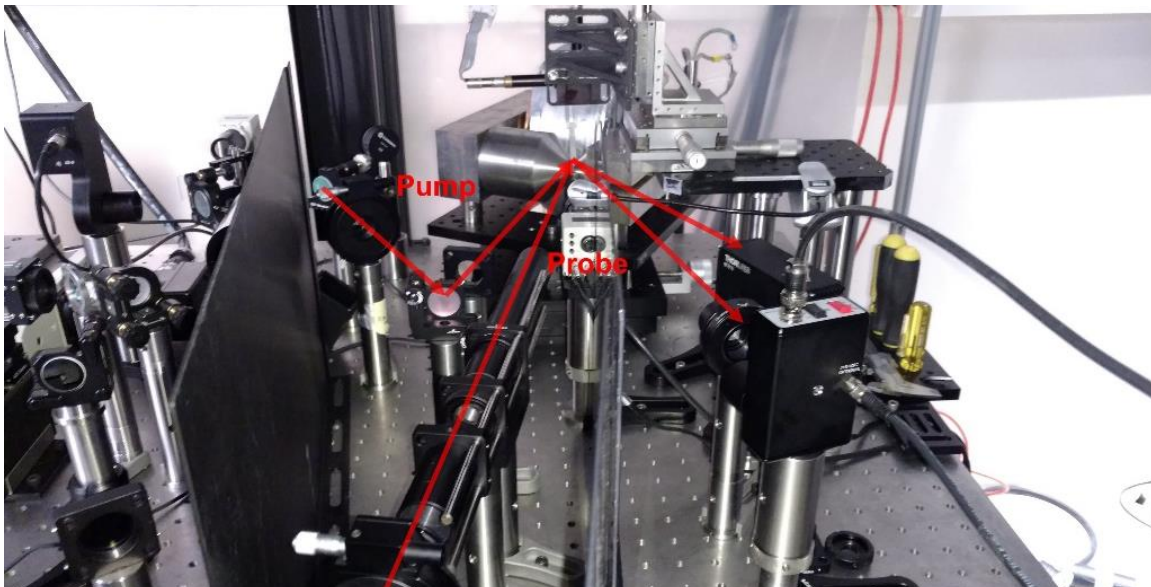


Figure 4.12 TRMOKE detection.

Figure 4.11 and Figure 4.12 are the overview of the TRMOKE systems with the key components labeled. All components will be covered to block the diffused light from entering the detector.

In this Chapter, the concerns and operations of the TRMOKE system were discussed in detail. The TRMOKE system has the following key capabilities:

- (1) ~ 800 nm center wavelength, ~ 100 fs pulses width, 1 kHz repetition rate
- (2) 3 ns time delay with 200 fs resolution.
- (3) ~ 1% beam diameter variation (3ns delay).
- (4) ~ 1% (center drift/beam diameter) beam pointing stability (3ns delay).
- (5) < 0.1 % noise in long term (1 hour) MOKE signal.
- (6) 8.65 kOe magnetic field with 0° to 90° field angle adjustment.

5 TRMOKE Study of the Gilbert Damping in Multilayered Magnetic Thin Films

5.1 Study of TRMOKE Experimental Conditions

TRMOKE measurement can be performed in many different experimental conditions, three key factors are pulse energy, external field strength and external field direction. The measured effective damping constant including the intrinsic and extrinsic contributions varies significantly with different media properties and experimental conditions.

Bo Liu, et.al studied the dependence of intrinsic damping constant α (measured with high field) on pump influence with in-plane and perpendicular CoFeB films. The pump influence was varied from 5 mJ/cm² to 12 mJ/cm² in both studies. The α of in-plane film increases from ~ 0.006 to ~ 0.013 with increasing pump influence while the α of perpendicular films remains constant at 0.0165 [70], [76]. The increasing of α was explained as the transient enhancement of electron temperature during pumping and the temperature dependence of damping [76]. However, the study of in-plane FePt by Zhifeng Chen et.al shows different trend. They reported α_{eff} decreased from 0.066 to 0.038 with the fluence increased from 2.5 to 7.3 mJ/cm² [77]. This phenomenon was explained as the magnetic inhomogeneity was reduced at a higher temperature induced by stronger pump fluence [77].

For the experiments performed with varying external field strength, Bo Liu, et.al studied CoFeB films with in-plane and perpendicular anisotropy with external field angle θ_H fixed at 60° and 47.5°, respectively. In both studies, they reported the effective damping constant α_{eff} decreases sharply with increasing field strength and saturates to constant at high fields

[70], [76]. Similar effect was found in $[\text{Co/Ni}]_N$ multilayer system studied by Hyon-Seok Song et.al with θ_H fixed at 60° . For $N=24$, α_{eff} decreases with increasing external field and saturates at high fields. However, for $N=6$, α_{eff} measured with different field strengths are almost constant [71]. Thus, high external field strength is usually applied to suppress the extrinsic damping that may come from spin-wave and magnetic inhomogeneity [70], [71], [76]–[79].

As for θ_H dependence, S. Mizukami et.al reported α_{eff} increased from 0.055 to 0.10 with θ_H increased from 30° to 80° for L_{10} FePt films [80]. For $[\text{Ni/Co}]_N$ multilayer films, the α_{eff} is independent of θ_H and field strength except for $t_{Co} = 0.3$ nm, $t_{Ni}=0.6$ nm and $N=2$ at $\theta_H=80^\circ$ [69]. In this section, we will study the best experimental conditions for the TRMOKE measurement of Co/Pt multilayers with different pump influence and external field configurations. The experimental conditions to acquire intrinsic Gilbert damping in Co/Pt multilayers will be studied.

5.1.1 Co/Pt Fabrication and Static MOKE Measurement

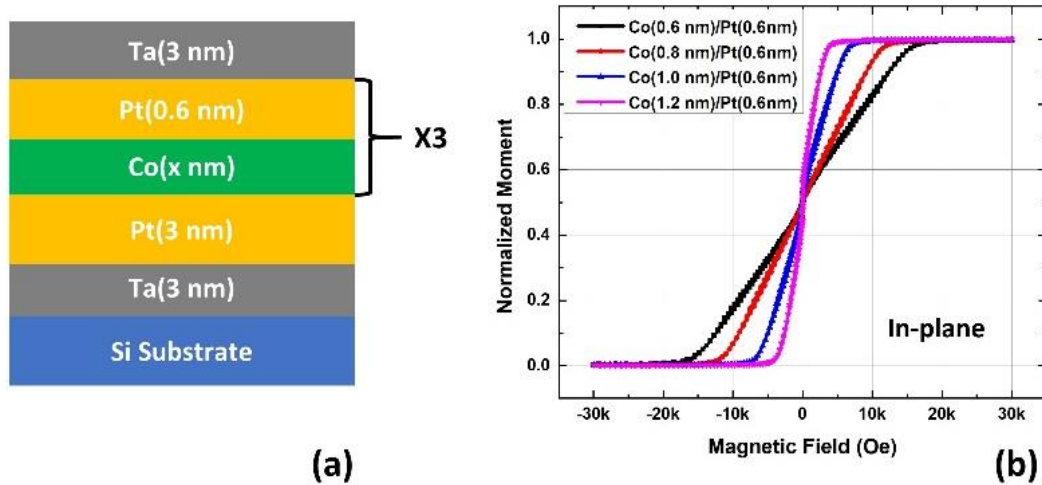


Figure 5.1 Film stack and in-plane MH loops of Co/Pt multilayered magnetic thin films.

The Co/Pt multilayered thin films were prepared by magnetron sputtering on thermally grown SiO₂ substrate with base pressure less than 1×10^{-8} Torr. The film stack from bottom to top was Ta (3 nm)/Pt (3 nm) [Co (X nm)/Pt (0.6 nm)]₃/Ta (2 nm). The Co layers thickness was varied from 0.6 nm to 1.2 nm in 0.2 nm step size. The magnetic properties were characterized by Quantum Design's Magnetic Property Measurement System (MPMS-3). Figure 5.1 shows the film structure and the normalized in-plane magnetic hysteresis loop. The in-plane MH loops shows in-plane hard axis which corresponds to out-of-plane easy axis. The effective anisotropy field H_k^{eff} increases with decreasing cobalt layer thickness.

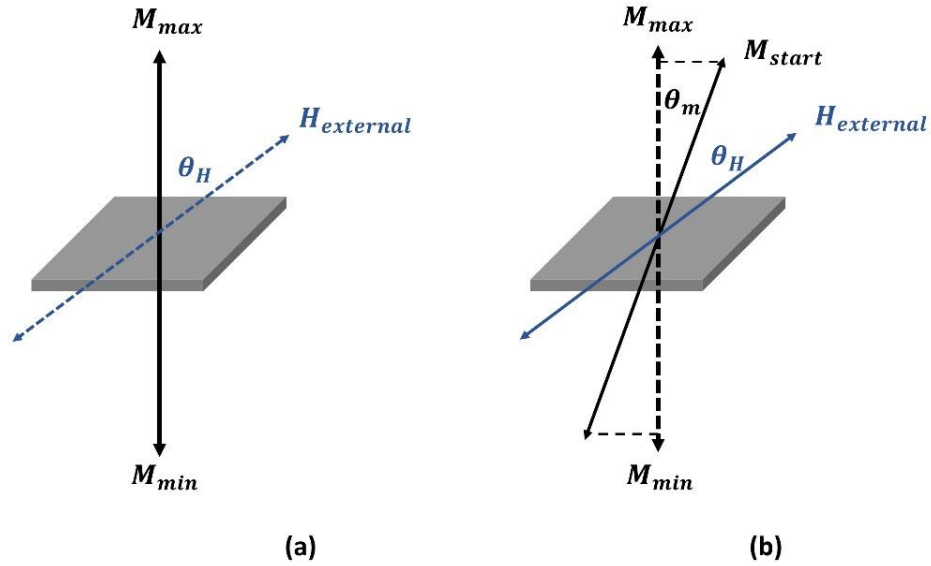


Figure 5.2 Schematic of angled MH measurement.

The maximum magnetic field can be applied in TRMOKE system was 8.65 kOe, which was not high enough to perform in-plane MH measurement as in MPMS-3. However, MH measurement with the $H_{external}$ at an angle θ_H can be performed to extract H_k^{eff} . This measurement is called angled MH measurement in this thesis and the measurement

principle is illustrated in Figure 5.2. The sample was centered between the poles of the magnet, then the magnet was rotated so that the $H_{external}$ was applied at angle θ_H w.r.t. the film normal. As shown in Figure 5.2 (a), 8.65 kOe $H_{external}$ was applied in positive direction to switch the magnetic moment into the positive half space, then the $H_{external}$ was decreased to zero. Due to the perpendicular anisotropy, the magnetic moment will relax to the positive direction, which is shown as the M_{max} in the figure. The MOKE signal was recorded as the value of the magnetic moment in positive direction. Similar process was done with the external field applied in negative direction and the value of magnetic moment in negative direction was recorded as M_{min} . The magnitude of the magnetic moment can be calculated with Equation 5.1.

$$M = \frac{M_{max} - M_{min}}{2} \quad (5.1)$$

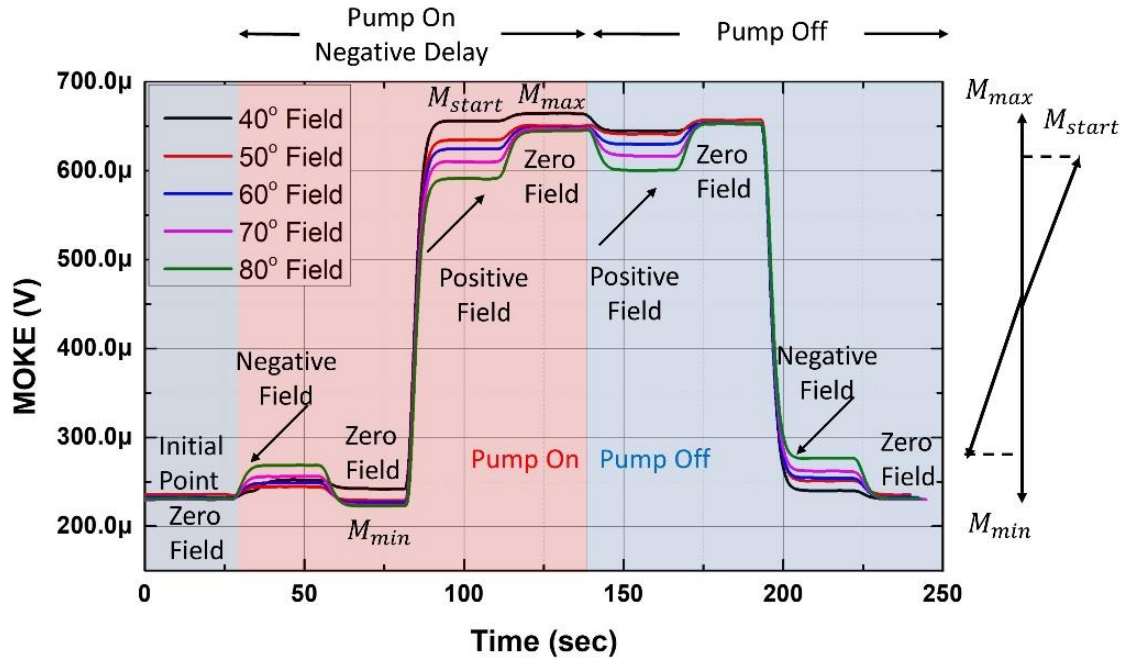


Figure 5.3 Typical angled MH measurements with and without pump pulse.

When $H_{external}$ was held at the 8.65 kOe, the magnetic moment will be deviated to an angle θ_m w.r.t film normal, as shown in Figure 5.2 (b). The MOKE signal with positive field held was recorded as M_{start} , which is the projective value of the magnetic moment in film normal direction. The magnetization direction θ_m can be calculated from Equation 5.2.

$$\theta_m = \arccos \frac{M - (M_{max} - M_{start})}{M} \quad (5.2)$$

The angled MH measurement can also be performed with pump pulse at negative delay position to evaluate the possible heating effect of pump pulse on the magnetic structure.

Figure 5.3 shows a series of typical angled MH measurements. A negative $H_{external}$ was applied first then decreased to zero and M_{min} was recorded. Then a positive $H_{external}$ was applied and held to record M_{start} . Finally, $H_{external}$ was decreased to zero and M_{max} was recorded. The light blue region was the measurement without pump pulse, the light red region was the measurement with the pump pulse at negative delay position, i.e. probe pulse arrives about 1 ms after the pump pulse. Different colored lines were the measurements done with different θ_H . As shown in Figure 5.3, the magnetic moment was tilted further away from the perpendicular direction under larger θ_H . The MOKE signal was slightly affected by the diffracted light of pump pulse with pump pulse applied. After $H_{external}$ was set to zero, the MOKE signal with pump pulse didn't change with time, which indicates no demagnetization effect from the pulse heating. This angled MH measurement is also a necessary step to check the sensitivity, SNR and the linearity of the MOKE signal before TRMOKE measurement.

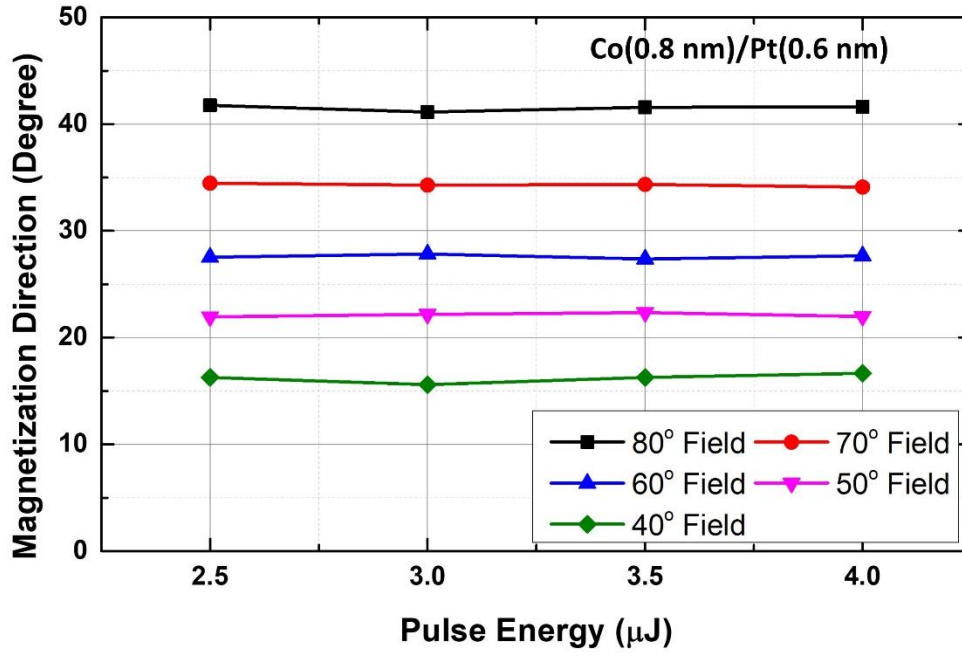


Figure 5.4 Magnetization direction measured under different pulse energy.

Figure 5.4 shows θ_m from angled MH measurement for 0.8 nm t_{Co} with different θ_H under various pump pulse energy, the magnitude of $H_{external}$ was 8.65 kOe. θ_H was varied from 40° to 80° with 10° step size. The pump pulse energy was varied from 2.5 μJ to 4 μJ in 0.5 μJ step size. From the data we can see all the measurements under different pump pulse energies show about the same θ_m as long as the external field conditions are the same, which also indicates the pump heating won't cause demagnetization of the films.

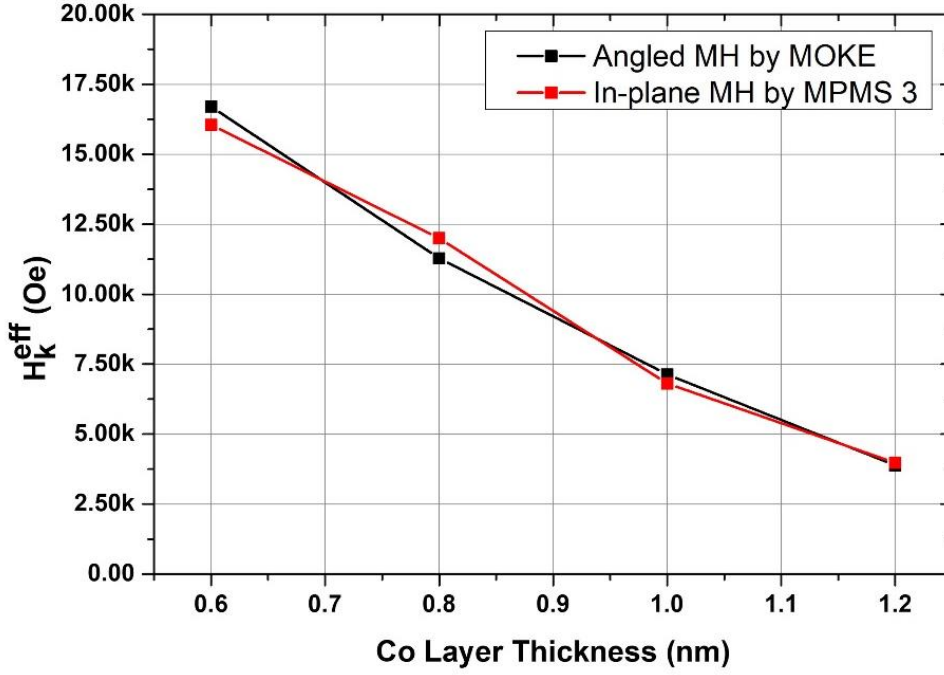


Figure 5.5 Effective anisotropy field dependence on Co layer thickness.

With accurate θ_m extracted from angled MH measurements, the effective anisotropy field H_k^{eff} can also be calculated with Equation 5.3.

$$H_k^{eff} = 2 H_{external} \frac{\sin (\theta_H - \theta_m)}{\sin 2\theta_m} \quad (5.3)$$

The average H_k^{eff} calculated from angled MH measurements were shown as the black curve in Figure 5.5. The value was cross-validated with the value extracted from in-plane MH measurements in Figure 5.1. The red curve corresponds to the field strength where the magnetic moment is about 96% of the saturated moment.

5.1.2 Magnetic Dynamic Study under Different TRMOKE Measurement Conditions

From the analysis in Chapter 3, we can conclude larger θ_H and higher E_p can result in more significant oscillation signal in Z direction. However, for perpendicular magnetic film, larger magnetization angle might result in multi domains structure, which might introduce extrinsic contribution to the damping [81], [82]. Higher pump energy can result in larger oscillation amplitude and break the small angle approximation which will introduce larger deviation between the actual FMR frequency and Kittel model, as analyzed in Section 3.1.2. Here we present the study of TRMOKE measurements to study the effect of pump pulse energy and external field on the magnetic dynamics.

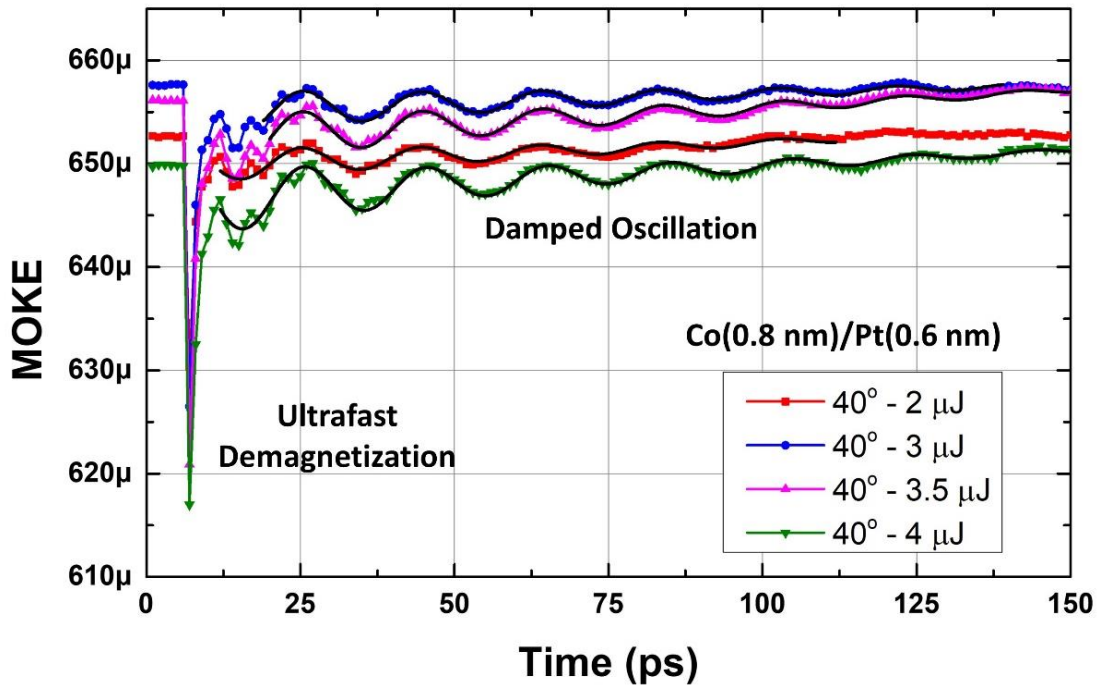


Figure 5.6 TRMOKE measurement performed with different pulse energies for Co(0.8nm)/Pt(0.6nm) film.

First, we performed TRMOKE measurements on Co (0.8 nm)/Pt (0.6 nm) film with different pump pulse energies. All the measurements were performed with θ_H fixed at 40° w.r.t. the film normal. The magnitude of external field was 8.65 kOe. The pump pulse energy was varied from 2.5 μJ to 4 μJ in 0.5 μJ step size. The TRMOKE signals are plotted in Figure 5.6. The black lines were the fitting curves to the phenomenal model (Equation 3.8). A fast demagnetization due to the instant heating of electrons in several ps time scale happened first. After the ultrafast demagnetization, the magnetic moment started to precess around the total field and damped towards the total field direction, which resulted in a damped oscillation signal in Z direction. The amplitude of the oscillation became more obvious as the pump pulse energy went higher since the reduction of anisotropy field was larger. Similar trend was observed in many other studies [77], [80].

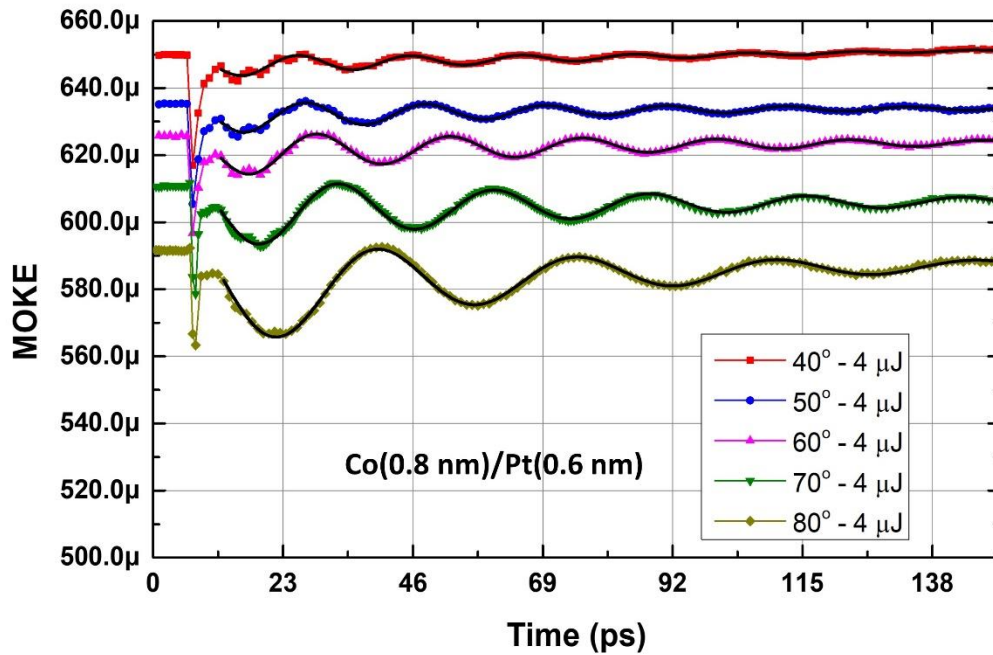


Figure 5.7 TRMOKE measurement performed with different external field angle for Co(0.8nm)/Pt(0.6nm) film.

Figure 5.7 shows the TRMOKE signal measured on Co (0.8 nm)/Pt (0.6 nm) film with different θ_H . The magnitude of $H_{external}$ was 8.65 kOe. θ_H was varied from 40° to 80 ° in 10° step size. The pump pulse energy was fixed at 4 μ J. The black curves were the fitting curves to Equation 3.8. As the θ_H was increased, θ_m also increased accordingly, thus the projective component in Z direction became larger and resulted in larger oscillation amplitude in TRMOKE signal.

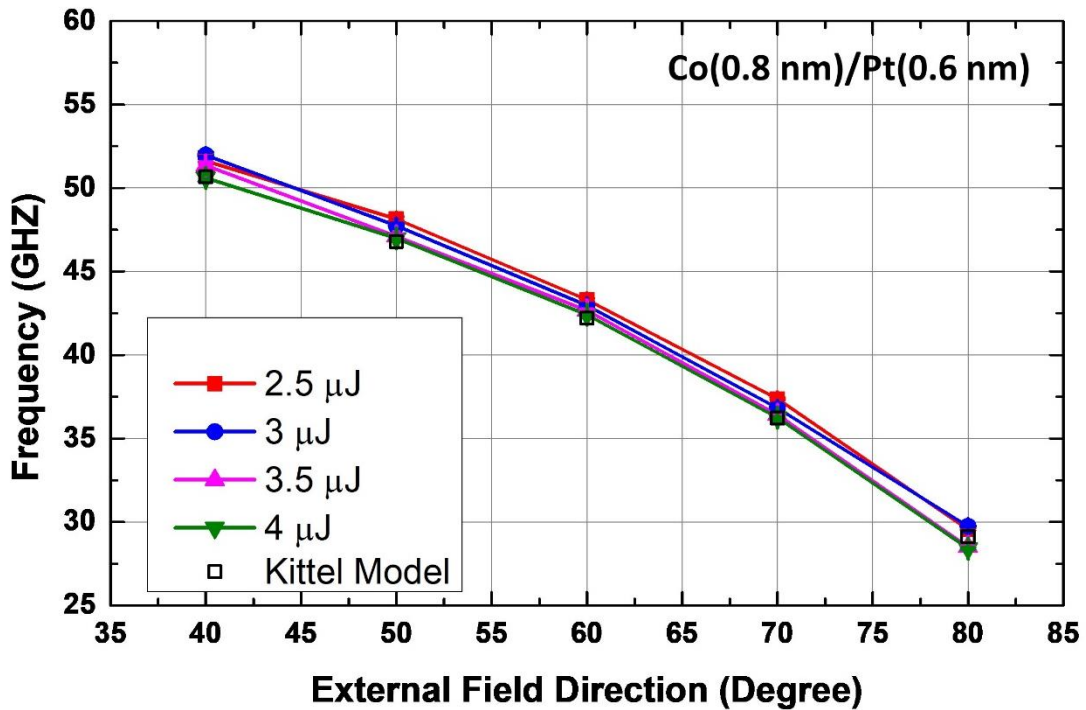


Figure 5.8 FMR frequency dependence on external field direction.

More measurements were performed with different combinations of pump E_P and θ_H . The TRMOKE data was fitted to Equation 3.8 to extract the FMR frequency and lifetime. Figure 5.8 shows the fitting values of FMR frequencies with different pump energies and θ_H . The black open squares are the value from Kittel model with θ_m and H_k^{eff} calculated from angled MH measurement. The oscillation frequencies are almost the same for same $H_{external}$ conditions with a slightly decreasing trend with increasing pulse energy. Figure

5.9 shows the fitting values of the lifetime. The error bars are the fitting errors. The overall trend of lifetime shows an increasing trend with increasing θ_H until 60° then decreasing. The lifetime decreases with increasing pump pulse energy, which is more obvious than the trend of FMR frequency in Figure 5.8.

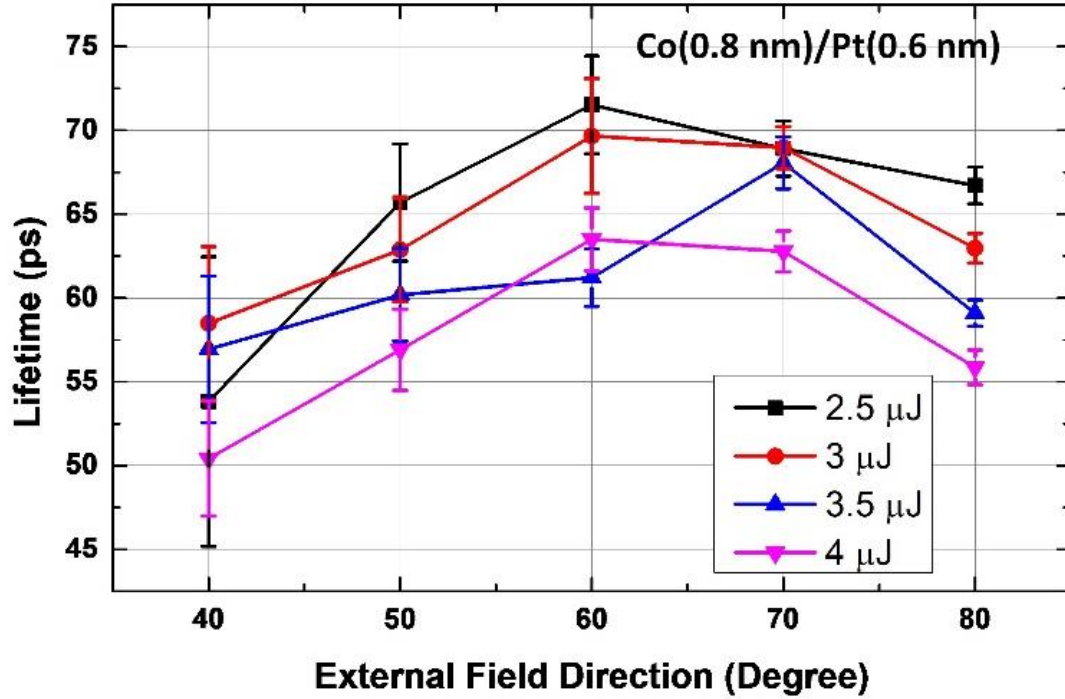


Figure 5.9 Lifetime dependence on external field direction.

Combining the oscillation frequency and the lifetime will give the result of effective damping constant α_{eff} . Figure 5.10 shows α_{eff} under different E_P and θ_H combinations. Each point stands for a single measurement and the error bars come from the fitting error. Considering the effect of θ_H , α_{eff} is the same measured with $\theta_H = 40^\circ$, 50° and 60° . Then a slightly increasing happens with $\theta_H = 70^\circ$. The α_{eff} measured with $\theta_H = 80^\circ$ shows an obviously higher value which is almost twice of the values measured with smaller θ_H . This θ_H dependence might come from the formation of multi domains when the external field lies more in-plane. This trend is the same as the other TRMOKE study of L_{10} FePt [80],

Ni/Co [69], CoCrPt [83]. As for the effect of E_p , the α_{eff} shows a slightly increasing trends with increasing E_p , but not as significantly as the result in the study of CoFeB by Bo Liu [76]. From these results, we can conclude α_{eff} measured below 4 $\mu\text{J}/\text{pulse}$ E_p and $60^\circ \theta_H$ reaches a constant value when the extrinsic contribution is well suppressed and the pump influence is not too high. Thus α_{eff} can be treated as the intrinsic Gilbert damping constant α in these conditions.

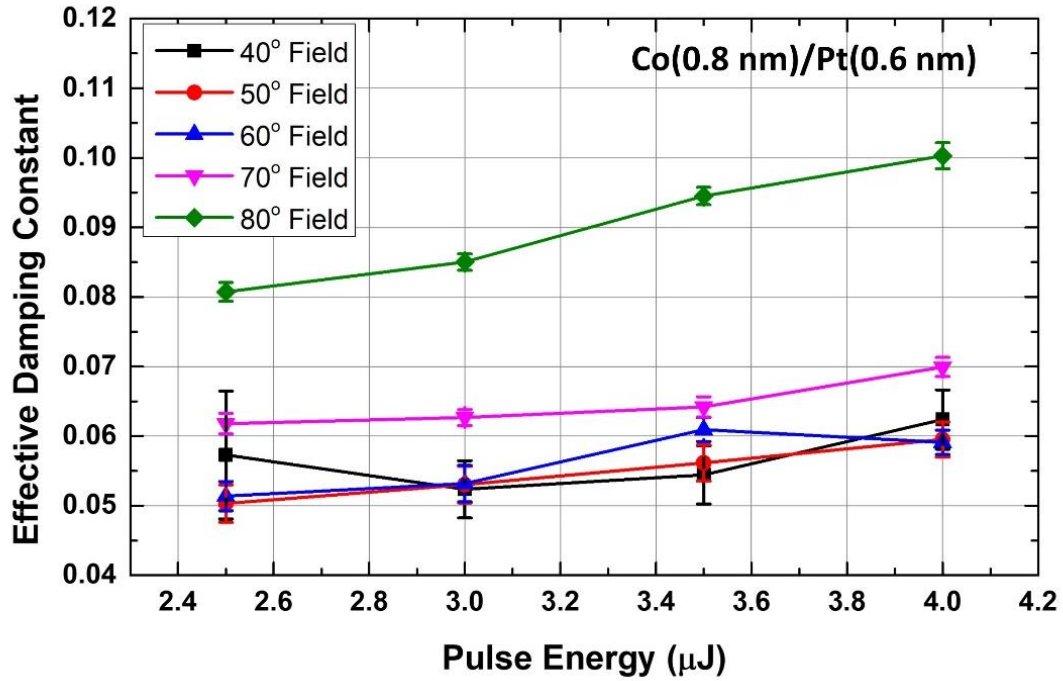


Figure 5.10 Effective damping constant vs. pulse energy.

In the previous experiments, θ_H was changed with fixed field strength, which is defined as method 1. Another way to apply the external field is fixing θ_H and changing the field strength, which is also widely used in other TRMOKE studies [43], [75] and defined as method 2 in this thesis. For the experimental study of method 2, θ_H was fixed at 80° and θ_H was varied to tilt the magnetic moment to different directions. Similar TRMOKE measurements were performed with method 2 and the damping constants were extracted

to compare with the values from method 1. The effective damping constants were plotted with the magnetization direction θ_m for comparison.

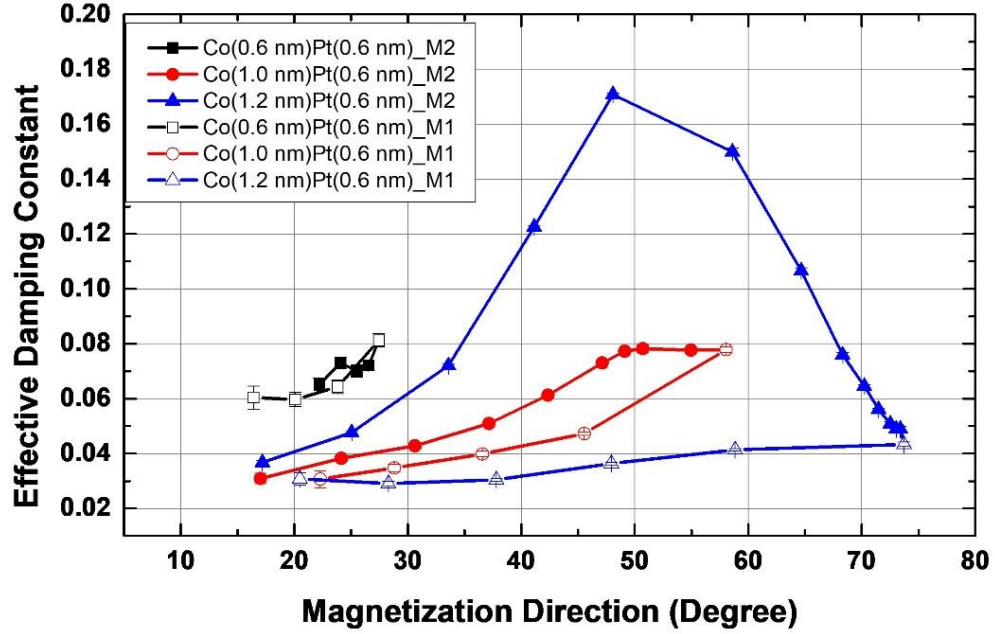


Figure 5.11 Comparison of damping constant measured with different external field conditions.

Figure 5.11 shows even the total magnetic moment points in the same direction in macroscopic view, the trends of effective damping constant are quite different. For the sample with 0.6 nm Co thickness which has the highest anisotropy constant, both methods can only tilt the magnetic moment a small angle away from the perpendicular direction. The damping constants measured from both methods have almost the same value when θ_m are the same. However, the damping constant still goes higher slightly when the magnetic moment lies more in plane. The damping constants with 1.0 nm Co thickness measured with two methods start to show clear difference. For magnetization direction smaller than 30°, the damping constants measured with both methods are almost the same. For magnetization direction larger than 30°, the damping constants measured from method 2

are significantly higher than from method 1. This difference is more obvious in the lowest anisotropy film with 1.2 nm Co thickness. The damping constant is about 0.17 when the magnetization direction is about 48° . This phenomenon comes from the multi domains structure since the magnetic moment can be easily tilted in plane if the sample has low anisotropy, the $H_{external}$ in method 2 was not high enough to suppress the formation of multi domains. Similar divergence of damping constant was also observed in some other TRMOKE studies when $H_{external}$ was almost in-plane and equaled H_k^{eff} [75], [84]. In this thesis we didn't dive into the correction and understanding of this effect. The external field will be applied with maximum field strength and the minimum possible θ_H that can suppress extrinsic contribution but still give enough oscillating signal amplitude to get intrinsic Gilbert damping.

In this section, we studied the experimental conditions for reliable TRMOKE measurements. From the previous analysis, we can conclude the conditions to get accurate measurement on damping constant should be (1) high magnetic field; (2) small field angle; (3) low pump pulse energy. These conditions can well suppress the extrinsic contributions to the effective damping constant leaving only intrinsic Gilbert damping. However, they can also decrease the amplitude of oscillating signal significantly, which might result in larger fitting error in TRMOKE analysis.

5.2 Damping Constant and FMR Frequency of Co/Pt Multilayers

5.2.1 Co/Pt Fabrication and Study of Magnetic Properties

To perform precise study of the Gilbert damping constant in multilayered magnetic thin films. Another series of Co/Pt multilayered thin films were fabricated. All films were prepared by magnetron sputtering on thermally grown SiO₂ substrate with base pressure less than 1×10^{-8} Torr. As shown in Figure 5.12 (a), the film stack from bottom to top was substrate/Ta (3 nm)/Pt (3 nm)/[Co (X nm)/Pt (0.7 nm)]₃/Ta (2 nm). The Co thickness X was varied from 0.6 nm to 1.3 nm in 0.1 nm step size.

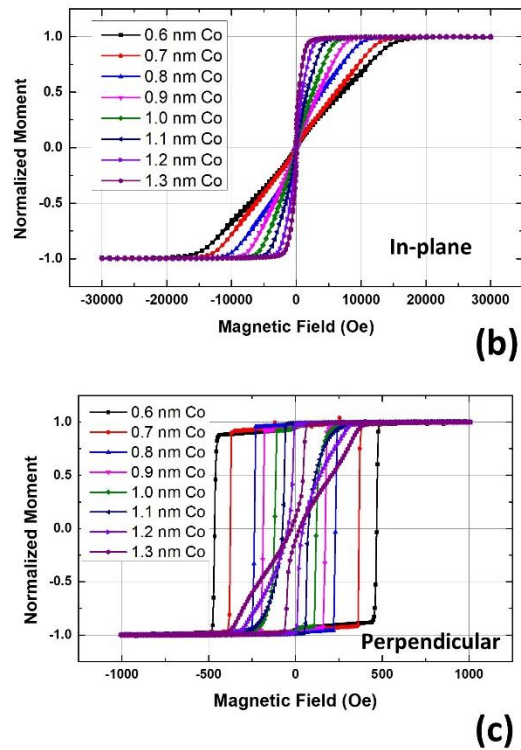
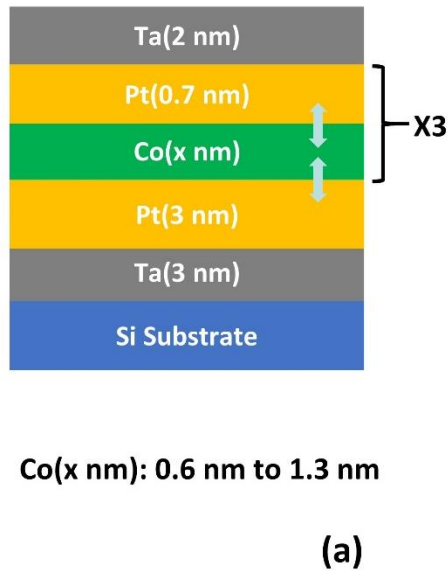


Figure 5.12 (a) Film stack of Co/Pt multilayered magnetic thin film. (b) and (c) In-plane and perpendicular MH loops measured with MPMS-3, respectively.

Figure 5.12 (b) and (c) shows normalized in-plane and perpendicular MH loops measured by MPMS-3, respectively. The square nature of out of plane loops and linear magnetization process of in plane loops confirm all the films have perpendicular anisotropy.

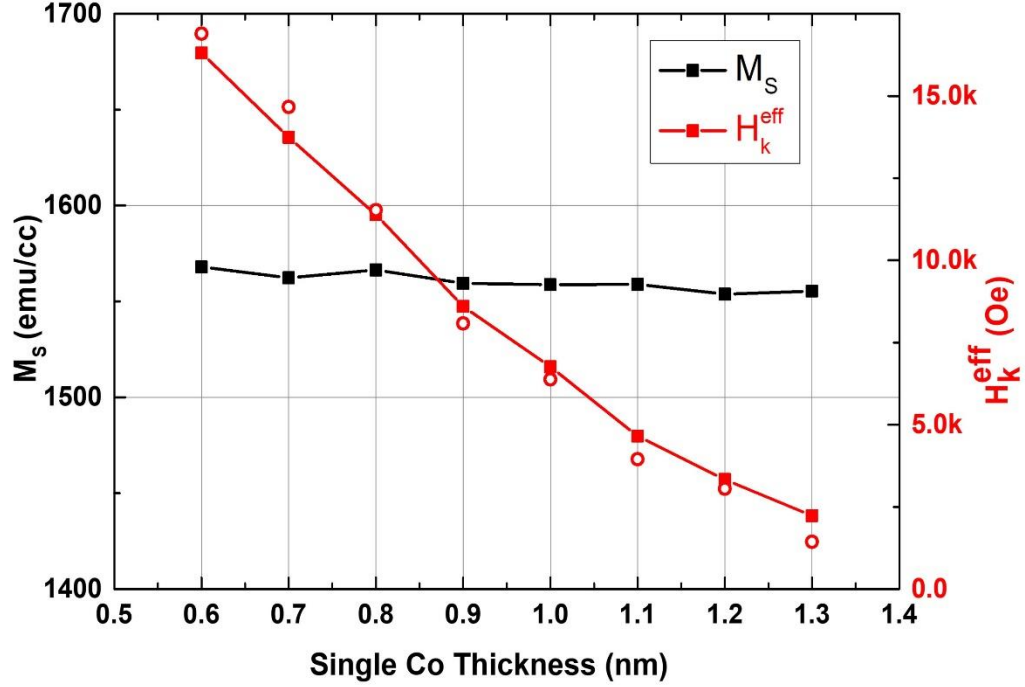


Figure 5.13 M_S and H_k^{eff} dependence on single Co layer thickness. Red open circles: H_k^{eff} from angled MH measurements.

Figure 5.13 shows the M_S and H_k^{eff} vs. single Co layer thickness. The effective perpendicular anisotropy field H_k^{eff} was estimated from the in-plane hard-axis loops in Figure 5.12 and it increases with decreasing t_{Co} . Angled MH loops were also performed with 8.65 kOe $H_{external}$ and θ_H varied from 40° to 80° in 10° step size. At each θ_H , θ_m was measured multiple times to get the average value. The H_k^{eff} was calculated with averaged θ_m . Then the H_k^{eff} calculated from each θ_H was averaged again and plotted as the red open circle in Figure 5.13. The figure shows a good agreement between commercial

tools and home built TRMOKE. The saturation magnetization, M_S , calculated from MPMS-3 measurements was normalized with respect to the total Co volume present in the corresponding thin film. It can be observed that M_S of all samples are higher than that of bulk Co, which is ~ 1400 emu/cc, primarily due to the polarization of Pt at the Co/Pt interfaces [85]. The enhanced M_S and weak $1/t$ dependence of M_S confirm the high quality Co/Pt interfaces in all samples.

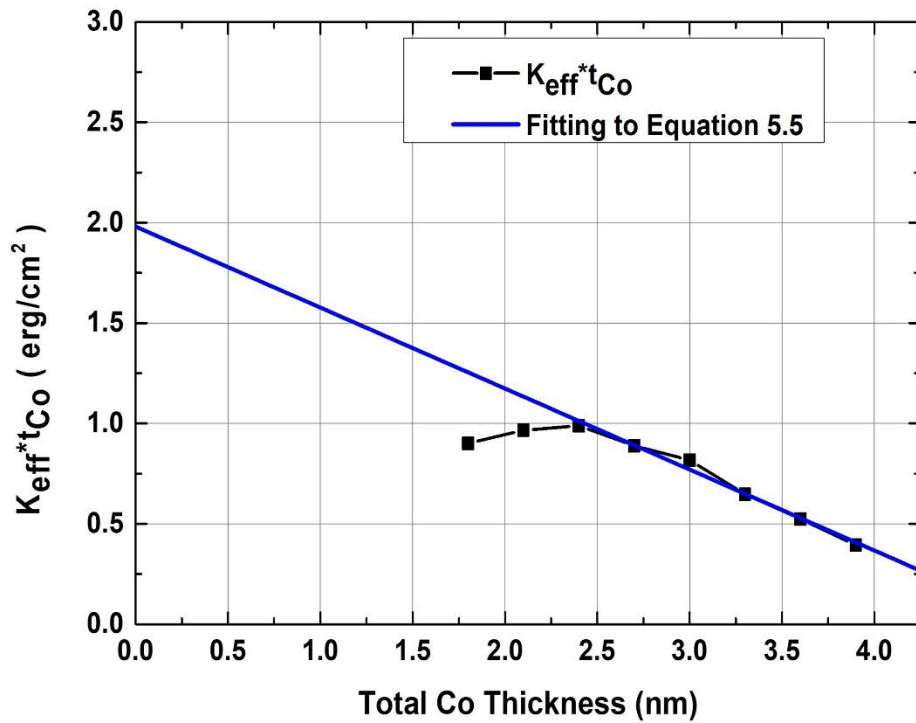


Figure 5.14 Interfacial anisotropy constant calculation.

Figure 5.14 shows the relationship of $K_{eff} * t_{Co}$ with t_{Co} that can be fitted to get the interfacial anisotropy constant K_S . The K_S was calculated with Equation 5.4 [85], [86].

$$K_{eff} = \frac{H_k^{eff} M_S}{2} \quad (5.4)$$

$$K_{eff} * t_{Co} = K_V * t_{Co} + K_S$$

where H_k^{eff} is the effective anisotropy field, t_{Co} is the total Co thickness, K_V is the volume contribution to the anisotropy. M_S is calculated with the thickness of 3 Co layers and 4 Pt layers since the Pt layers are also polarized through the coupling with Co layers. In our case, K_S contains contributions from 6 interfaces. The intersection from fitting the linear part gives 1.98 erg/cm^2 , i.e. the interfacial anisotropy constant is 0.33 erg/cm^2 for each Co/Pt interface.

5.2.2 TRMOKE Study of the Gilbert Damping Constant and FMR Frequency with Different Co Thickness

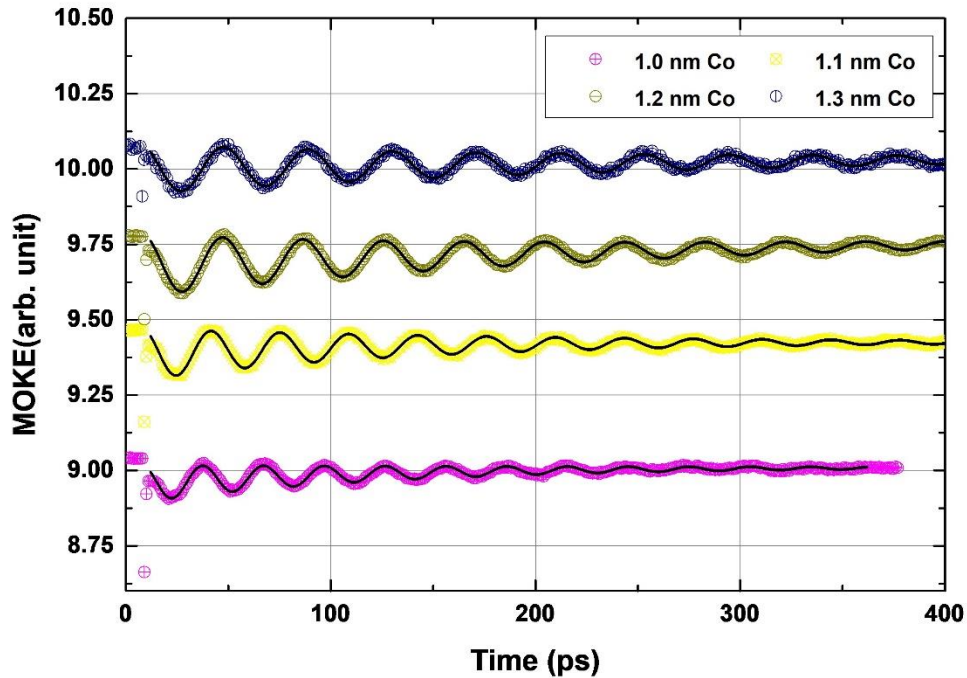


Figure 5.15 Examples of TRMOKE measurement. The black lines are fitting curves to Equation 3.8.

The magnetic dynamics of Co/Pt multilayers were studied with TRMOKE measurement. All measurements were performed with 8.65 kOe external field at $40^\circ \theta_H$ and $3.5 \mu\text{J/pulse}$

pump energy, which was approved to give the intrinsic Gilbert damping constant in Section 5.1.

Figure 5.15 shows some typical examples of measured TRMOKE data. The curves are plotted with offset for clearance. The solid black lines are the fitting curves to Equation 3.8. As shown in the figure, an ultrafast demagnetization happens within < 1 ps time scale. After several ps, the oscillation signal appears, and the amplitude slowly decays with time. The oscillation signal is more obvious for lower anisotropy film, this comes from larger θ_m , θ_m increases from 12.5° to 36° with increasing t_{Co} from 0.6 nm to 1.3 nm, which is in accordance with the decreasing trend of H_k^{eff} . With the magnetic moment lies more in plane, the precession contributes more Z component signal. From Figure 5.15, we can see the detectable precession time scale for low anisotropy film can be extended to more than 500 ps.

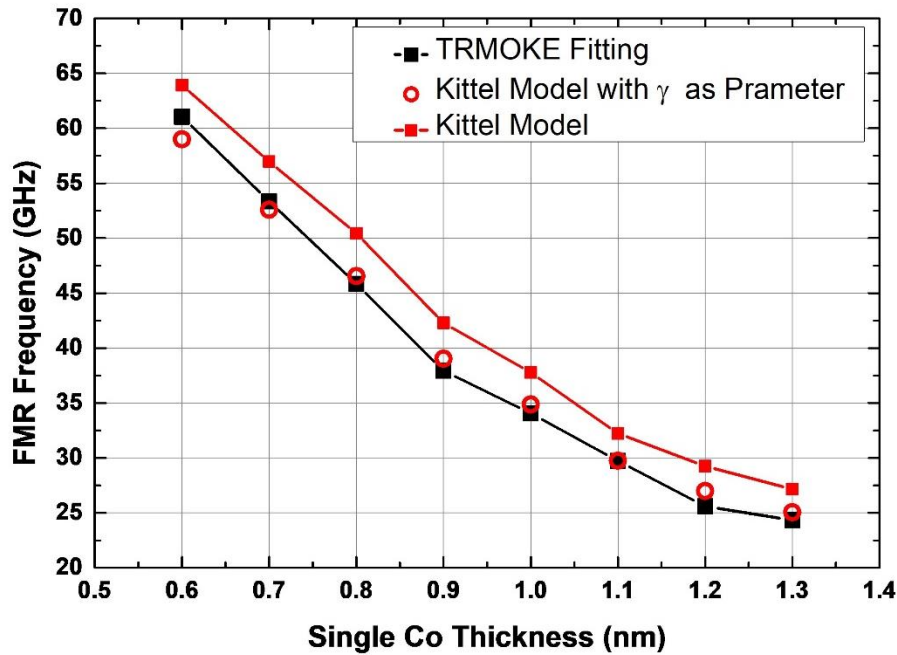


Figure 5.16 FMR frequency vs. single Co layer thickness.

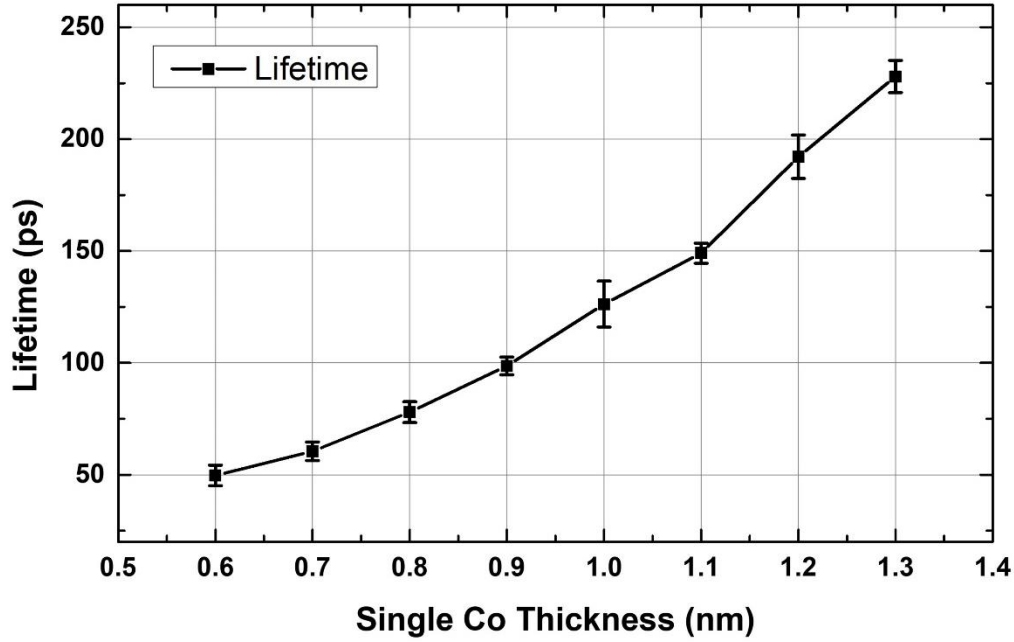


Figure 5.17 Lifetime dependence on single Co layer thickness.

To further study the origin of the damping for interfacial anisotropy structure and minimize the measurement error, we performed at least ten measurements on each sample. All measurements were fitted separately to extract fitting parameters and perform statistical analysis. Figure 5.16 and 5.17 shows the relationship of f and τ vs. single layer Co thickness plotted with error bar, respectively. In Figure 5.16, the black squares are the fitting values from TRMOKE signal with Equation 3.8. The solid red squares are the values calculated from Kittel model (Equation 3.6) with $\gamma = 1.76 \times 10^7 / (\text{s} * \text{Oe})$. The red open circle was the fitting of experimental data to Kittel model with γ as fitting parameter. The fitting value of γ is $1.62 \times 10^7 / (\text{s} * \text{Oe})$, which is about 10% smaller than the γ of electron. As shown in the figures, with increasing t_{Co} , the precession frequency decreases and the lifetime increases. The relative standard deviation of FMR frequency is much smaller than that of lifetime, which indicates FMR frequency can be precisely measured with TRMOKE.

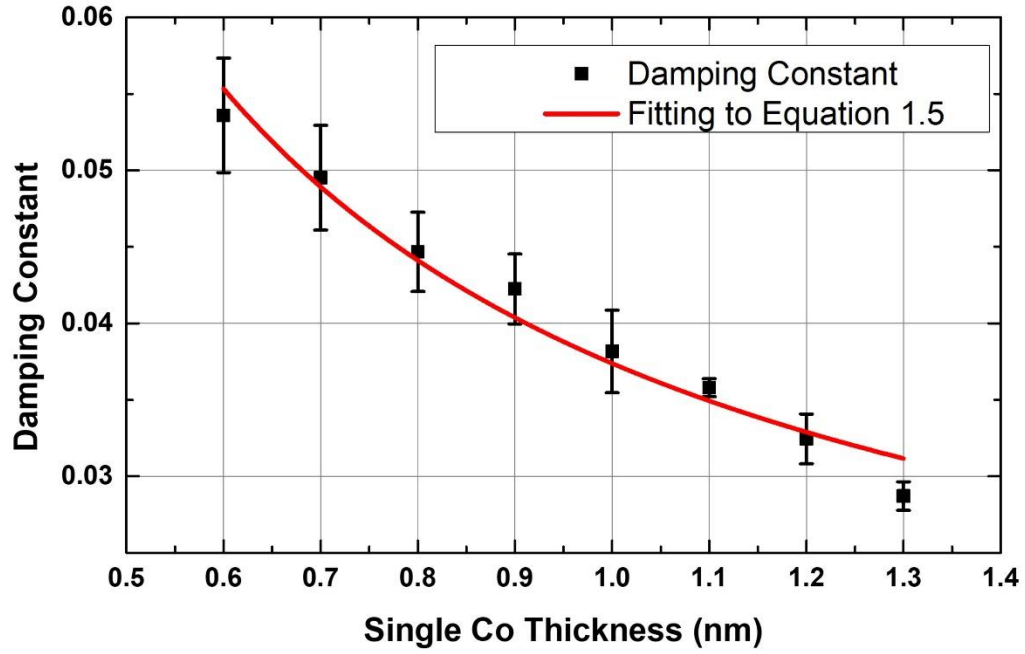


Figure 5.18 Damping constant vs. single Co layer thickness.

Figure 5.18 shows the Gilbert damping constant vs. single Co layer thickness. Compared with other similar studies on Co/Pt multilayers, our damping constant is much smaller [28], [43]. One possible reason is our external field is 8.65 kOe which is significantly larger than the field used in other studies, 3.08 kOe in Reference [43], 4 kOe in Reference [28]. Large external field strength can well suppress the extrinsic contributions to the damping, such as magnon-magnon scattering, thus the effective damping constant we get can be viewed as intrinsic Gilbert damping constant. Another possible reason is the relatively small pump influence we implied, our value is 0.1 mJ/cm^2 , which is much smaller than the values in other studies, 26 mJ/cm^2 in Reference [43], 3.8 mJ/cm^2 in Reference [28]. The precession angle was estimated through the fitting oscillation amplitude and found to be smaller than 1° . From these comparisons, we can conclude the extrinsic damping constant is well suppressed in experiment and the most

accurate study of the intrinsic Gilbert damping constant of Co/Pt multilayers with different Co thickness by far was achieved. The red line is the fitting curve to Equation 1.5, which shows a well-fitting of the experiment values to the theoretical equation. The fitting interfacial contribution α_s is 0.027, the bulk contribution α_b is 0.010. This bulk contribution value is very close to the reported value in the study on [Co(X nm)/Pd(0.9nm)]₈ multilayers, which is 0.011 [87]. The magnetic layer thickness used in Equation 1.5 is single Co layer thickness in nm unit. The inverse dependence proves the Gilbert damping of Co/Pt multilayer magnetic thin film is enhanced through the interfacial coupling.

5.3 Comparison of the Gilbert Damping in Sandwiched Magnetic Thin Films

As proved in Section 5.2, the Gilbert damping constant is enhanced in multilayered magnetic thin film through the interfacial coupling between magnetic (M) and nonmagnetic (NM) interfaces. The interfacial anisotropy and the material type of NM play an important role in the control of the damping since the first one determines the coupling strength between spin system and orbital system and the later affects the damping rate of spin angular momentum in the NM layer. Co/Pt and Co/Ir multilayered thin films were fabricated to study the effect of NM materials and interfacial coupling in this thesis. The films stacks of the four samples fabricated with the same sputtering parameters as described in Section 5.2.1 was shown in Figure 5.19. The films were sandwiched structure with 1 nm Co between two 3 nm non-magnetic layers. The materials of the two non-magnetic layers were the combinations between Pt and Ir.

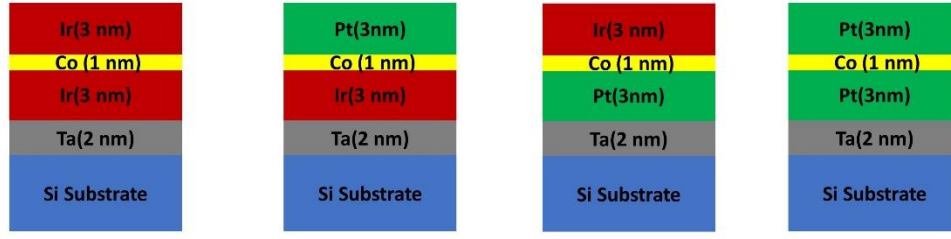


Figure 5.19 Film stacks for the comparison of sandwiched magnetic thin films with Co as magnetic layer, Pt and Ir as non-magnetic layer.

Figure 5.20 shows the normalized perpendicular and in-plane MH loops measured with AGM and MPMS-3. All the films have perpendicular anisotropy. As shown in Figure 5.20 (b), Pt/Co/Ir film has the highest H_k^{eff} which is about 9.5 kOe. Ir/Co/Ir and Pt/Co/Pt films have 7.8 kOe and 6.8 kOe H_k^{eff} , respectively. Ir/Co/Pt film has the lowest H_k^{eff} , which is about 3.8 kOe. The difference between Pt/Co/Ir and Ir/Co/Pt films indicates the interfacial effect is related to the growing sequence of the film and affected by the mismatch of lattice between adjacent layers.

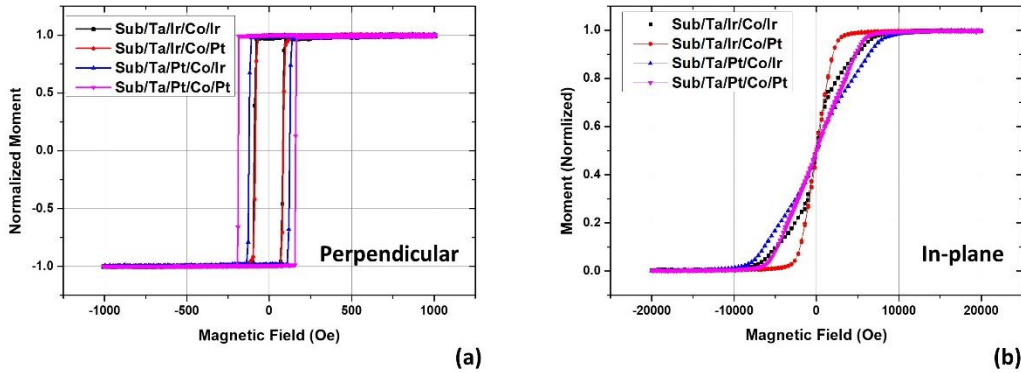


Figure 5.20 Perpendicular and in-plane MH loops for sandwiched magnetic thin films.

The TRMOKE measurements for these films were performed with 2.5 μJ pulse energy, 8.65 kOe external field and θ_H varied from 60° to 80° in 10° step size. The effective damping constant was shown in Figure 5.21. As shown in the figure, the extrinsic contribution caused by θ_H is negligible. With low pulse energy and high external field

strength, the extrinsic contribution to the damping was well suppressed, leaving only intrinsic Gilbert damping. Considering Ir/Co/Ir and Pt/Co/Pt samples with close H_k^{eff} , which are 7.8 kOe and 6.8 kOe H_k^{eff} , respectively, the damping constants are quite different, which are ~ 0.15 and ~ 0.08 , respectively. Thus, Ir is a more effective spin sinking material than Pt, which is in accordance with the results for spin diffusive length of Ir and Pt which are 0.5 nm and 1.2 nm respectively [88], [89]. For Pt/Co/Ir and Ir/Co/Pt films, even the materials of adjacent layers are the same, the Gilbert damping constants are not similar, which are ~ 0.13 and ~ 0.09 , respectively. This mainly comes from the difference of the interface coupling strength. The H_k^{eff} of Pt/Co/Ir is 2.5 times of the H_k^{eff} of Ir/Co/Pt which shows stronger spin orbital coupling strength between interface for Pt/Co/Ir. From theses comparison we can conclude, the NM material and interfacial coupling strength determines the Gilbert damping together, high spin orbital coupling of NM material and high interfacial coupling between FM/NM result in high Gilbert damping constant.

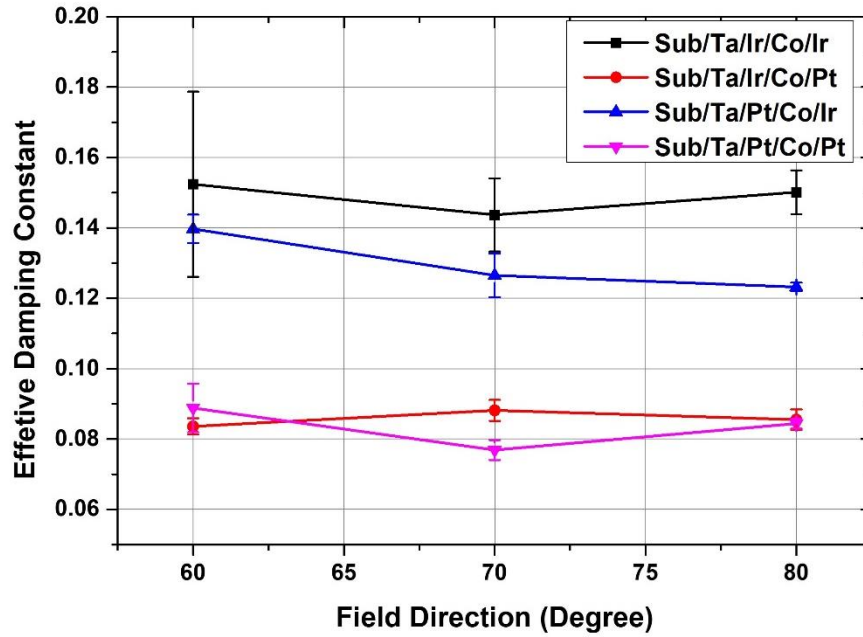


Figure 5.21 Damping constant vs. external field direction for sandwiched magnetic thin films with Pt and Ir as nonmagnetic layers.

In this chapter, we used TRMOKE to study the damping constant of $[\text{Co}(X \text{ nm})/\text{Pt}(0.7 \text{ nm})]_3$ multilayered films with Co layer thickness from 0.6 nm to 1.3 nm. With high external field, small external field angle and low pump influence, the extrinsic contribution to the damping is well suppressed. The Gilbert damping constant decreases from 0.054 to 0.029 with increasing Co layer thickness. Further fitting analysis shows the damping constant has an interfacial contribution which is inversely proportional to the magnetic layer thickness and a constant value from bulk contribution. For multilayered magnetic thin films, the Gilbert damping constant is enhanced through the interfacial coupling between magnetic and nonmagnetic layers. Comparison of sandwiched magnetic thin films with Pt/Ir as nonmagnetic layers shows high spin orbital coupling of NM material and high interfacial coupling between FM/NM result in high Gilbert damping constant in multilayered magnetic thin films.

6 Summary and Discussion of Future Directions

The work of this thesis was focused on the pump-probe study of the Curie temperature distribution of HAMR media and the Gilbert damping constant in multilayered magnetic thin films. Two pump-probe methodologies were studied and understood with micromagnetic simulation. The pump-probe experimental systems were successfully built to study the Curie temperature distribution and the Gilbert damping constant for the first time in Data Storage Systems Center.

The Curie temperature distribution was measured through the switching curve of saturated media under sub-ns pulse laser heating. The Curie temperature distribution of HAMR media with $\text{BaFe}_{12}\text{O}_{19}+\text{C}$ as grain boundary was measured and proved to be smaller than that of the media with C grain boundary, which is a novel way to control the Curie temperature distribution for small grain size. The same system was extended to measure the temperature dependence of anisotropy field around Curie temperature for the first time.

For the future work of Curie temperature distribution measurement, the system may be updated with temperature measurement capability through thermal reflectance that can provide in situ measurement of the temperature.

The micromagnetic modeling with pulse laser heating was established to understand the magnetic dynamics excited by ultrafast laser heating. Though the model was based on single spin, it gave an in-depth understanding of the TRMOKE measurement that was used to guide and correct the experiments. The TRMOKE system built in this thesis has high SNR and long-term stability with cutting edge techniques. The detailed study determined the best measurement conditions for TRMOKE measurement of magnetic films with perpendicular anisotropy are: (1) high external field, (2) low pulse energy, (3) small angle

between external field direction and perpendicular direction. The intrinsic Gilbert damping of Co/Pt multilayered magnetic thin films was accurately measured with the extrinsic contribution well suppressed. In FM/NM multilayered magnetic thin film, the Gilbert damping constant contains a bulk contribution from magnetic layer and an interfacial contribution through the interfacial effect at FM/NM interface. Comparison of sandwiched magnetic thin films with Pt/Ir as nonmagnetic layers shows Ir is a more effective spin sinking material than Pt. High spin orbital coupling of NM material and high interfacial coupling between FM/NM result in high Gilbert damping constant in multilayered magnetic thin films. The TRMOKE system also provided intensive study on the Gilbert damping constant for industrial sponsors with productive results.

For the future simulation work of magnetic dynamics, a more complicated model with the capability of simulating magnetic domains and the variation of local magnetic properties should be developed to study the extrinsic contributions of the damping. As for the experimental work, the method to control interfacial anisotropy constant without changing the materials should be developed to further investigate the interfacial effect. Spin wave mode in addition to the damping dynamics [83], [84], [92] was also observed for thick magnetic films from industrial sponsors. The result was not shown in this thesis, but this is an important area in understanding the origin and transmission of spin waves.

References

- [1] H. J. Richter, “The transition from longitudinal to perpendicular recording,” *J. Phys. D. Appl. Phys.*, vol. 40, no. 9, 2007.
- [2] “Toshiba : Press Releases 14 December, 2004,” *www.toshiba.co.jp*.
- [3] IDEMA, “ASTC Technology Roadmap - 2014 v8,” 2014. [Online]. Available: http://idema.org/?page_id=2269. [Accessed: 26-Sep-2019].
- [4] A. Gandomi and M. Haider, “Beyond the hype: Big data concepts, methods, and analytics,” *Int. J. Inf. Manage.*, 2015.
- [5] M. H. Kryder *et al.*, “Heat Assisted Magnetic Recording,” *Proc. IEEE*, vol. 96, no. 11, pp. 1810–1835, Nov. 2008.
- [6] J. G. Zhu, X. Zhu, and Y. Tang, “Microwave assisted magnetic recording,” *IEEE Trans. Magn.*, vol. 44, no. 1, pp. 125–131, 2008.
- [7] S. Mao *et al.*, “Commercial TMR heads for hard disk drives: Characterization and extendibility at 300 Gbit/in²,” *IEEE Trans. Magn.*, vol. 42, no. 2, pp. 97–102, 2006.
- [8] C. J. Lin *et al.*, “45nm low power CMOS logic compatible embedded STT MRAM utilizing a reverse-connection 1T/1MTJ cell,” *Tech. Dig. - Int. Electron Devices Meet. IEDM*, pp. 279–282, 2009.
- [9] S. W. Chung *et al.*, “4Gbit density STT-MRAM using perpendicular MTJ realized with compact cell structure,” *Tech. Dig. - Int. Electron Devices Meet. IEDM*, pp. 27.1.1-27.1.4, 2017.
- [10] H. Li and J. G. Zhu, “Understanding the impact of T_c and H_k variation on signal-

- to-noise ratio in heat-assisted magnetic recording,” *J. Appl. Phys.*, vol. 115, no. 17, pp. 1–4, 2014.
- [11] D. Weller, O. Mosendz, G. Parker, S. Pisana, and T. S. Santos, “L10 FePtX-Y media for heat-assisted magnetic recording,” *Phys. Status Solidi Appl. Mater. Sci.*, vol. 210, no. 7, pp. 1245–1260, 2013.
- [12] M. Zhang, T. Zhou, and Z. Yuan, “Analysis of switchable spin torque oscillator for microwave assisted magnetic recording,” *Adv. Condens. Matter Phys.*, vol. 2015, 2015.
- [13] J.-G. Zhu and Y. Wang, “Microwave Assisted Magnetic Recording Utilizing Perpendicular Spin Torque Oscillator With Switchable Perpendicular Electrodes,” *IEEE Trans. Magn.*, vol. 46, no. 3, pp. 751–757, Mar. 2010.
- [14] J.-H. Moon, T. Y. Lee, and C.-Y. You, “Relation between switching time distribution and damping constant in magnetic nanostructure OPEN,” *Sci. Rep*, vol. 8, p. 13288, 2018.
- [15] S. Bhatti, R. Sbiaa, A. Hirohata, H. Ohno, S. Fukami, and S. N. Piramanayagam, “Spintronics based random access memory: a review,” *Materials Today*, vol. 20, no. 9. Elsevier B.V., pp. 530–548, 01-Nov-2017.
- [16] X. Zhu and J. G. Zhu, “Effect of damping constant on magnetic switching in spin torque driven perpendicular MRAM,” in *IEEE Transactions on Magnetism*, 2007, vol. 43, no. 6, pp. 2349–2351.
- [17] A. Moser *et al.*, “Magnetic recording: advancing into the future,” 2002.
- [18] D. Weller and A. Moser, “Thermal effect limits in ultrahigh-density magnetic

- recording,” *IEEE Trans. Magn.*, vol. 35, no. 6, pp. 4423–4439, 1999.
- [19] S. H. Charap, P. L. Lu, and Y. He, “Thermal stability of recorded information at high densities,” *IEEE Trans. Magn.*, vol. 33, no. 1 PART 2, pp. 978–983, 1997.
- [20] E. C. Stoner and E. P. Wohlfarth, “A Mechanism of Magnetic Hysteresis in Heterogeneous Alloys,” *Philos. Trans. R. Soc. A Math. Phys. Eng. Sci.*, vol. 240, no. 826, pp. 599–642, May 1948.
- [21] J. G. Zhu, “New heights for hard disk drives,” *Materials Today*, vol. 6, no. 7–8. Elsevier, pp. 22–31, 2003.
- [22] Y. Tao, A. Eichler, T. Holzherr, and C. L. Degen, “Ultrasensitive mechanical detection of magnetic moment using a commercial disk drive write head,” *Nat. Commun.*, vol. 7, 2016.
- [23] S. Pisana *et al.*, “Measurement of the Curie temperature distribution in FePt granular magnetic media,” *Appl. Phys. Lett.*, vol. 104, no. 16, p. 162407, Apr. 2014.
- [24] A. Chernyshov *et al.*, “Measurement of Curie temperature distribution relevant to heat assisted magnetic recording,” *J. Appl. Phys.*, vol. 117, no. 17, p. 17D111, May 2015.
- [25] Z. Dai, H. Li, and J. G. J. Zhu, “Measuring Temperature Dependence of Anisotropy Field in Heat-Assisted Magnetic Recording Media by Pump-Probe Method,” *IEEE Trans. Magn.*, vol. 52, no. 7, pp. 1–4, Jul. 2016.
- [26] T. L. Gilbert, “A phenomenological theory of damping in ferromagnetic materials,” *IEEE Trans. Magn.*, vol. 40, no. 6, pp. 3443–3449, Nov. 2004.
- [27] S. S. Kalarickal *et al.*, “Ferromagnetic resonance linewidth in metallic thin films:

- Comparison of measurement methods,” *J. Appl. Phys.*, vol. 99, no. 9, p. 93909, 2006.
- [28] S. Mizukami *et al.*, “Gilbert damping in perpendicularly magnetized Pt/Co/Pt films investigated by all-optical pump-probe technique,” *Appl. Phys. Lett.*, vol. 96, no. 15, p. 152502, 2010.
- [29] I. Neudecker, G. Woltersdorf, B. Heinrich, T. Okuno, G. Gubbiotti, and C. H. Back, “Comparison of frequency, field, and time domain ferromagnetic resonance methods,” *J. Magn. Magn. Mater.*, vol. 307, no. 1, pp. 148–156, Dec. 2006.
- [30] S. Azzawi, A. T. Hindmarch, and D. Atkinson, “Magnetic damping phenomena in ferromagnetic thin-films and multilayers,” *J. Phys. D: Appl. Phys.*, vol. 50, no. 47, p. 473001, 2017.
- [31] M. A. W. Schoen, J. M. Shaw, H. T. Nembach, M. Weiler, and T. J. Silva, “Radiative damping in waveguide-based ferromagnetic resonance measured via analysis of perpendicular standing spin waves in sputtered permalloy films,” *Phys. Rev. B - Condens. Matter Mater. Phys.*, vol. 92, no. 18, p. 184417, 2015.
- [32] S. Ishikawa *et al.*, “Co/Pt multilayer-based magnetic tunnel junctions with a CoFeB/Ta insertion layer,” *J. Appl. Phys.*, vol. 115, no. 17, pp. 3–6, 2014.
- [33] J. H. Park, C. Park, T. Jeong, M. T. Moneck, N. T. Nufer, and J. G. Zhu, “CoPt multilayer based magnetic tunnel junctions using perpendicular magnetic anisotropy,” *J. Appl. Phys.*, vol. 103, no. 7, pp. 5–8, 2008.
- [34] P. J. Metaxas *et al.*, “Creep and flow regimes of magnetic domain-wall motion in ultrathin Pt/Co/Pt films with perpendicular anisotropy,” *Phys. Rev. Lett.*, vol. 99, no. 21, pp. 1–4, 2007.

- [35] K. Wang, M. C. Wu, S. Lepadatu, J. S. Claydon, C. H. Marrows, and S. J. Bending, “Optimization of Co/Pt multilayers for applications of current-driven domain wall propagation,” *J. Appl. Phys.*, vol. 110, no. 8, 2011.
- [36] V. Kamberský, “Spin-orbital Gilbert damping in common magnetic metals,” *Phys. Rev. B - Condens. Matter Mater. Phys.*, vol. 76, no. 13, pp. 1–10, 2007.
- [37] V. Kamberský, “On ferromagnetic resonance damping in metals,” *Czechoslovak Journal of Physics*, vol. 26, no. 12, pp. 1366–1383, 1976.
- [38] M. T. Johnson, P. J. H. Bloemen, F. J. A. Den Broeder, and J. J. De Vries, “Magnetic anisotropy in metallic multilayers,” *Reports Prog. Phys.*, vol. 59, no. 11, pp. 1409–1458, 1996.
- [39] T. Qu and R. H. Victora, “Theoretical study of interfacial damping in perpendicular anisotropy superlattices along multiple crystal orientations,” *Phys. Rev. B*, vol. 93, no. 22, pp. 1–8, 2016.
- [40] E. Barati and M. Cinal, “Gilbert damping in binary magnetic multilayers,” *Phys. Rev. B*, vol. 95, no. 13, pp. 1–14, 2017.
- [41] A. Caprile, M. Pasquale, M. Kuepferling, M. Coisson, T. Y. Lee, and S. H. Lim, “Microwave Properties and Damping in [Pt/Co] Multilayers with Perpendicular Anisotropy,” *IEEE Magn. Lett.*, vol. 5, pp. 3–6, 2014.
- [42] N. Fujita, N. Inaba, F. Kirino, S. Igarashi, K. Koike, and H. Kato, “Damping constant of Co/Pt multilayer thin-film media,” *J. Magn. Magn. Mater.*, 2008.
- [43] A. Barman, S. Wang, O. Hellwig, A. Berger, E. E. Fullerton, and H. Schmidt, “Ultrafast magnetization dynamics in high perpendicular anisotropy [CoPt]_n

- multilayers,” in *Journal of Applied Physics*, 2007, vol. 101, no. 9, pp. 9–102.
- [44] E. Barati, M. Cinal, D. M. Edwards, and A. Umerski, “Gilbert damping in magnetic layered systems,” *Phys. Rev. B - Condens. Matter Mater. Phys.*, vol. 90, no. 1, pp. 1–16, 2014.
- [45] J. Kerr, “XLIII. On rotation of the plane of polarization by reflection from the pole of a magnet,” *London, Edinburgh, Dublin Philos. Mag. J. Sci.*, vol. 3, no. 19, pp. 321–343, 1877.
- [46] T. Haider, “A Review of Magneto-Optic Effects and Its Application,” *Int. J. Electromagn. Appl.*, vol. 7, no. 1, pp. 17–24, 2017.
- [47] Z. Q. Qiu and S. D. Bader, “Surface magneto-optic Kerr effect Surface magneto-optic Kerr effect,” *Rev. Sci. Instrum.*, vol. 71, no. 3, p. 1243, 2000.
- [48] E. Oblak, P. Riego, L. Fallarino, A. Martínez-De-Guerenu, F. Arizti, and A. Berger, “Ultrasensitive transverse magneto-optical Kerr effect measurements by means of effective polarization change detection,” *J. Phys. D. Appl. Phys.*, vol. 50, no. 23, pp. 23–24, 2017.
- [49] C. B. Rong *et al.*, “Size-dependent chemical and magnetic ordering in L10-FePt nanoparticles,” *Adv. Mater.*, vol. 18, no. 22, pp. 2984–2988, 2006.
- [50] A. Lyberatos, D. Weller, G. J. Parker, and B. C. Stipe, “Size dependence of the Curie temperature of L10-FePt nanoparticles,” *J. Appl. Phys.*, vol. 112, no. 11, p. 113915, 2012.
- [51] C. Papusoi *et al.*, “The effect of film thickness on Curie temperature distribution and magnetization reversal mechanism for granular L10 FePt films,” *J. Phys. D. Appl.*

Phys., vol. 50, no. 28, 2017.

- [52] O. Hovorka *et al.*, “The Curie temperature distribution of FePt granular magnetic recording media,” *Appl. Phys. Lett.*, vol. 101, no. 5, p. 52406, 2012.
- [53] H. Li, “Storage Physics and Noise Mechanism in Heat-Assisted Magnetic Recording,” Carnegie Mellon University, 2016.
- [54] B. Zhou, B. S. D. C. S. Varaprasad, Z. Dai, D. E. Laughlin, and J. G. Zhu, “The effect of adding a magnetic oxide in the grain boundaries of HAMR media,” *Appl. Phys. Lett.*, vol. 113, no. 8, p. 82401, 2018.
- [55] A. Barman, T. Kimura, Y. Otani, Y. Fukuma, K. Akahane, and S. Meguro, “Benchtop time-resolved magneto-optical Kerr magnetometer,” *Rev. Sci. Instrum.*, vol. 79, no. 12, p. 140901, 2008.
- [56] M. Sharma, S. C. Kashyap, H. C. Gupta, M. C. Dimri, and K. Asokan, “Enhancement of Curie temperature of barium hexaferrite by dense electronic excitations,” *AIP Adv.*, vol. 4, no. 7, p. 77129, 2014.
- [57] A. F. Clark, W. M. Haynes, V. A. Deason, and R. J. Trapani, “Low temperature thermal expansion of barium ferrite,” *Cryogenics (Guildf.)*, vol. 16, no. 5, pp. 267–270, May 1976.
- [58] E. Yang, D. E. Laughlin, and J. G. Zhu, “Correction of order parameter calculations for FePt perpendicular thin films,” *IEEE Trans. Magn.*, vol. 48, no. 1, pp. 7–12, 2012.
- [59] B. S. D. C. S. Varaprasad, M. Chen, Y. K. Takahashi, and K. Hono, “L10-Ordered FePt-Based Perpendicular Magnetic Recording Media for Heat-Assisted Magnetic

- Recording,” *IEEE Trans. Magn.*, vol. 49, no. 2, pp. 718–722, Feb. 2013.
- [60] J. U. Thiele, K. R. Coffey, M. F. Toney, J. A. Hedstrom, and A. J. Kellock, “Temperature dependent magnetic properties of highly chemically ordered Fe₅₅-xNi_xPt₄₅L₁₀ films,” *J. Appl. Phys.*, vol. 91, no. 10, pp. 6595–6600, 2002.
- [61] J. G. Zhu and H. Li, “Understanding signal and noise in heat assisted magnetic recording,” *IEEE Trans. Magn.*, vol. 49, no. 2, pp. 765–772, Feb. 2013.
- [62] Z. Lin, L. V. Zhigilei, and V. Celli, “Electron-phonon coupling and electron heat capacity of metals under conditions of strong electron-phonon nonequilibrium,” *Phys. Rev. B - Condens. Matter Mater. Phys.*, vol. 77, no. 7, pp. 1–17, 2008.
- [63] C. H. Kim, J.-H. H. Shim, K. M. Lee, J.-R. R. Jeong, D.-H. H. E. Kim, and D.-H. H. E. Kim, “Coherent phonon control via electron-lattice interaction in ferromagnetic Co/Pt multilayers,” *Sci. Rep.*, vol. 6, no. 1, p. 22054, Mar. 2016.
- [64] J. Mendil *et al.*, “Resolving the role of femtosecond heated electrons in ultrafast spin dynamics,” *Sci. Rep.*, vol. 4, pp. 1–7, 2014.
- [65] J. Wu, T. Cheng, C. Lu, X. Zhou, X. Lu, and C. Bunce, “Spin-dynamic measurement techniques,” in *Handbook of Spintronics*, 2015, pp. 785–830.
- [66] C. Kittel, “On the theory of ferromagnetic resonance absorption,” *Phys. Rev.*, vol. 73, no. 2, pp. 155–161, 1948.
- [67] B. Liu *et al.*, “The effect of growth sequence on magnetization damping in Ta/CoFeB/MgO structures,” *J. Magn. Magn. Mater.*, vol. 450, pp. 65–69, 2018.
- [68] S. Iihama, S. Mizukami, H. Naganuma, M. Oogane, Y. Ando, and T. Miyazaki, “Gilbert damping constants of Ta/CoFeB/MgO(Ta) thin films measured by optical

- detection of precessional magnetization dynamics,” *Phys. Rev. B - Condens. Matter Mater. Phys.*, vol. 89, no. 17, p. 174416, 2014.
- [69] S. Mizukami *et al.*, “Gilbert damping in Ni/Co multilayer films exhibiting large perpendicular anisotropy,” *Appl. Phys. Express*, vol. 4, no. 1, p. 13005, 2011.
- [70] B. Liu *et al.*, “Femtosecond laser-heating effect on the magnetization dynamics in perpendicularly magnetized Ta/CoFeB/MgO film,” *New J. Phys.*, vol. 21, p. 53032, 2019.
- [71] H. S. Song *et al.*, “Observation of the intrinsic Gilbert damping constant in Co/Ni multilayers independent of the stack number with perpendicular anisotropy,” *Appl. Phys. Lett.*, vol. 102, no. 10, 2013.
- [72] Y. Wang, “Physics and Micromagnetic Analysis of Advanced Recording Technologies,” 2011.
- [73] H. J. Richter and G. J. Parker, “Temperature dependence of the anisotropy field of L10 FePt near the Curie temperature,” *J. Appl. Phys.*, vol. 121, no. 21, p. 213902, 2017.
- [74] J. M. Sanchez, J. L. Moran-Lopez, C. Leroux, and M. C. Cadeville, “Magnetic properties and chemical ordering in Co-Pt,” *J. Phys. Condens. Matter*, vol. 1, no. 2, pp. 491–496, Jan. 1989.
- [75] A. Capua, S. H. Yang, T. Phung, and S. S. P. Parkin, “Determination of intrinsic damping of perpendicularly magnetized ultrathin films from time-resolved precessional magnetization measurements,” *Phys. Rev. B - Condens. Matter Mater. Phys.*, vol. 92, no. 22, pp. 1–9, 2015.

- [76] B. Liu *et al.*, “Transient enhancement of magnetization damping in CoFeB film via pulsed laser excitation,” *Appl. Phys. Lett.*, vol. 109, no. 4, p. 42401, 2016.
- [77] Z. Chen, M. Yi, M. Chen, S. Li, S. Zhou, and T. Lai, “Spin waves and small intrinsic damping in an in-plane magnetized FePt film,” *Appl. Phys. Lett.*, vol. 101, no. 22, p. 222402, 2012.
- [78] J. Walowski, M. D. Kaufmann, B. Lenk, C. Hamann, J. McCord, and M. Münzenberg, “Intrinsic and non-local Gilbert damping in polycrystalline nickel studied by Ti : SSSapphire laser fs spectroscopy,” *J. Phys. D: Appl. Phys.*, vol. 41, no. 16, p. 164016, 2008.
- [79] M. Djordjevic, G. Eilers, A. Parge, M. Münzenberg, and J. S. Moodera, “Intrinsic and nonlocal Gilbert damping parameter in all optical pump-probe experiments,” *J. Appl. Phys.*, vol. 99, no. 8, pp. 8–308, 2006.
- [80] S. Mizukami *et al.*, “Fast magnetization precession observed in L10-FePt epitaxial thin film,” *Appl. Phys. Lett.*, vol. 98, no. 5, 2011.
- [81] X. Ma, L. Ma, P. He, H. B. Zhao, S. M. Zhou, and G. Lüpke, “Role of antisite disorder on intrinsic Gilbert damping in L1 0 FePt films,” *Phys. Rev. B*, vol. 91, p. 14438, 2015.
- [82] H. S. Song *et al.*, “Intrinsic and extrinsic Gilbert damping in exchange-biased IrMn/Cu/CoFe trilayer films,” *Appl. Phys. Express*, vol. 8, no. 5, 2015.
- [83] S. Mizukami, X. Zhang, and T. Kubota, “Laser-Induced Fast Magnetization Precession and Gilbert Damping for CoCrPt Alloy Thin Films with Perpendicular Magnetic Anisotropy,” *Appl. Phys. Express*, vol. 3, p. 123001, 2010.

- [84] D. M. Lattery, D. Zhang, J. Zhu, X. Hang, J. P. Wang, and X. Wang, “Low Gilbert Damping Constant in Perpendicularly Magnetized W/CoFeB/MgO Films with High Thermal Stability,” *Sci. Rep.*, vol. 8, no. 1, p. 13395, 2018.
- [85] C.-J. Lin *et al.*, “Magnetic and structural properties of Co/Pt multilayers,” *J. Magn. Magn. Mater.*, vol. 93, pp. 194–206, Feb. 1991.
- [86] W. B. Zeper, F. J. A. M. Greidanus, P. F. Carcia, and C. R. Fincher, “Perpendicular magnetic anisotropy and magneto-optical Kerr effect of vapor-deposited Co/Pt-layered structures,” *J. Appl. Phys.*, vol. 65, no. 12, pp. 4971–4975, 1989.
- [87] S. Pal, B. Rana, O. Hellwig, T. Thomson, and A. Barman, “Tunable magnonic frequency and damping in [Co/Pd]8 multilayers with variable Co layer thickness,” *Appl. Phys. Lett.*, vol. 98, no. 8, 2011.
- [88] W. Zhang, V. Vlaminck, J. E. Pearson, R. Divan, S. D. Bader, and A. Hoffmann, “Determination of the Pt spin diffusion length by spin-pumping and spin Hall effect,” *Appl. Phys. Lett.*, vol. 103, no. 24, p. 242414, Dec. 2013.
- [89] W. Zhang *et al.*, “Spin pumping and inverse spin Hall effects - Insights for future spin-orbitronics (invited),” *J. Appl. Phys.*, vol. 117, no. 17, p. 172610, 2015.
- [90] A. De *et al.*, “Shape dependent high frequency spin-wave dynamics in nanoscale magnonic crystals,” *J. Magn. Magn. Mater.*, vol. 487, Oct. 2019.
- [91] S. Pal *et al.*, “Optically induced spin wave dynamics in [Co/Pd]8 antidot lattices with perpendicular magnetic anisotropy,” *Appl. Phys. Lett.*, vol. 105, no. 16, p. 162408, 2014.
- [92] I. Razdolski *et al.*, “Nanoscale interface confinement of ultrafast spin transfer torque

driving non-uniform spin dynamics,” *Nat. Commun.*, vol. 8, no. 1, p. 15007, Apr. 2017.